856

REACTIVITY COEFFICIENTS IN A THORIUM OXIDE FUELLED, HEAVY WATER MODERATED AND COOLED REACTOR

by

Nasr. M. Ghoniem

PART A: MCMASTER (OFF-CAMPUS) PROJECT*

A Report Submitted to the School of Graduate Studies

in Partial Fulfilment of the Requirements

for the Degree

Master of Engineering

Department of Engineering Physics

McMaster University

Hamilton, Ontario, Canada

August 1974

*One of two Project Reports: The other part is designated PART B: ON-CAMPUS PROJECT

MASTER OF ENGINEERING (1974)
Department of Engineering Physics

MCMASTER UNIVERSITY
Hamilton, Ontario

TITLE: REACTIVITY COEFFICIENTS IN A THORIUM OXIDE FUELLED, HEAVY WATER MODERATED AND COOLED REACTOR

AUTHOR: Nasr. M. Ghoniem

SUPERVISORS: Dr. D.A. Thompson and Dr. J.E. Robinson

NUMBER OF PAGES: v, 74

REACTIVITY COEFFICIENTS IN A THORIUM OXIDE FUELLED, HEAVY WATER MODERATED AND COOLED REACTOR

by

N. Ghoniem

ABSTRACT

Temperature coefficients of reactivity for an 37-element reference design of a thorium oxide fuelled, heavy water moderated and cooled reactor, are calculated. The physical processes which determine magnitude and sign of the coefficients are identified and discussed. Results are given for fresh fuel containing equilibrium concentrations of the fission product Xe-135 and with boron control in the moderator. Results are also given for fresh fuel with the equilibrium concentration of Xe-135 but without boron contorl for fuel with an exposue of 1.513 n/k barn and for fuel with an exposure of 3.13 n/k barn; each containing appropriate concentrations of 50 separate nuclides and one-pseudo fission product. The fuel temperature coefficient of reactivity is negative for all the cases studied, while the coolant temperature coefficient of reactivity is positive for all the cases studied. The void effect is an increase in reactivity for all cases studied.

Atomic Energy of Canada Ltd.
Whiteshell Nuclear Research Establishment
Pinawa, Manitoba, Canada
August, 1974

ACKNOWLEDGEMENT

The author wishes to thank Dr. D. Hamel for his help during the course of this work and for the many interesting discussions and valuable comments. Also the author wishes to thank Dr. K. Dormuth for his comments and J.H. Wright for providing auxiliary data.

C O N T E N T S

1. INTRODUCTION

1.1 Concepts and Definitions

Many of the parameters that determine the reactivity of a nuclear reactor, namely the thermal utilization, resonance escape probability, diffusion length, and others, are functions of the temperature of the constituent materials in reactors; as the fuel, coolant and moderator. Such effects ensue essentially from changes in microscopic cross-sections and number densities of materials, due to changes in temperature.

Temperature effects on reactivity are to be understood if a reactor is to be properly operated and controlled.

Temperature coefficients of reactivity are defined as:

$$\alpha_T = \frac{\partial \rho}{\partial T} \qquad (1.1)$$

where ρ is the reactivity of the system with its usual definition:

$$\rho = \frac{(k_{eff}-1)}{k_{eff}}$$

From the viewpoint of control theory, temperature effects on reactivity are considered as a feedback element and are to be taken into consideration in the design of reactor control system. Reactor stability criteria are thus intimately releated to temperature reactivity feedback and the reactor is said to be either inherently stable or unstable with respect to changes in temperature for negative and positive signs of α_T respectively. A schematic

diagram, showing the inclusion of temperature coefficients of reactivity in the feed-back system, is shown in fig. (1.1).

In solid fuelled reactors, it is the temperature coefficient of the fuel which is usually of greatest importance in safety considerations. This is because the fuel temperature responds almost immediately to changes in power, where as the temperatures of the coolant or moderator must wait upon the transfer of heat from the fuel. For this reason the fuel temperature coefficient is often called the prompt temperature coefficient [1].

With the variation of temperature of certain materials, $\frac{\partial \rho}{\partial T}$ varies only slowly, so that a single coefficient is valid for a sizable interval around the temperature of interest. In other materials $\frac{\partial \rho}{\partial T}$ depends strongly on the temperature and must be given as a function of temperature.

One important simplification, in the problem of the calcualtion of various temperature coefficients, is to assume that the temperature of a certain material has the same value independent of position in the reactor. This simplifying assumption allows the definition of a fuel temperature coefficient, a coolant temperature coefficient and a moderator temperature coefficient. These definitions are often called isothermal temperature coefficients of reactivity. Thus in (1.1), if T refers to the temperature of the fuel, α_T is called the fuel temperature coefficient; if T is the temperature of the coolant α_T is called the coolant temperature coefficient and so forth.

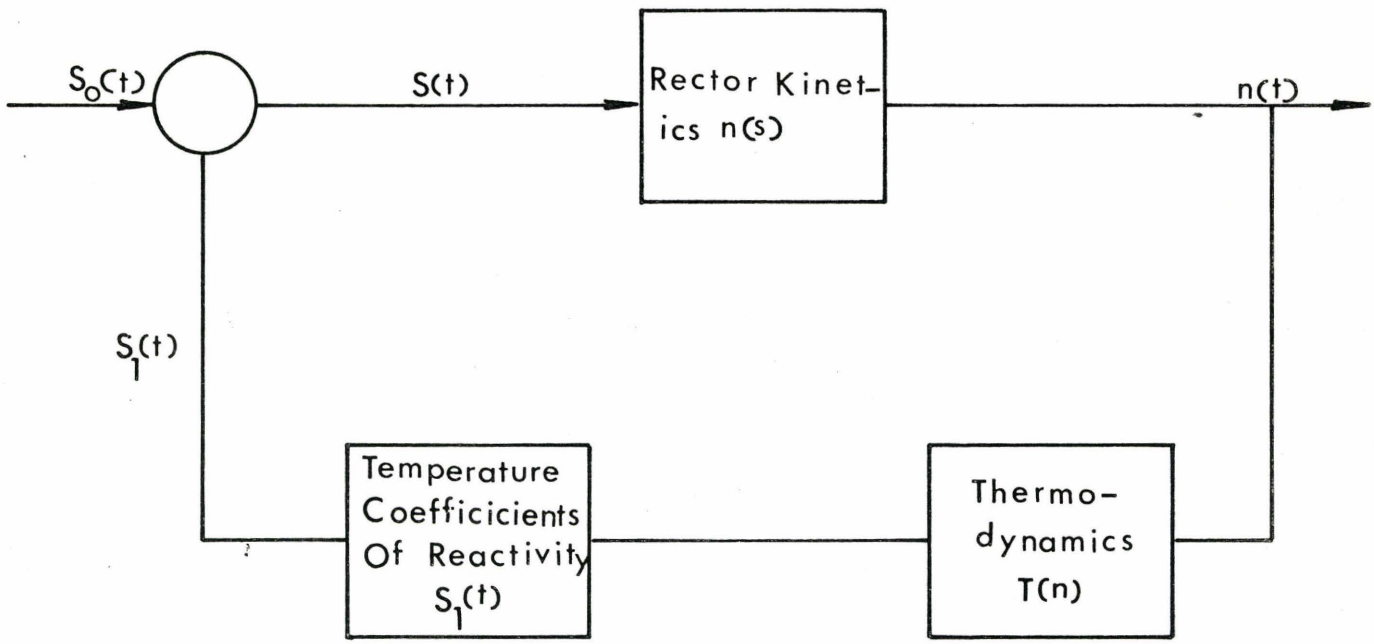

FIGURE(1.1)

Temperature Coefficients Of Reactivity As An Element In A Feedback System.

Temperature coefficients are usually evaluated by calculating ρ at two temperatures T_1, T_2, and deriving the coefficient from:

$$\frac{\partial \rho}{\partial T} \sim \frac{\Delta \rho}{\Delta T} = \frac{\rho_2 - \rho_1}{T_2 - T_1} = \frac{1}{k_1 k_2} \cdot \frac{k_2 - k_1}{T_2 - T_1} \qquad (1.2)$$

Alternatively, perturbation theory can be used to obtain the change in k due to a small change in microscopic cross-sections, caused by a change in temperature.

If $\frac{\partial \rho}{\partial T}$ is strongly temperature dependent, $\rho(T)$ can be calculated at several temperatures, and $\frac{\partial \rho}{\partial T}$ determined by numerical differentiation.

To aquire a good physical understanding of the parameters affecting the temperature coefficient of reactivity, the so called adiabatic approximation is followed. It is normally adopted in the study of slow transients.

The temperature coefficient is defined here as:

$$\frac{\partial \rho}{\partial T} = \frac{1}{k^2} \frac{\partial k}{\partial T} \sim \frac{1}{k} \frac{\partial k}{\partial T} \qquad (1.3)$$

If one now uses the familiar formula,

$$k_{eff} = f \eta p \varepsilon P_{nl} \,, \qquad (1.4)$$

The temperature coefficient of reactivity for the adiabatic approximation can be written as:

$$\frac{\partial \rho}{\partial T} \sim \frac{1}{k} \frac{\partial k}{\partial T}$$

$$= \frac{1}{f} \frac{\partial f}{\partial T} + \frac{1}{\eta} \frac{\partial \eta}{\partial T} + \frac{1}{p} \frac{\partial p}{\partial T} + \frac{1}{\varepsilon} \frac{\partial \varepsilon}{\partial T} + \frac{1}{P_{nl}} \frac{\partial P_{nl}}{\partial T} ; \qquad (1.5)$$

where P_{nl} denotes the non-leakage probability and the other four factors have their usual meaning.

Calculations of the different factors involved in the evaluation of k_{eff} in connection with multigroup theory can be approximately accomplished in the following way:

$$f = \frac{\text{Thermal absorption in fuel}}{\text{Thermal absorption in system}}$$

$$\eta = \frac{\text{Number of neutrons per sec. produced by thermal fission}}{\text{Thermal absorption in fuel}}$$

$$p = \frac{\text{Thermal absorption in system}}{\text{Total absorption in system}} \qquad (1.6)$$

$$\varepsilon = \frac{\text{Number of neutrons per sec. produced over total energy range}}{\text{Number of neutrons per sec. produced by thermal fission}}$$

Although the definition of the terms in equation (1.5) is not identical with the original definition of the different terms based on the one group formalism; nevertheless discussions based on (1.5) allows more physical insight into the problem considered here.

The temperature coefficients reported here were calculated from the results of separate calculations of the multiplication factor k. Only fuel, coolant and coolant void coefficients were determined. The definition given by (1.2) is used in their calculation.

Results are given for calculations with fresh fuel (BOL), containing

equilibrium concentration of the fission product Xe-135. Aslo results for middle of fuel life (MOL) and end of fuel life (EOL), for irradiations of 1.51336 n/kbarn and 3.13 n/kbarn respectively, are given. Appropriate concentrations of 50 separate elements and 1 pseudo fission product are included.

1.2 Case Description

In the following a complete account of the reference case is given in the form of tables. The dimensions of the reactor and of the reference cell are found in tables (1.1) and (1.2). In table (1.3) the composition of materials in the reference cell is presented including appropriate proportions of materials from end regions at average temperatures. A homogenization procedure is followed to mix materials in end regions with those in fuel, oxygen gap, clad and coolant. It is to be noted that only an equilibrium concentration of Xe-135 is included in the fresh fuel. Other fission products exist in very small quantities.

TABLE (1.1)

REACTOR DIMENSIONS

Core Height	600	cm
Radial Extrapolation Distance	60	cm
Vertical Extrapolation Distance at each end	5	cm
Reflector Thickness	60	cm
Number of Channels	732	
Core Radius	349	cm
Core Average Geometrical Buckling	0.000079306	cm^{-2}

DIMENSIONS OF THE REFERENCE CELL

1. Fuel Element

Fuel Radius	R_1 = 0.6335 cm
Sheath Inside Radius	R_2 = 0.6380 cm
Sheath Outside Radius	R_3 = 0.6780 cm

2. Fuel Bundle

Total Number of Fuel Elements	37
Pitch Circle Radii (Number of Fuel Elements in Brackets)	(1) C_1 = 0.0 cm
	(6) C_2 = 1.483 cm
	(12) C_3 = 2.865 cm
	(18) C_4 = 4.316 cm
Relative Position of Element Rings (fig. 1.2)	α_1 = 0.0
	α_2 = 0.0
	α_3 = 15°
	α_4 = 10°
Fuel Stack Length	s = 48.15 cm
Number of Fuel Bundles per Channel	12
Gap Between Fuel Faces of Two Succeeding Bundles	G = 1.85 cm

3. Pressure Tube

Inside Radius	P_1 = 5.1780 cm
Outside Radius	P_2 = 5.5951 cm

4. Calandria Tube

Inside Radius	T_1 = 6.448 cm
Outside Radius	T_2 = 6.585 cm

5. Lattice

Square Lattice Pitch	27.300 cm
Equivalent Cell Radius	Q = 15.40237563 cm

6. End Region

(Region Between Fuel Faces of Two Vertically Neighbouring Bundles Inside the Pressure Tube)

Total volume	160.039 cm^3
Partial volumes	Zr 39.688 cm^3
	D_2O, H_2O 120.351 cm^3

Partial volumes of this region added to the fuel, gas, gap, clad and coolant

Fuel	88.6336 cm^3
Gas gap	1.2637 cm^3
Clad	11.625 cm^3
Coolant	58.516 cm^3

TABLE (1.3)

COMPOSITION OF MATERIALS IN THE REFERENCE CELL

1. Fuel (End Regions Included)

Volume 26,925.9576 cm^3

Fraction of Cell Volume 0.0602136

Average Temperature 753°C

NUCLEAR DENSITIES [atoms/barn.cm]

Nuclide	Fresh Fuel (BOL)	(MOL) Fuel Irradiation 1.513n/k barn	(EOL) Fuel Irradiation 3.13 n/k barn
Th-230	-	-	-
Th-232	9.91742×10^{-3}	9.8109×10^{-3}	9.6305×10^{-3}
Th-234	-	-	-
Pa-231	-	-	-
Pa-233	-	1.55707×10^{-5}	1.8882×10^{-5}
U-233	$1.54951\text{-}x\ 10^{-4}$	1.39922×10^{-4}	1.3588×10^{-4}
U-234	6.19983×10^{-5}	6.46148×10^{-5}	6.8928×10^{-5}
U-235	1.33521×10^{-5}	1.26185×10^{-5}	1.2094×10^{-5}
U-236	3.31746×10^{-5}	3.34327×10^{-5}	3.4175×10^{-5}
U-238	8.08133×10^{-7}	7.73186×10^{-7}	7.2771×10^{-7}
Np-237	-	1.05928×10^{-6}	2.0005×10^{-6}
Pu-239	7.55952×10^{-5}	1.34348×10^{-5}	5.0804×10^{-7}
Pu-240	3.73931×10^{-5}	3.64896×10^{-5}	1.5484×10^{-5}
Pu-241	7.49670×10^{-6}	1.00907×10^{-5}	5.9338×10^{-6}
Pu-242	3.18208×10^{-6}	7.34941×10^{-6}	1.3037×10^{-5}
Am-241	-	2.09675×10^{-7}	1.7112×10^{-7}
AM-242	-	6.11758×10^{-9}	5.3693×10^{-9}
AM-243	-	7.24251×10^{-7}	2.2769×10^{-6}
Kr-83	-	1.09834×10^{-6}	2.2554×10^{-6}

Nuclide	Fresh Fuel (BOL)	(MOL) Fuel Irradiation 1.513n/k barn	(EOL) Fuel Irradiation 3.13 n/k barn
Mo-95	-	8.69959×10^{-6}	1.9857×10^{-5}
Te-99	-	8.0535×10^{-7}	1.7205×10^{-5}
Pu-101	-	6.27311×10^{-6}	1.3059×10^{-5}
Ru-103	-	8.72752×10^{-5}	6.6896×10^{-7}
Rh-103	-	3.59028×10^{-6}	6.2367×10^{-6}
Rh-105	-	1.69936×10^{-8}	9.1256×10^{-9}
Pd-105	-	3.13546×10^{-6}	5.2095×10^{-6}
Pd-108	-	1.55784×10^{-6}	2.4556×10^{-6}
Ag-109	-	8.51497×10^{-7}	1.1627×10^{-6}
Cd-113	-	1.33222×10^{-9}	7.9210×10^{-11}
In-115	-	2.99317×10^{-8}	4.1290×10^{-8}
I-127	-	7.55874×10^{-7}	1.7754×10^{-6}
Xe-131	-	4.79305×10^{-6}	9.0342×10^{-6}
Cs-133	-	9.32543×10^{-6}	1.9589×10^{-5}
Cs-134	-	3.80269×10^{-7}	1.7261×10^{-6}
Cs-135	-	1.41157×10^{-6}	2.8462×10^{-6}
Xe-135	3.12375×10^{-9}	2.03784×10^{-9}	1.61177×10^{-9}
Nd-143	-	7.00715×10^{-6}	1.1942×10^{-5}
Nd-145	-	4.85611×10^{-6}	1.0379×10^{-5}
Pm-147	-	9.80469×10^{-7}	1.3462×10^{-6}
Sm-147	-	2.32203×10^{-8}	7.4794×10^{-7}
Pm-148	-	1.55397×10^{-8}	2.0046×10^{-8}
Sm-149	-	1.91933×10^{-8}	1.7740×10^{-8}
Sm-150	-	1.76682×10^{-6}	4.1369×10^{-6}
Sm-151	-	1.08022×10^{-7}	1.2010×10^{-7}
Sm-152	-	1.07202×10^{-6}	1.8748×10^{-6}
Eu-153	-	5.41603×10^{-7}	1.2626×10^{-6}

Nuclide	Fresh Fuel (BOL)	(EOL) Fuel Irradiation 1.513 n/k barn	(EOL) Fuel Irradiation 3.13 n/k barn
Eu-154	-	1.07810×10^{-7}	3.7121×10^{-7}
Eu-155	-	1.56446×10^{-8}	4.1495×10^{-8}
Gd-157	-	1.13679×10^{-10}	5.0210×10^{-11}
PFP	-	5.18085×10^{-5}	1.1084×10^{-4}
O-16	2.13408×10^{-2}	2.13408×10^{-2}	2.13408×10^{-2}
Zr-91	4.07585×10^{-4}	4.07585×10^{-4}	4.07585×10^{-4}
H	3.08274×10^{-6}	3.08274×10^{-6}	3.08274×10^{-6}
D	1.38446×10^{-3}	1.38446×10^{-3}	1.38446×10^{-3}

2. Oxygen Gas Gap

Volume 383.8896 cm^3

Fraction of cell volume 0.00085848

Nuclear Densities [atoms/barn.cm]

O - 6.63270×10^{-4}

Zr - 4.07585×10^{-4}

H - 2.72327×10^{-6}

D - 1.222467×10^{-3}

3. Sheath

Volume 3531.7812 cm^3

Fraction of cell volume 0.007898

Nuclear Densities [atoms/barn.cm]

O - 6.12595×10^{-4}

Zr - 4.20123×10^{-2}

H - 2.72327×10^{-6}

D - 1.22247×10^{-3}

4. Coolant

Volume 1481.3941 cm^3

Fraction of cell volume 0.0033128

Nuclear Densities [atoms/barn.cm

Temp. 473 K

O - 2.85071×10^{-2}

Zr - 4.07585×10^{-4}

H - 1.26727×10^{-4}

D - 5.68875×10^{-2}

Temp. 523 K

O 2.62434×10^{-2}

Zr 4.07585×10^{-4}

H 1.16664×10^{-4}

D 5.23701×10^{-2}

Temp. 573 K

O 2.12332×10^{-2}

Zr 4.07585×10^{-4}

H 1.04144×10^{-4}

D 4.67501×10^{-2}

Temp. 623 K

O 1.713085×10^{-2}

Zr 4.07585×10^{-4}

H 7.61545×10^{-4}

D 3.41855×10^{-2}

5. Pressure Tube

Volume 8,469.97257 cm^3

Fraction of cell volume 0.0189411

Nuclear Density [atoms/barn/cm]

Zr 4.49333×10^{-2}

6. Air Gas Gap

Volume 22,727.06223 cm^3

Fraction of cell volume 0.0508238

Nuclear Density [atoms/bar.cm]

O 5.26996×10^{-5}

7. Calandria Tube

Volume 3,365.62779 cm^3

Fraction of cell volume 0.0075264

Nuclear Density [atom/barn.cm]

Zr 4.32465×10^{-2}

8. Moderator

Volume 365,438.1314 cm^3

Fraction of Cell Volume 0.81721686

Nuclear Densities [atom/barn.cm]

H 1.44899×10^{-4}

D 6.50450×10^{-2}

9. End Region

Volume $160.039 \times 12 = 1920.468$ cm^3

Fraction of Cell Volume 0.00429468

Region	1	2
Density	6.55	0.805921
Number of Component Materials	1	2
Volumes	39.688	120.351
Materials	Zr	D_2O, H_2O
Wt. fraction	1.0	0.998, 0.002

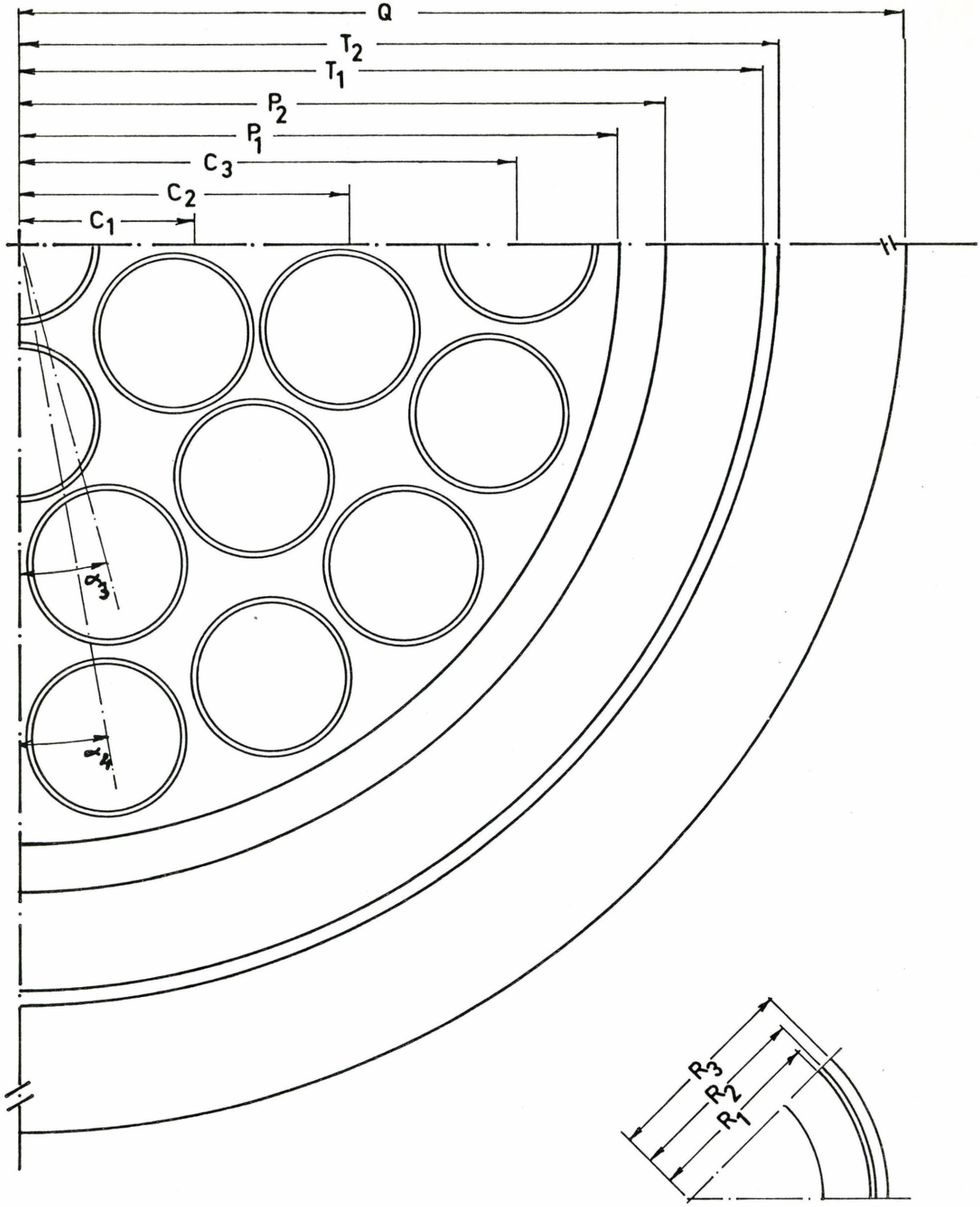

FIGURE (1.2)

Quarter Of a Cross Section Through The Fuel-Bearing Part Of The Reference Cell. See Table 1.2 For Legend

1.3 Simplification of the Cell Structure

To use a computer code for one-dimensional cylindrical geometry, the detailed structure of the lattice cell, as described in Table (1.2) and figure (1.2), has to be simplified. The outer boundary of the cell is replaced by a cylindrical one, preserving the total cross-sectional area. The calendria tube, gas gap and pressure tube are left with the same dimensions. The fuel, air gap and cladding material are homogenized into four different annuli. Outside the second, third and fourth homogeneous mixture annuli there are three coolant annuli. The materials inside the pressure tube in the "end region" between the faces of two adjacent rod-bundles of a channel are homogenized and subsequently added to, and homogenized with, the materials in the annular regions in proportion to the geometrical cross-sections of these regions.

The geometrical cross-section of the simplified lattice cell, made up of concentric nested annuli, is shown in figure (1-3). The different annuli have the following description counting from inside to outside.

	Construction	Designation
1.	Fuel, gas gap and sheath	HOM1
2.	Fuel, gas gap and sheath	HOM2
3.	Coolant	COL1
4.	Fuel, gas gap and sheath	HOM3
5.	Coolant	COL2
6.	Fuel, gas gap and sheath	HOM4
7.	Coolant	COL3
8.	Pressure tube	PT
9.	Gas gap	GG
10.	Calandria Tube	CT
11.	Moderator	MOD

The average temperatures of fuel and coolant used are 1026 K and 566 K respectively with allowance of temperature variations around these averages. The temperatures of all other reactor materials are assumed virtually constant at their averages. The following average temperatures are used:

Gas inbetween fuel and sheath	850 K
Sheath	650 K
Pressure tube	600 K
Gas gap between pressure and calandria tube	400 K
Calandria tube	350 K
Moderator	325 K

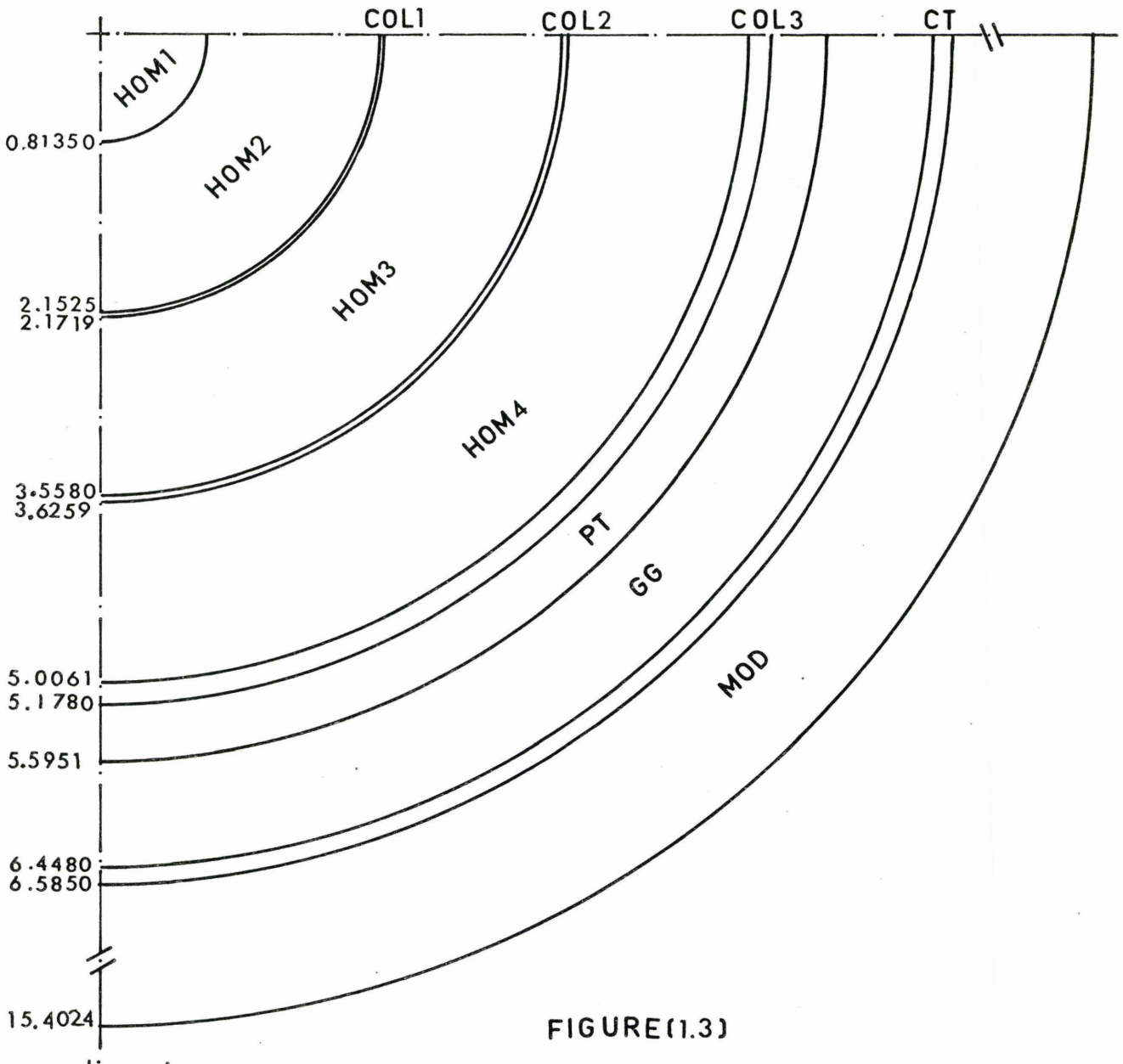

FIGURE(1.3)

Quarter Of The Simplified Cell Cross-Section

2.1 Introduction

The Winfrith improved multigroup scheme (WIMS) is used to calculate the temperature coefficients of reactivity.

Isothermal temperature coefficients of reactivity are derived from reactivities calculated at two different temperatures or by differentiation of the numerically determined reactivity $\rho(T)$. Coolant and fuel temperature changes are considered separately.

2.2 Energy Group Structure

The basic WIMS library contains cross-sections for 69 energy groups (defined in table 2-1) of which the first 14 'fast' groups occur at equal lethargy intervals of 0.5 in the range of 10 MeV - 9.118 KeV.

Below 9.118 KeV there are 13 'resonance' energy groups down to 4eV for which the isotopes with significant resonance behaviour have their effective resonance integrals tabulated in each group as a function of effective potential scattering cross-section and temperature T. The group boundaries in the lower part of the resonance region are chosen so that the important resonances in the fissile and fertile isotopes are well centred in their energy group.

Below 4eV in the 'thermal' region there are 42 groups whose energy boundaries are chosen to ensure adequate definition to neutron capture in the Pu^{239} resonance at 0.29eV, and the Pu^{240} resonance at 1.0eV.

2.3 Basic Features of the WIMS Code

Description and validations of the physics methods embodied in the WIMS code have been given by Askew et al (3) and Fayers et al (2).

Although solution of the transport equations is possible in the full 69-group structure, such calculations tend to be unnecessarily elaborate. A special procedure is therefore incorporated in WIMS for group condensation. This is based on the use of the 'spectrox' method for producing, in the full 69 groups, a condensation flux spectrum for each of the principal regions of the lattice cell, coupled together through collision probability expressions. In the cluster geometry used here, separate spectra are provided for fuel, clad, coolant and moderator.

Following the generation of condensed group cross-sections, a more accurate spatial solution is obtained using either differential (discrete ordinate, DSN) or integral (collision probability) transport theory methods. The DSN method is used in the calculation of the temperature coefficients of reactivity. Thirteen energy groups have been used here for the main transport calculations.

Calculations for the leakage in WIMS are performed on the homogenized cell, in the same group structure as used for the main transport routine. Allowance for assymmetric diffusion is made using methods based on the theory developed by Benoist (4). The leakage flux solution is obtained by either diffusion theory or the B_1 method, the latter employing explicit scattering data for the principal moderators, viz. hydrogen, deuterium, oxygen and carbon. In the case of hydrogen and graphite, tabulations based upon the Chalk River

scattering experiments (5) are available. Alternative theoretical models are also provided (for example Nelkin (6) and effective width (7) models for hydrogen and Honeck (8) and effective width models for deuterium). All other materials have gas law scattering matrices in the thermal region (2).

Treatment of the resonance region in WIMS is based on the use of equivalence theorems to relate a group resonance integral for the heterogeneous cell to group resonance integrals for various homogeneous mixtures of moderator and resonance absorption. The provision of as many as 13 energy groups is the resonance region allows a varying source shape to have its proper influence on resonance captures, an effect which is particularly important for cluster geometries.

There are various edit facilities in WIMS, e.g. the reaction rate edit which outputs absorption, fission and fission-yield reactions, as appropriate for any given nuclide. The reaction rate edits are provided for both the results of the main transport calculation, and for the results obtained when any of the leakage calculations are used to modify the fluxes obtained from the K_{∞} calculation. Details of the editing and other operating instructions for the WIMS code have been given by Roth et al (9).

The energy boundaries of the 69 group cross-section library are shown in table (2.1), while the energy boundaries of the condensed 13 groups are shown in table (2.2). Figure (2.1) illustrates the computational sequence used in the WIMS code.

69-GROUP ENERGY BOUNDARIES FOR WIMS

GROUP	ENERGY	ENERGY WIDTH	LETHARGY WIDTH	GROUP	ENERGY	ENERGY WIDTH	LETHARGY WIDTH
	MeV						
1	10.0 - 6.0655	3.9345	0.49997	36	1.097 - 1.071	0.026	0.02399
2	6.0655 - 3.679	2.3865	0.49998	37	1.071 - 1.045	0.026	0.02458
3	3.679 - 2.231	1.448	0.50019	38	1.045 - 1.020	0.025	0.02421
4	2.231 - 1.353	0.878	0.50013	39	1.020 - 0.996	0.024	0.02381
5	1.353 - 0.821	0.532	0.49956	40	0.996 - 0.972	0.024	0.02439
6	0.821 - 0.500	0.321	0.49592	41	0.972 - 0.950	0.022	0.02289
7	0.500 - 0.3025	0.1975	0.50253	42	0.950 - 0.910	0.040	0.04302
8	0.3025 - 0.183	0.1195	0.50260	43	0.910 - 0.850	0.060	0.06821
9	0.183 - 0.1110	0.072	0.49996	44	0.850 - 0.780	0.070	0.08594
10	0.111 - 0.06734	0.04366	0.49978	45	0.780 - 0.625	0.155	0.22154
11	0.06734 - 0.04085	0.02649	0.49985	46	0.625 - 0.500	0.125	0.22314
12	0.04085 - 0.02478	0.01607	0.49987	47	0.500 - 0.400	0.100	0.22314
13	0.02478 - 0.01503	0.00975	0.49999	48	0.400 - 0.350	0.050	0.13353
14	0.01503 - 0.009118	0.005912	0.49980	49	0.350 - 0.320	0.030	0.08961
				50	0.320 - 0.300	0.020	0.06454
	eV			51	0.300 - 0.280	0.020	0.06899
15	9118.0 - 5530.0	3588.0	0.50006	52	0.280 - 0.250	0.030	0.11333
16	5530.0 - 3519.1	2010.9	0.45198	53	0.250 - 0.220	0.030	0.12783
17	3519.1 - 2239.45	1279.65	0.45198	54	0.220 - 0.180	0.040	0.20067
18	2239.45 - 1425.1	814.35	0.45199	55	0.180 - 0.140	0.040	0.25131
19	1425.1 - 906.898	518.202	0.45197	56	0.140 - 0.100	0.040	0.33647
20	906.898 - 367.262	539.636	0.90395	57	0.100 - 0.080	0.020	0.22314
21	367.262 - 148.728	218.534	0.90396	58	0.080 - 0.067	0.013	0.17733
22	148.728 - 75.5014	73.2266	0.67797	59	0.067 - 0.058	0.009	0.14425
23	75.5014 - 48.052	27.4494	0.45187	60	0.058 - 0.050	0.008	0.14842
24	48.052 - 27.700	20.352	0.55085	61	0.050 - 0.042	0.008	0.17435
25	27.700 - 15.968	11.732	0.55085	62	0.042 - 0.035	0.007	0.18232
26	15.968 - 9.877	6.091	0.48038	63	0.035 - 0.030	0.005	0.15415
27	9.877 - 4.00	5.877	0.90391	64	0.020 - 0.025	0.005	0.18232
28	4.00 - 3.30	0.700	0.19237	65	0.025 - 0.020	0.005	0.22314
29	3.30 - 2.60	0.700	0.23841	66	0.020 - 0.015	0.005	0.28768
30	2.60 - 2.10	0.500	0.21357	67	0.015 - 0.010	0.005	0.40547
31	2.10 - 1.50	0.600	0.33647	68	0.010 - 0.005	0.005	0.69315
32	1.50 - 1.30	0.200	0.14310	69	0.005 - 0.	0.005	-
33	1.30 - 1.15	0.150	0.12260				
34	1.15 - 1.123	0.027	0.02376				
35	1.123 - 1.097	0.026	0.02342				

TABLE (2.2)

13-ENERGY GROUP BOUNDARIES FOR CONDENSED SPECTRUM

GROUP	ENERGY	ENERGY WIDTH	LETHARGY WIDTH
	MeV	MeV	
1	10.0 - 0.821	0.179	1.085657
2	0.821 - 0.009118	0.811882	1.954444
	eV	eV	
3	9118.0 - 75.5014	9042.4986	4.793854
4	75.5014 - 15.968	59.5334	1.5535644
5	15.968 - 4.00	11.968	1.3842923
6	4.00 - 1.15	2.85	1.246532
7	1.15 - 0.972	0.178	0.1681614
8	0.972 - 0.625	0.347	0.44160415
9	0.625 - 0.140	0.485	1.4961092
10	0.140 - 0.05	0.090	1.0296194
11	0.05 - 0.03	0.02	0.5108256
12	0.030 - 0.015	0.015	0.69314718
13	0.015 - 0.0	0.015	-

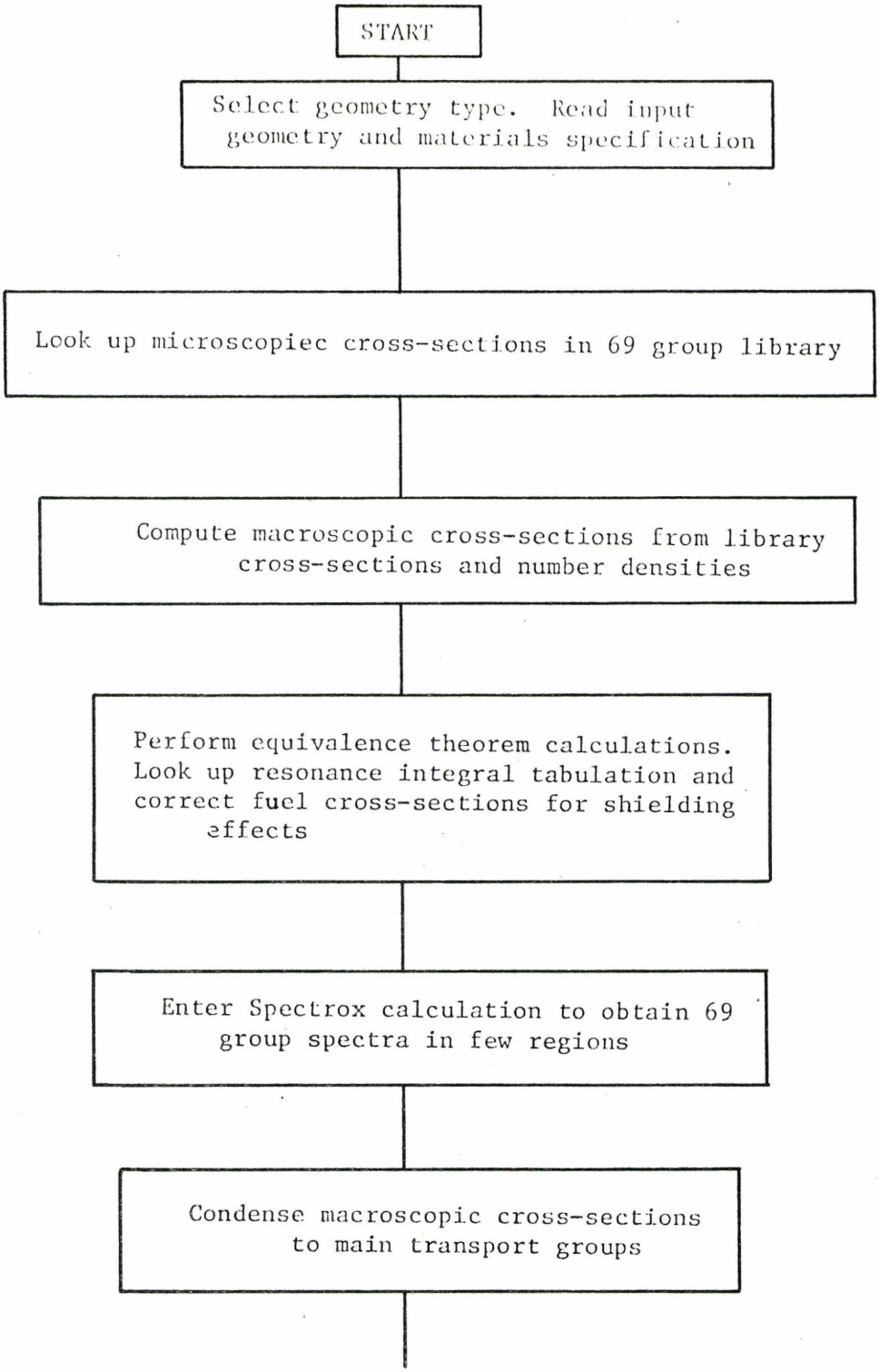

FIGURE (1.2) Block diagram of computational Sequences in WIMS

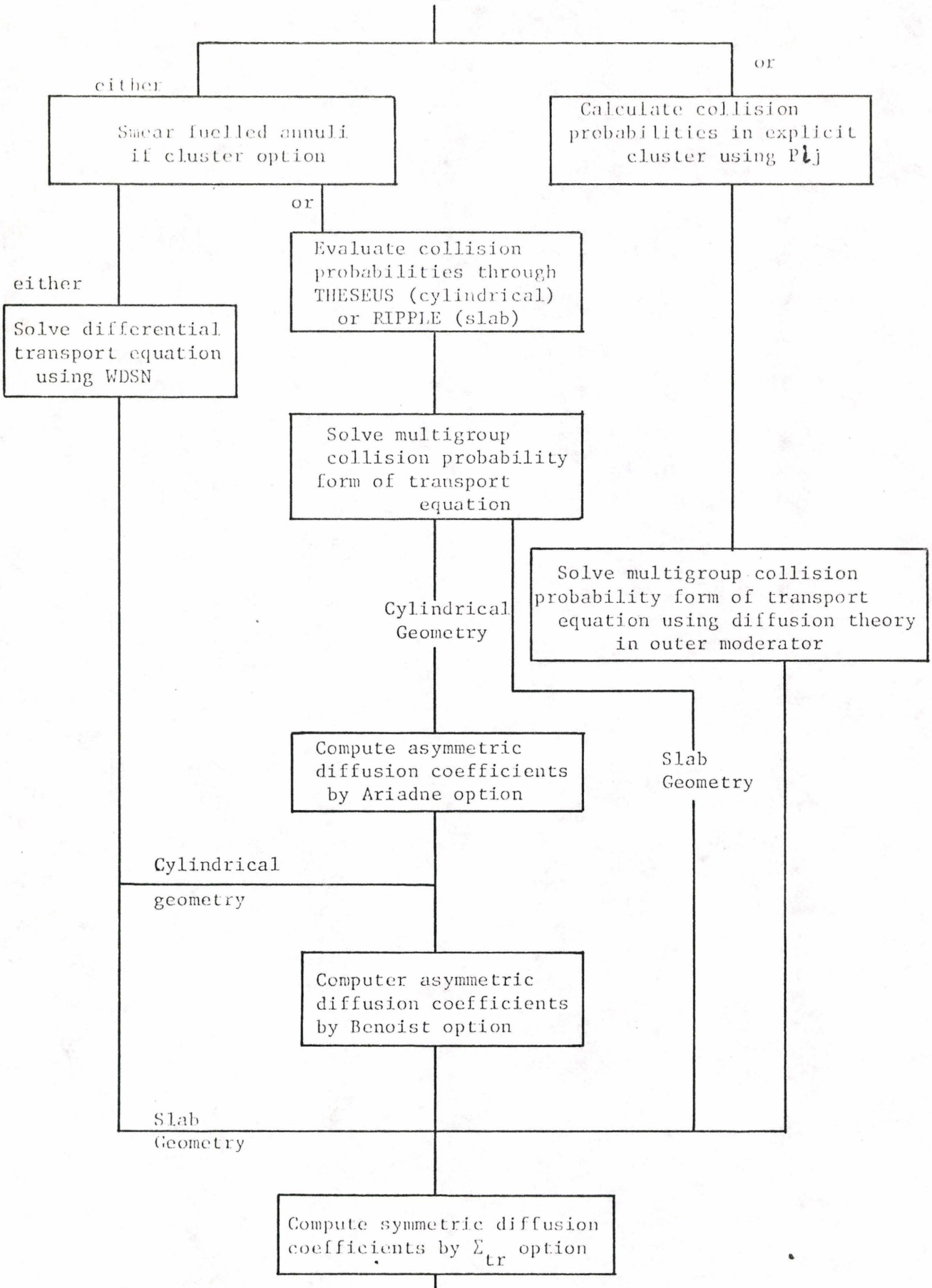

FIGURE (1.2) continued

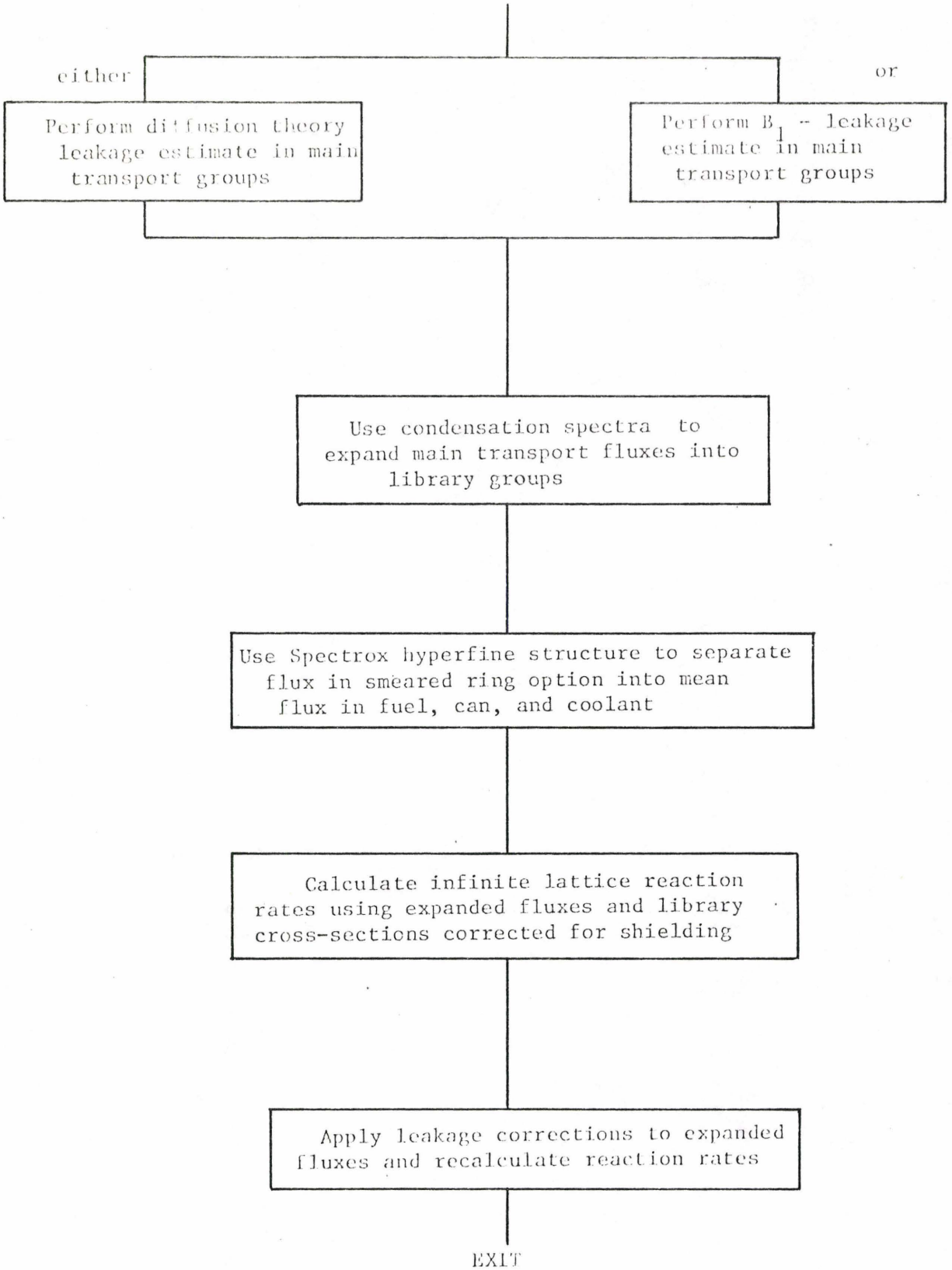

FIGURE (1.2) concluded

3. FUEL TEMPERATURE COEFFICIENT OF REACTIVITY

3.1 General Aspects:

The fuel temperature coefficient of reactivity, $\frac{\partial \rho}{\partial T_f}$ relates changes in temperature with induced changes in reactivity:

$$\Delta\rho = \frac{\partial \rho}{\partial T_f}\Big|_{T_f} \cdot \Delta T_f \qquad (3.1)$$

Here the thermal expansion of the fuel is neglected because of its minor influence on fuel temperature coefficients. Changes in neutron reaction cross-sections are reflected in changes of the flux spectra for the different zones and in changes of reaction rates. All mentioned quantities are therefore studied to understand the physical mechanisms which cause the reactivity change.

Xe-135 reaches equilibrium relatively rapidly, and it is also effective in neutron absorption; so an equilibrium concentration of Xe is included in the case of fresh fuel. It is shown, in table (3.1), that Xe-135 reaches its equilibrium concentration comparatively rapidly while Rh-105 and Sm-149 take a much longer time to reach their equilibrium concentrations. The middle of life case corresponds to an irradiation time of 310.01 days, and the end of life case corresponds to full irradiation time of 691.84 days.

The scattering kernel for H in H_2O is based on the Nelkin model [6] and cross-section sets are given at 293K, 333K, 373K, 423K and 473K. The scattering kernel for D in D_2O is based on the effective width model [7] and cross-section sets are given at 293K, 450K, 600K. Interpolation is used

TABLE (3.1)

FISSION PRODUCTS CONCENTRATIONS AS FUNCTIONS OF IRRADIATION

Irradiation Time (days)	Irradiation (MWd/TE)	Rh-105 Concentration (atoms/cm.barn)	Xe-135 Concentration (atoms/cm.barn)	Sm-149 Concentration (atoms/cm.barn)
0.01	0.641	1.32181×10^{-10}	3.12375×10^{-9}	4.71249×10^{-11}
10.01	641.665	2.42791×10^{-8}	3.07472×10^{-9}	1.95019×10^{-8}
110.01	7051.899	2.38887×10^{-8}	2.66569×10^{-9}	2.10743×10^{-8}
210.01	13462.134	2.07107×10^{-8}	2.31074×10^{-9}	2.00555×10^{-8}
310.01	19872.369	1.69993×10^{-8}	2.03784×10^{-9}	1.91933×10^{-8}
410.01	26282.604	1.38918×10^{-8}	1.85568×10^{-9}	1.86193×10^{-8}
510.01	32692.839	1.16838×10^{-8}	1.74055×10^{-9}	1.82416×10^{-8}
600.01	38462.05	1.01926×10^{-8}	1.66840×10^{-9}	1.79963×10^{-8}
691.84	44348.75	9.1256×10^{-9}	1.6177×10^{-9}	1.7740×10^{-8}

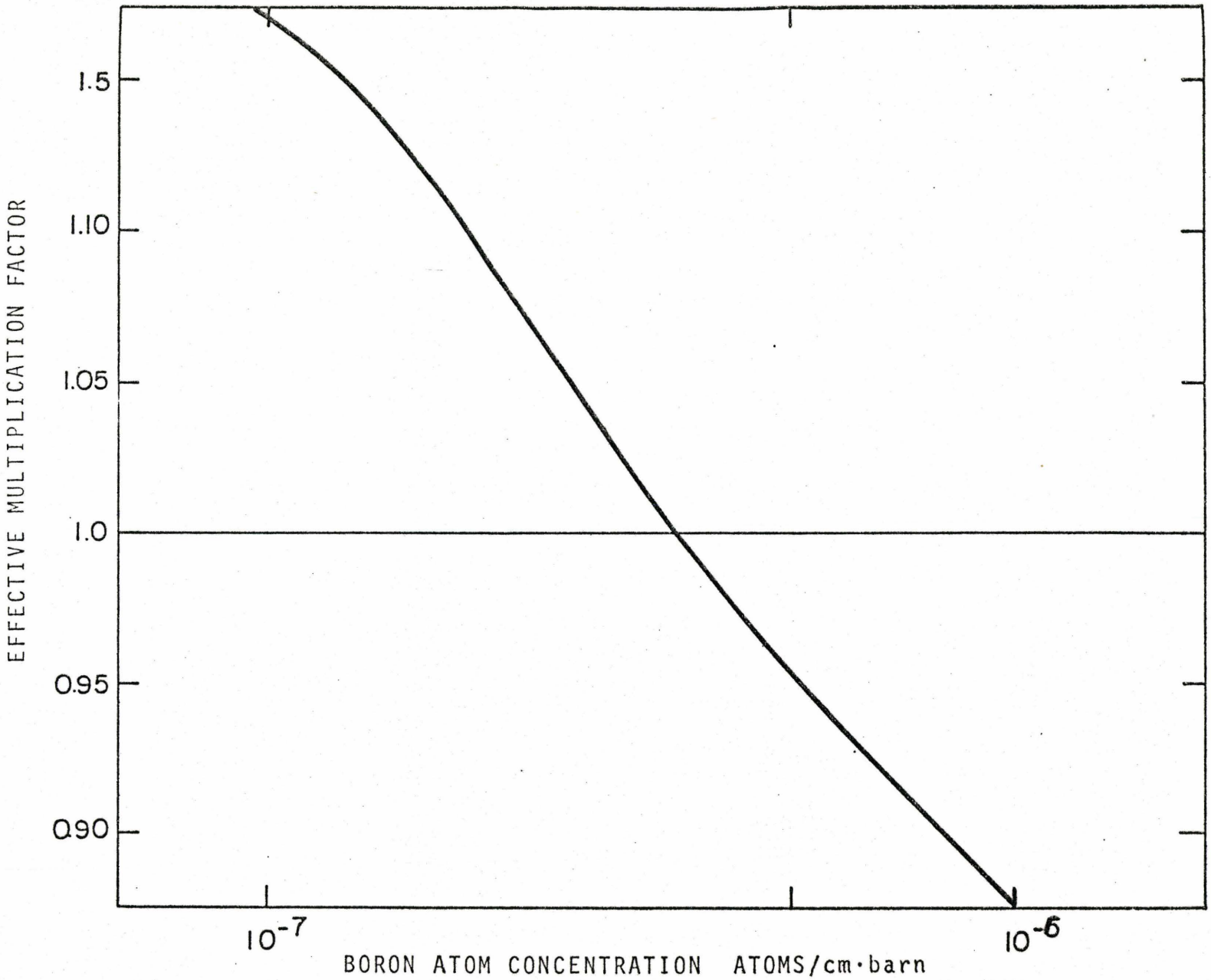

FIGURE 3.1 k_e VS. BORON ATOM CONCENTRATION IN THE MODERATOR AT AVERAGE TEMPERATURES

for other temperatures.

The results of the calculation of the infinite and effective multiplication factors at different fuel temperatures are shown in table (3.2) a, b, c and d. The fuel temperature coefficients, as calculated by relation (1.2), are shown in table (3.3) and illustrated in figure (3.2).

The macroscopic absorption cross-sections of four different nculide mixtures are plotted as a function of energy in figures (3.3) and (3.4). The four mixtures are: fresh fuel with Boron control in the moderator (fuel A), coolant, moderator and homogenized cell mixture.

The macroscopic absorption cross-section of the fuel mixture for different irradiation conditions - A,C,D - is shown as a function of neutron energy in figure (3.5). In the fast neutron energy region, only the macroscopic absorption cross-section of fresh fuel is shown, since it differes only slightly from the macroscopic absorption cross-sections of irradiated fuel.

3.2 Discussion of Results

3.2.a. General

The reactivity of a reactor can be adjusted by addition of boron to the moderator. It is to be expected that as the atom n,mber density of boron in the moderator is increased the reactivity of the system decreases; this is represented graphically in figure (3.1). A value of 3.85×10^{-7} atoms/cm. bar

in the moderator is chosen to represent normal operating conditions. This brings the effective multiplication factor of the reactor to 1.068956 and the corresponding reactivity to 64.51 mk under average temperature conditions.

Figure (3.2) shows that the reactivity decreases as the fuel temperature coefficient is increased. The fuel temperature coefficient is negative over the whole temperature range covered by the four cases. The magnitude of the fuel temperature coefficient for the fresh fuel with Boron control case (A) decreases from $0.938 \times 10^{-5} {}^{\circ}C^{-1}$ to $0.850 \times 10^{-5} {}^{\circ}C^{-1}$ as the fuel temperature rises from 951 K to 1101 K.

The effect of Boron in the moderator accounts for the big changes observed in the values of the fuel temperature coefficients of reactivity between curve A and curve B. The magnitude of the fuel temperature coefficient of reactivity is generally larger when Boron is included in the moderator. The presence of Boron in the moderator results in more thermal neutron absorptions. This in effect increases the relative number of epithermal neutrons and hence the influence of Doppler-broadening of the resonances in Th-232.

The same general argument, to account for the magnitude increase of the temperature coefficient of reactivity, could now be extended to the cases of irradiated fuel. With increased irradiation Pu-239 concentration decreases and less thermal productions occur; hence the positive contribution from η decreases. Also thermal absorption in the fuel decreases and there is a corresponding increase in the relative number of epithermal neutrons with the consequent negative increase of p.

TABLE (3.2)a

INFINITE AND EFFECTIVE MULTIPLICATION FACTORS FOR FRESH FUEL WITH EQUILIBRIUM XE AND BORON

T(k)	K_∞	K_{eff}
926	1.093713	1.069162
976	1.093165	1.068626
1026	1.092632	1.068106
1076	1.092115	1.067600
1126	1.091619	1.067116

TABLE (3.2)b

INFINITE AND EFFECTIVE MULTIPLICATION FACTORS FOR FRESH FUEL WITH EQUILIBRIUM XE

T(k)	K_∞	K_{eff}
926	1.273709	1.242498
976	1.273124	1.241927
1026	1.272558	1.241373
1076	1.272010	1.240836
1126	1.271490	1.240319

TABLE (3.2)c

INFINITE AND EFFECTIVE MULTIPLICATION FACTORS
FOR MIDDLE OF LIFE FUEL (MOL)

Temperature K	K_{∞}	K_{eff}
926	0.9844951	0.9581251
976	0.9840748	0.9577081
1026	0.9836695	0.9573042
1076	0.9832749	0.9569125
1126	0.9828949	0.9565193

TABLE (3.2)d

INFINITE AND EFFECTIVE MULTIPLICATION FACTORS
FOR END OF LIFE FUEL (EOL)

Temperature K	K_{∞}	K_{eff}
926	0.9102812	0.8850595
976	0.9098744	0.8846533
1026	0.9094790	0.8842583
1076	0.9090944	0.8838738
1126	0.908723	0.8835023

TABLE (3.3)

FUEL TEMPERATURE COEFFICIENT OF REACTIVITY, $\frac{\partial \rho}{\partial T} \times 10^{5} {}^{o}C^{-1}$
AS A FUNCTION OF TEMPERATURE

Temperature K	Fresh Fuel with B (BOL) A	Fresh Fuel without B B	Middle of Life Fuel (MOL) C	End of Life Fuel (EOL) D
951	- 0.938265	- 0.740073	- 0.908889	- 1.03758
1001	- 0.9111571	- 0.718690	- 0.881091	- 1.009892
1051	- 0.887477	- 0.697248	- 0.855188	- 0.983914
1101	- 0.849679	- 0.671851	- 0.859167	- 0.95146

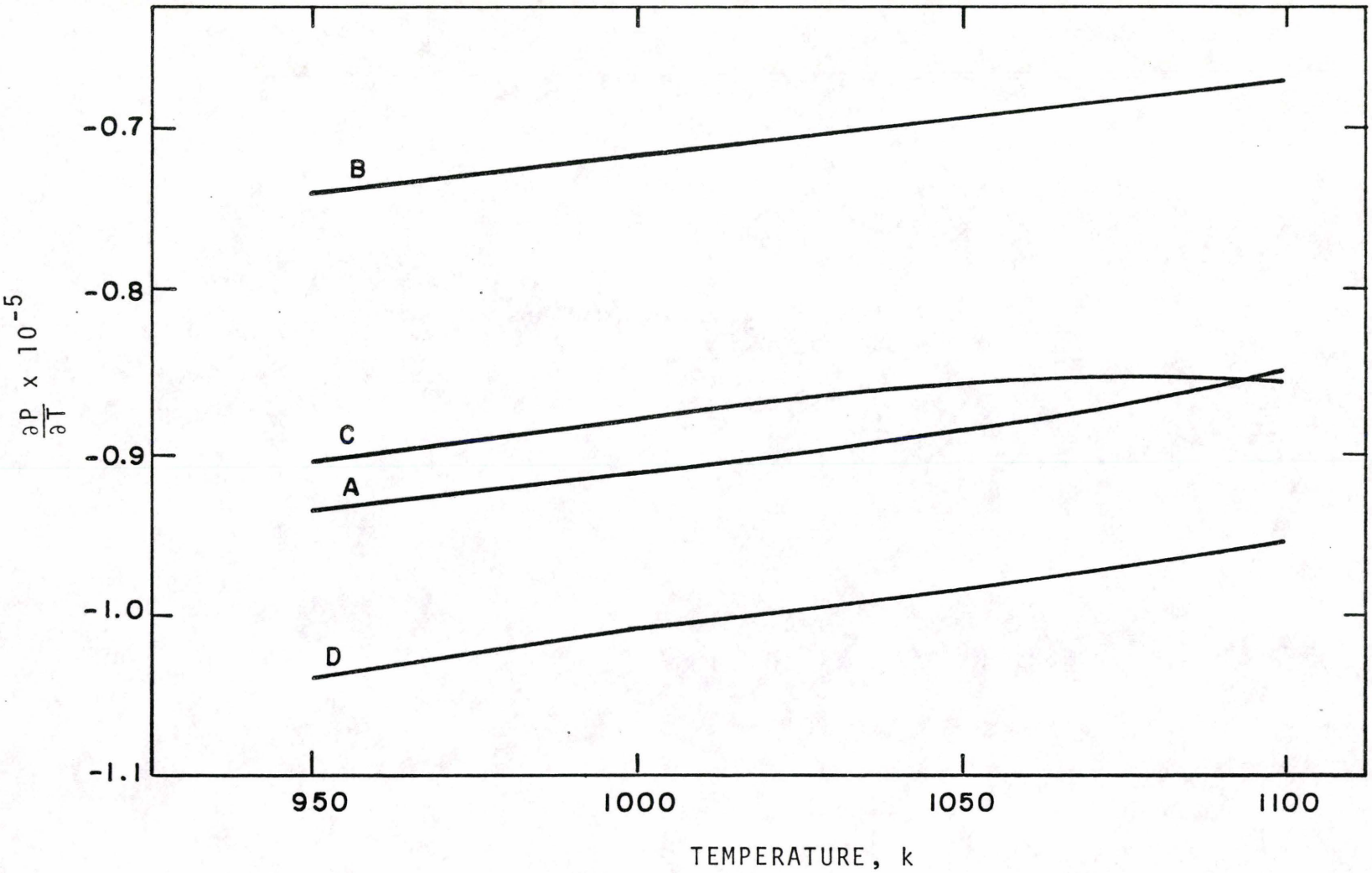

FIGURE 3.2 FUEL-TEMPERATURE COEFFICIENT OF REACTIVITY, $\frac{\partial P}{\partial T}$, AS A FUNCTION OF FUEL TEMPERATURE, T_F; FOR DIFFERENT CASES

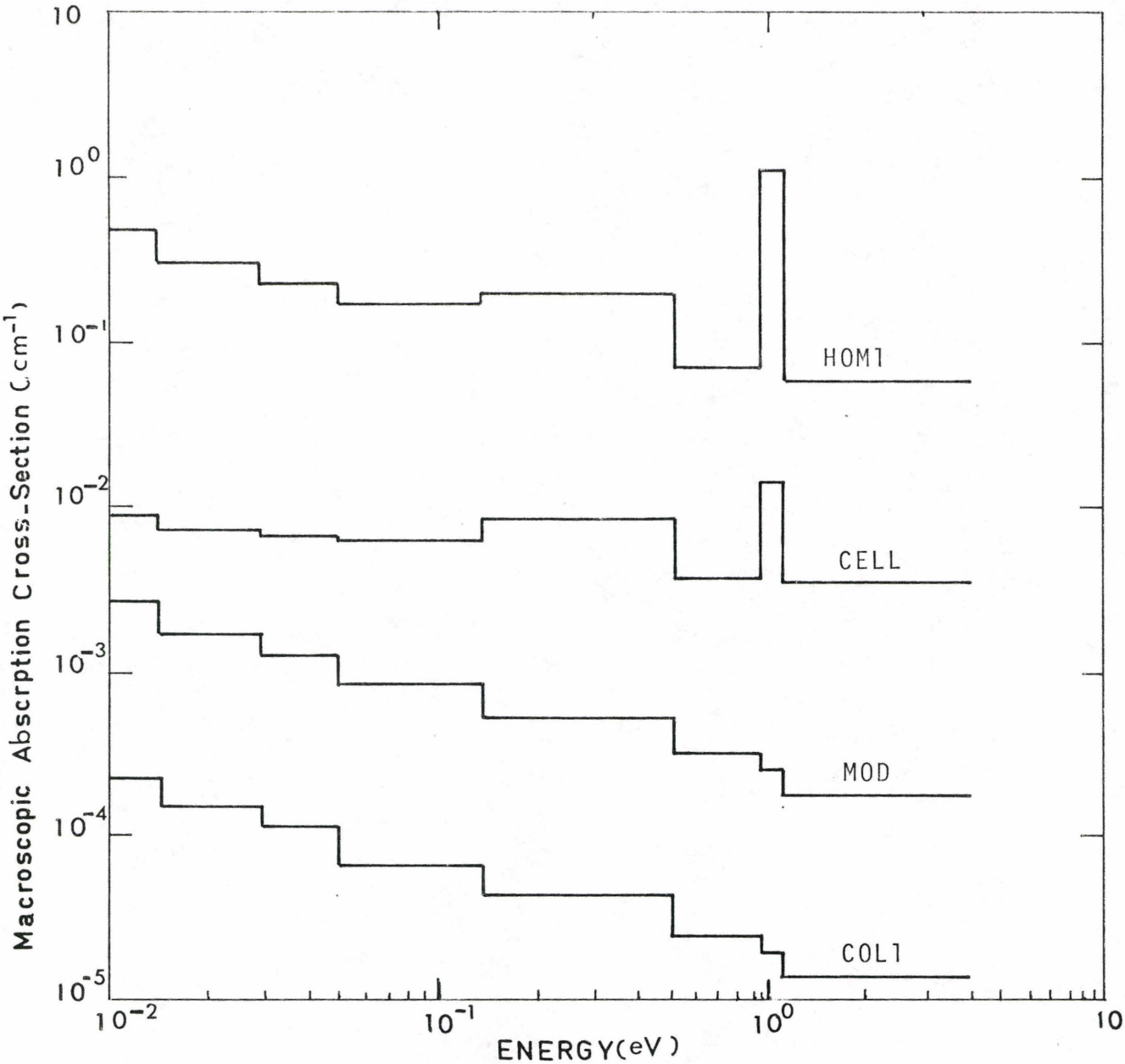

FIGURE 3.3 MACROSCOPIC ABSORPTION CROSS-SECTIONS FOR DIFFERENT MIXTURES AS A FUNCTION OF NEUTRON ENERGY. T_F = 1026 K, T_C = 566 K, THERMAL NEUTRON ENERGY REGION

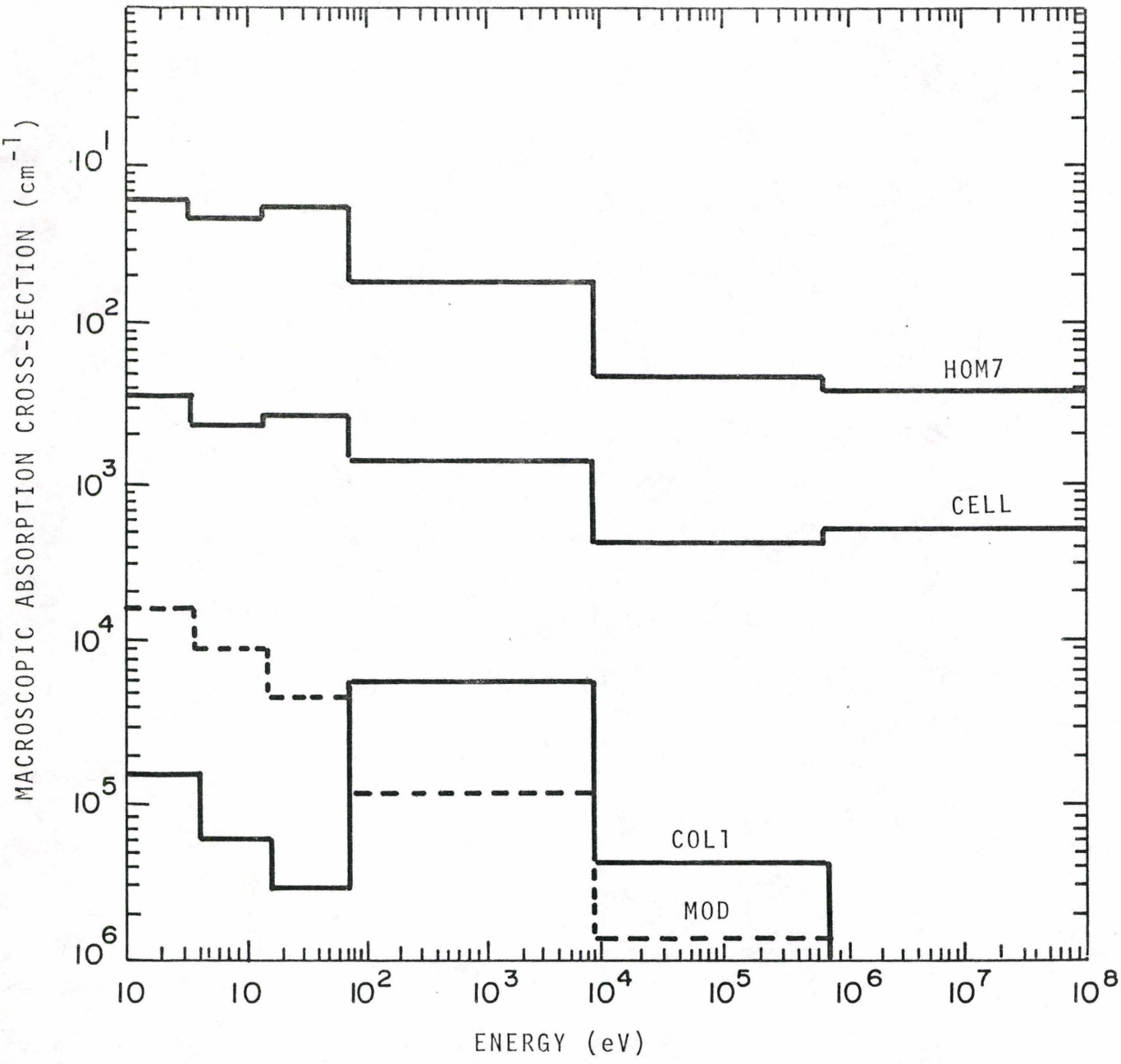

FIGURE (3.4) MACROSCOPIC ABSORPTION CROSS-SECTIONS FOR DIFFERENT MIXTURES AS A FUNCTION OF NEUTRON ENERGY. T_f = 1026 K, T_c = 566 K, FAST NEUTRON ENERGY REGION

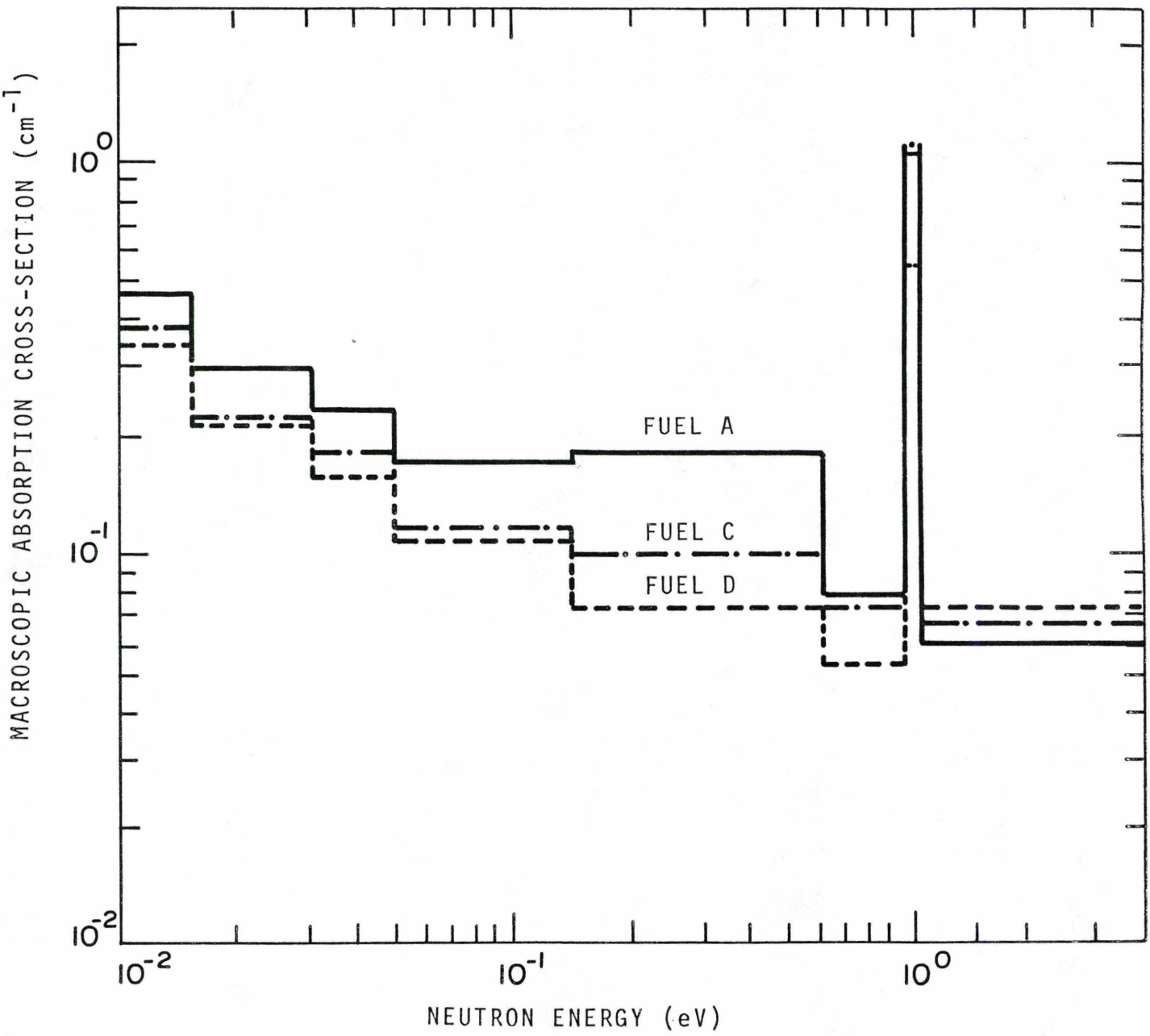

FIGURE 3.5 MACROSCOPIC ABSORPTION CROSS-SECTIONS FOR FUEL AT DIFFERENT IRRADIATIONS AS FUNCTION OF NEUTRON ENERGY. T_F = 1026 K, T_C = 566 K; THERMAL ENERGY REGION

TABLE (3.4)

FOUR FACTOR INTERPRETATION OF FUEL TEMPERATURE COEFFICIENTS OF REACTIVITY
FOR FRESH FUEL WITH BORON CONTROL

parameter	T_f = 926K	$\Delta x.10^5$	$\frac{1}{x} \cdot \frac{\partial x}{\partial T_f}\Big\|_{951K} .10^5$	T_f = 976K	$\Delta x.10^5$	$\frac{1}{x} \cdot \frac{\partial x}{\partial T_f}\Big\|_{1001K} .10^5$	T_f = 1026K
f	0.8195986	-3.54	- 0.086384	0.8195632	- 3.76	- 0.091756	0.8195256
η	1.4367758	+ 13.91	+ 0.193627	1.4369149	+ 14.76	+ 0.205440	1.4370625
p	0.8437920	- 49.30	- 1.168534	0.8432990	- 43.20	- 1.024547	0.8428670
ε	1.1008146	- 3.45	- 0.062681	1.1007801	- 3.24	- 0.058867	1.1007477
k_∞	1.0938050	- 61.472	- 1.124000	1.0931900	- 53.01	- 0.969761	1.0926599

TABLE (3.4) Continued

parameter	T_f = 1026K	$\Delta x.10^5$	$\frac{1}{x} \cdot \frac{\partial x}{\partial T_f}\Big\|_{1051K} .10^5$	T_f = 1076K	$\Delta x.10^5$	$\frac{1}{x} \cdot \frac{\partial x}{\partial T_f}\Big\|_{1101K} .10^5$	T_f = 1126K
f	0.8195256	- 3.58	- 0.087367	0.8194898	- 3.29	- 0.080294	0.8194569
n	1.4370625	+ 14.29	+ 0.198877	1.4372054	+ 15.22	+ 0.211800	1.4373576
p	0.8428670	- 42.10	- 0.998971	0.8424460	- 41.20	- 0.978104	0.8420340
ϵ	1.1007477	- 3.54	- 0.064320	1.1007123	- 2.79	- 0.050694	1.1006844
k_∞	1.0926599	- 52.00	- 0.9518	1.0921399	- 48.998	- 0.8972	1.0916499

TABLE (3.5)

FOUR FACTOR INTERPRETATION OF FUEL TEMPERATURE COEFFICIENTS OF REACTIVITY FOR FRESH FUEL

parameter	T_f = 926K	$\Delta x.10^5$	$\frac{1}{x} \cdot \frac{\partial x}{\partial T_f}\Big\|_{951K} .10^5$	T_f = 976K	$\Delta x.10^5$	$\frac{1}{x} \cdot \frac{\partial x}{\partial T_f}\Big\|_{1001K} .10^5$	T_f = 1026K
f	0.9657983	- 0.25	- 0.005177	0.9657958	- 0.25	- 0.005177	0.9657933
η	1.4351251	13.44	+ .187301	1.4352595	+ 15.08	+ 0.210136	1.4354103
p	0.8466270	- 44.5	- 1.051230	0.8461820	- 43.8	- 1.035238	0.8457440
ε	1.854396	- 3.10	- 0.057120	1.0854086	- 3.33	- 0.061359	1.0853753
k_∞	1.2737200	- 58.99	- 0.926263	1.2731301	- 56.7599	- 0.89166002	1.2725625

TABLE (3.5) continued

FOUR FACTOR INTERPRETATION OF FUEL TEMPERATURE COEFFICIENTS OF REACTIVITY FOR FRESH FUEL

parameter	T_f = 1026K	$\Delta x.10^5$	$\frac{1}{x} \cdot \frac{\partial x}{\partial T_f}\Big\|_{1051K} .10^5$	T_f = 1076K	$\Delta x.10^5$	$\frac{1}{x} \cdot \frac{\partial x}{\partial T_f}\Big\|_{1101K} .10^5$	T_f = 1126K
f	0.9657933	- 0.28	- 0.0057983	0.9657905	- 0.07	- 0.0014496	0.9657898
η	1.4354103	+ 13.28	+ .185034	1.4355431	+ 15.85	+ .2208223	1.4357016
p	0.845744	- 41.70	- 0.986114	0.845327	- 41.00	- 0.9700388	0.844917
ε	1.0853753	- 2.47	- 0.0455142	1.0853506	- 4.48	- 0.082554	1.0853058
k_∞	1.2725625	- 54.25	- 0.8536103	1.2720200	- 52.994	- 0.83322	1.2714901

TABLE (3.6)

FOUR FACTOR INTERPRETATION OF FUEL TEMPERATURE COEFFICIENTS
REACTIVITY FOR (MOL)

parameter	T_f = 926K	$\Delta x.10^5$	$\frac{1}{x} \cdot \frac{\partial x}{\partial T_f}\Big]_{951K} .10^5$	T_f = 976K	$\Delta x.10^5$	$\frac{1}{x} \cdot \frac{\partial x}{\partial T_f}\Big]_{1001K} .10^5$	T_f = 1026
f	0.9574967	- 2.07	- 0.04323	0.9574750	- 1.87	- 0.03906	0.9574573
η	1.1313547	+ 14.77	+ 0.26110	1.1315024	+ 14.54	+ 0.25700	1.1316478
p	0.8401390	- 42.10	- 1.00222	0.8397180	- 41.00	- 0.97652	0.8393030
ε	1.0817529	- 3.72	- 0.06878	1.0817157	- 3.6	- 0.06656	1.0816797
k_∞	0.9844990	- 41.998	- 0.85319	0.9840790	- 40.604	- 0.82522	0.9836730

TABLE (3.6) Continued

FOUR FACTOR INTERPRETATION FO FUEL TEMPERATURE COEFFICIENTS
REACTIVITY FOR (MOL)

parameter	T_f = 1026K	$\Delta x.10^5$	$\frac{1}{x} \cdot \frac{\partial x}{\partial T_f}\Big\|_{1051K}.10^5$	T_f = 1076K	$\Delta x.10^5$	$\frac{1}{x} \cdot \frac{\partial x}{\partial T_f}\Big\|_{1101K}.10^5$	T_f = 1126K
f	0.9574573	- 2.03	- 0.042403	0.9574370	- 1.74	- 0.036347	0.9574196
η	1.1316478	+ 14.66	+ 0.2590912	1.1317944	+ 15.13	+ 0.26736	1.1319457
p	0.8393080	- 40.10	- 9.95555	0.8389070	- 39.40	- 0.93932	0.8385130
ε	1.0816797	- 3.47	- 0.064159	1.0816450	- 3.45	- 0.06453	1.0816101
k_∞	0.9836730	- 39.502	- 0.803156	0.9832780	- 38.000	- 0.772920	0.9828980

TABLE (3.7) (a)

RELATIVE THERMAL ABSORPTION IN FRESH FUEL AT DIFFERENT FUEL TEMPERATURES

	T_f = 926 K	$\Delta x.10^4$	T_f = 1026 K	$\Delta x.10^4$	T_f = 1126 K
Xe-135	2.634677×10^{-2}	- 0.7456	2.627221×10^{-2}	- 0.737	2.619848×10^{-2}
Th-232	1.816000×10^{-1}	- 5.5200	1.810478×10^{-1}	- 3.4700	1.807015×10^{-1}
U-233	2.227218×10^{-1}	- 5.2580	2.221959×10^{-1}	- 5.1710	2.216788×10^{-1}
U-235	2.141414×10^{-2}	- 0.5687	2.135727×10^{-2}	- 0.5571	2-130156 $\times 10^{-2}$
Pu-239	2.689200×10^{-1}	+ 2.7600	2.691956×10^{-1}	+ 5.8780	2.696834×10^{-1}

TABLE (3.7) (b)

RELATIVE RESONANCE ABSORPTIONS FOR FRESH FUEL

AT DIFFERENT FUEL TEMPERATURES

	T_f = 926 K	$\Delta x.10^4$	T_f = 1026 K	$\Delta x.10^4$	T_f = 1126K
Xe-135	3.194433×10^{-6}	- 0.0001	3.188065×10^{-6}	- 0.0001	3.181729×10^{-6}
Th-232	4.892550×10^{-2}	+ 8.2040	4.974593×10^{-2}	+ 7.7756	5.052349×10^{-2}
U-233	2.951279×10^{-2}	- 0.6250	2.945029×10^{-2}	- 0.6055	2.938974×10^{-2}
U-235	1.568996×10^{-3}	- 0.0427	1.564721×10^{-3}	- 0.0409	1.560628×10^{-3}
Pu-239	9.109470×10^{-3}	- 0.0198	9.107489×10^{-3}	- 0.0235	9.105142×10^{-3}

TABLE (3.8) (a)

RELATIVE FAST NEUTRON ABSORPTION IN (MOL) FUEL
AT DIFFERENT FUEL TEMPERATURES

	T_f = 926 K	$\Delta x.10^4$	T_f = 1026 K	$\Delta x.10^4$	T_f = 1126 K
Xe-135	6.4057×10^{-15}	0.0000	6.5910×10^{-15}	0.0000	6.5953×10^{-15}
Th-232	1.4919×10^{-2}	- 0.0400	1.4915×10^{-2}	- 0.0800	1.4928×10^{-2}
U-233	2.1197×10^{-3}	0.0000	2.1197×10^{-3}	+ 0.0040	2.1202×10^{-3}
U-235	1.5201×10^{-4}	0.0000	1.5205×10^{-4}	+ 0.0005	1.5210×10^{-4}
Pu-239	9.9325×10^{-5}	- 0.0012	9.9201×10^{-5}	+ 0.0008	9.9275×10^{-5}

TABLE (3.8) (b)

RELATIVE RESONANCE ABSORPTIONS IN (MOL) FUEL

AT DIFFERENT FUEL TEMPERATURES

	T_f = 926 K	$\Delta x.10^4$	T_f = 1026 K	$\Delta x.10^4$	T_f = 1126 K
Xe-135	8.5160×10^{-7}	0.0000	1.8423×10^{-6}	0.0000	1.8407×10^{-6}
Th-232	4.8122×10^{-2}	+ 9.0300	4.9025×10^{-2}	+ 7.7500	4.9801×10^{-2}
U-233	2.4587×10^{-2}	- 0.3910	2.4548×10^{-2}	- 0.4460	2.4503×10^{-2}
U-235	1.4132×10^{-3}	- 0.3450	1.4097×10^{-3}	- 0.3180	1.4066×10^{-3}
Pu-239	9.3456×10^{-4}	- 0.0390	9.3162×10^{-4}	- 0.0100	9.3057×10^{-4}

TABLE (3.8) (c)

RELATIVE THERMAL ABSORPTIONS IN (MOL) FUEL

AT DIFFERENT FUEL TEMPERATURES

	T_f = 926 K	$\Delta x.10^4$	T_f = 1026 K	$\Delta x.10^4$	T_f = 1126 K
Xe-135	2.15180×10^{-2}	- 0.6200	2.14560×10^{-2}	- 0.3100	2.14250×10^{-2}
Th-232	2.54457×10^{-1}	- 3.3340	2.54124×10^{-1}	- 3.0883	2.53815×10^{-1}
U-233	2.77060×10^{-1}	- 3.1200	2.76748×10^{-1}	- 3.8000	2.76368×10^{-1}
U-235	2.80240×10^{-2}	- 0.5060	2.79734×10^{-2}	- 0.4205	2.79264×10^{-2}
Pu-239	3.82690×10^{-2}	+ 1.6100	3.84300×10^{-2}	+ 1.7100	3.86009×10^{-2}

TABLE (3.9)

RELATIVE THERMAL NEUTRON PRODUCTIONS IN FRESH FUEL AT DIFFERENT TEMPERATURES

	T_f = 926 K	$\Delta x.10^4$	T_f = 1026 K	$\Delta x.10^4$	T_f = 1126 K
U-233	5.070597×10^{-1}	- 12.0697	5.058529×10^{-1}	- 11.8539	5.046676×10^{-1}
U-235	4.462734×10^{-2}	- 1.2150	4.450584×10^{-2}	- 1.19618	4.438622×10^{-2}
Pu-239	5.262953×10^{-1}	+ 4.0106	5.266964×10^{-1}	+ 4.3890	5.271353×10^{-1}

3.2.b Discussions Based on the Four Factor Formula

To aquire a more sound understanding of the physical mechanisms which govern the behaviour of the fuel temperature coefficient of reactivity, the results are now discussed in terms of the four factor formula for k_∞:

$$k_\infty = f\eta p\varepsilon$$

The definitions of the factors used here are given in (1-6), and the upper boundary of the thermal region is arbitrarily chosen at 0.625 eV. The individual values of the parameters have significance only if comparisons with other calculations are to be carried out. The separation of the multiplication factor k_∞ into the four parameters f, η, p and ε is only justified in this context as a means of expressing the results of the detailed multigroup calculations and of understanding their physical significance.

(i) The Fast Fission Factor ε:

An increase in temperature tends to flatten the thermal flux in the fuel, because of the decreased absorptions in the thermal region; this in effect decreases the escape probability for thermal neutrons from the fuel regions increasing thermal productions. Fast absorptions remain almost constant with a change in temperature. As a consequence ε decreases with fuel temperature increase.

This argument could be followed by observing the absorptions in the different energy ranges from tables (3.7) and (3.8), where the absorptions of important nuclides in the fuel are shown normalized to one absorption in the total system, for the cases of fresh fuel and the case of (MOL).

It is quite notable that in the fast neutron energy range (above

9.118 KeV) there is almost no change in fast absorptions with the temperature change, while most of the changes take place in the resonance region (between 0.625 eV and 9.118 KeV) and in the thermal energy range (below 0.625 eV). It is interesting to note that thermal absorptions increase in Pu-239 and Pu-241 nuclides. The reason is that the thermal spectrum hardening enhances absorption in the Pu-239 resonance at 0.297 eV, with partial half widths of Γ_γ = 39 meV, Γ_f = 61 meV and Γ_r = 0.22 meV, and the Pu-241 resonance at 0.25 eV with Γ_γ = 43 meV, Γ_f = 59 meV and Γ_r = 0.055 meV [10], to absorb more thermal neutrons. However, changes in ε are generally small and contribute with about 5-8 percent of the total net effects on the fuel temperature coefficient of reactivity.

(ii) The Regeneration Factor η:

From table (3.9), which shows the thermal neutron production for the different fissile materials, we can see that the production rate for U-233, U-235, Pu-239, at different temperatures, is almost proportional to the absorption rate at the corresponding temperature. However, other non-fissile nuclides exist, which absorb neutrons at a decreasing rate with temperature causing the total value of η to increase with temperature. Hence η is expected to have a less positive cofficient of reactivity as the enrichment of the fuel increases.

(iii) The Resonance Escape Probability p:

The temperature dependence of the resonance escape probability p is entirely due to the resonance integral I. Increasing the fuel temperature increases the effective resonance integral through Doppler-broadening of the resonances in Th-232 and hence decreases the resonance escape probability p.

These deductions are qualified through observations of the increase of the resonance absorption of Th-232 in tables (3.7(b), (3.8)(b).

The presence of Boron in the moderator absorbs more thermal neutrons and hence more neutrons have higher energies causing more resonance absorptions. When the fuel temperature increases the Doppler-boradening effect becomes more notable in the fresh fuel with boron control case. This is evident from comparisons of tables (3.4) and (3.5).

(iv) The Thermal Utilization Factor f

From the tables shown one notices that changes in f with temperature are generally negative and small. The thermal diffusion length increases with temperature; and as the diffusion length increases, the flux in the fuel region tends to flatten, that is, the depression of the flux across the fuel region becomes less pronounced, and this leads to a smaller value of the thermal absorption in fuel relative to the total thermal absorptions in the system. It is seen from tables (3.7) and (3.8) that generally thermal absorptions in the fuel normalized to one absorption in the system, decreases with increasing temperature. However, there is a compensating effect of the Pu-239 which shows increased absorption with temperature due to its thermal resonance.

4. COOLANT TEMPERATURE COEFFICIENT OF REACTIVITY

4.1 General

The coolant temperature coefficient of reactivity describes the change in reactivity associated with a change in coolant temperature and includes the appropriate change in coolant density. The effect of the change in coolant flow area with coolant temperature is neglected, because it is gneerally small. An increase in coolant temperature results in a reduction in coolant density and in a hardening of the neutron spectrum due to increased upscattering from the light nuclides in the coolant.

4.2 Discussion of the Results

Generally the increase in η and p with temperature provides the major contribution to the positive coolant temperature coefficient of reactivity. When the coolant temperature increases and the neutron spectrum hardens, more neutrons are now absorbed in the Pu-239 thermal resonance. This explanation is confirmed by the relative thermal absorption rates given in Table (4.3)(a). Since the thermal resonance of Pu-239 has a large fission width, the corresponding thermal production increases with a corresponding increase in the value of η. The relative fraction of thermal absorptions in the system increases with temperature, which means an increase in the value of p with temperature. These effects are observed from table (3.1).

With increased irradiation the concentration of Pu-239 decreases due to burnup, and more thermal neutrons are now available for absorption by other nuclides. Thus the thermal absorption in Pu decreases while those in other nuclides increase with increased irradiation, as demonstrated by

tables (4.3)(a) and (4.4)(a). The ensueing effects are a decrease in the value of η and an increase in the value of p with increased irradiation as can be observed from tables (4.1)(b) and (4.1)(c).

The temperature coefficient of p decreases with irradiation from $+ 0.9923 \times 10^{-5} {}^{\circ}C^{-1}$ in the (MOL) case to $+ 0.7345 \times 10^{-5} {}^{\circ}C^{-1}$ in the (EOL) case.

For the fresh fuel condition with boron control in the moderator, the coolant temperature coefficient at 498 K becomes $1.8226 \times 10^{-5} {}^{\circ}C^{-1}$, for the (MOL) fuel case it becomes $2.61679 \times 10^{-5} {}^{\circ}C^{-1}$ while it becomes $2.7734 \times 10^{-5} {}^{\circ}C^{-1}$ for the (EOL) fuel case.

Table (4.1) shows the contributions to the temperature coefficient of reactivity from the four factors at different coolant temperatures. Table (4.2) shows the relative absorptions, in the thermal and resonance neutron energy ranges, for important nuclides at different temperatures and irradiation cases.

TABLE (4.1) (a)

FOUR FACTOR INTERPRETATION OF COOLANT TEMPERATURE COEFFICIENTS
IN FRESH FUEL WITH BORON CONTROL

Parameter	T_c = 473 K	$\Delta x.10^4$	$\frac{1}{x} \cdot \frac{\partial x}{\partial T_c}\Big\|_{498\ K} .10^5$	T_c = 523 K
f	0.8188737	+ 2.9440	+ 0.719036	0.8191681
η	1.4362787	+ 4.8110	+ 0.669926	1.4367598
p	0.8419420	+ 4.4800	+ 1.064206	0.8423900
ϵ	1.10037627	+ 1.947100	+ 0.353897	1.10057098
k_∞	1.0896300	+ 15.3000	+ 2.808293	1.0911600

TABLE (4.1) (b)

FOUR FACTOR INTERPRETATION OF COOLANT TEMPERATURE COEFFICIENTS IN (MOL) FUEL

Parameter	T_c = 473 K	$\Delta x.10^4$	$\frac{1}{x}\frac{\partial x}{\partial T_c}\Big\|_{498\ K}.10^5$	T_c = 523 K
f	0.95716521	+ 1.2674	+ 0.264824	0.95729195
η	1.13062667	+ 6.0968	+ 1.07848	1.13123635
p	0.83845400	+ 4.1600	+ 0.9923	0.83887000
ϵ	1.08137015	+ 1.5604	+ .28860	1.08152619
k_∞	0.98120420	+ 12.8880	+ 2.62697	0.98249300

TABLE (4.1) (c)

FOUR FACTOR INTERPRETATION OF COOLANT TEMPERATURE COEFFICIENTS
IN (EOL) FUEL

Parameter	T_c = 473 K	$\Delta x.10^4$	$\frac{1}{x}\frac{\partial x}{\partial T_c}\Big\|_{498\ K}.10^5$	T_c = 523 K
f	0.95400973	+ 0.9303	+ 0.195029	0.95410276
η	1.04227628	+ 2.6300	+ 0.504665	1.04253928
p	0.84407200	+ 3.1000	+ 0.734534	0.84438200
ϵ	1.08167798	+ 2.2084	+ 0.4083291	1.08189882
k_∞	0.90784800	+ 8.3666	+ 1.843172	0.90868466

TABLE (4.2) (a)

RELATIVE THERMAL ABSORPTION IN FRESH FUEL

WITH BORON CONTROL

	T_c = 473 K	$\Delta x.10^4$	T_c = 523 K
Xe-135	2.208261×10^{-2}	+ 4.9715	2.257977×10^{-2}
Th-232	1.528079×10^{-1}	+ 33.9017	1.5619812×10^{-1}
U-233	1.875487×10^{-1}	+ 42.1311	1.917618×10^{-1}
U-235	1.802093×10^{-2}	+ 3.8951	1.841044×10^{-2}
Pu-239	2.289790×10^{-1}	+ 67.3065	2.357097×10^{-1}

TABLE (4.2)(b)

RELATIVE RESONANCE ABSORPTION IN FRESH FUEL
WITH BORON CONTROL

	T_c = 473 K	$\Delta x.10^4$	T_c = 523 K
Th-232	5.051475×10^{-2}	+ 1.1841	5.063316×10^{-2}
U-233	2.925717×10^{-2}	+ 4.2424	2.968141×10^{-2}
U-235	1.554834×10^{-2}	+ 0.2155	1.576382×10^{-3}
Pu-239	9.064095×10^{-3}	+ 1.2010	9.184190×10^{-3}

TABLE (4.3)(a)

RELATIVE THERMAL ABSORPTION IN (MOL) FUEL

	T_c = 473 K	$\Delta x.10^4$	T_c = 523 K
Th-232	2.572121×10^{-1}	- 2.2562	2.569864×10^{-1}
U-233	2.895630×10^{-1}	- 1.0746	2.894556×10^{-1}
U-235	2.827216×10^{-2}	- 0.4092	2.823124×10^{-2}
Pu-239	3.775647×10^{-2}	+ 4.6766	3.822413×10^{-2}

TABLE (4.3)(b)

RELATIVE RESONANCE ABSORPTION IN (MOL) FUEL

	T_c = 473 K	$\Delta x.10^4$	T_c = 523 K
Th-232	4.719041×10^{-2}	- 4.0523	4.678518×10^{-2}
U-233	1.181524×10^{-2}	+ 0.3009	1.184533×10^{-2}
U-235	1.170550×10^{-3}	+ 0.0276	1.173310×10^{-3}
Pu-239	8.077277×10^{-4}	+ 0.02086	8.098138×10^{-4}

TABLE (4.4) (a)

RELATIVE THERMAL ABSORPTION IN (EOL) FUEL

	T_c = 473 K	$\Delta x.10^4$	T_c = 523 K
Th-232	2.829107×10^{-1}	- 0.4994	2.828608×10^{-1}
U-233	3.190773×10^{-1}	+ 1.0817	3.191855×10^{-1}
U-235	3.155375×10^{-2}	- 0.2443	3.152932×10^{-2}
Pu-239	9.276658×10^{-4}	+ 0.1449	9.421583×10^{-4}

TABLE (4.4)(b)

RELATIVE RESONANCE ABSORPTION IN (EOL) FUEL

	T_c = 473 K	$\Delta x.10^4$	T_c = 523 K
Th-232	4.640199×10^{-2}	- 4.0307	4.599892×10^{-2}
U-233	1.143967×10^{-2}	+ 0.2693	1.146659×10^{-2}
U-235	1.143759×10^{-3}	+ 0.0250	1.146254×10^{-3}
Pu-239	1.789867×10^{-5}	- 0.0813	0.976576×10^{-5}

5. COOLANT VOID COEFFICIENT OF REACTIVITY

The coolant void coefficient of reactivity is normally defined as the change in reactivity per percent voids in the coolant. The total change in reactivity if the coolant is completely removed is often called the void effect.

In the calculation of the void effect, the reactivity is calculated with the coolant present and with the coolant absent; and the void effect is calculated as the difference of the corresponding reactivities. In order to demonstrate the influence of the different factors in the four factor formula, the following procedure is followed.

Since $k_\infty = \varepsilon p \eta f$

then $\Delta k_\infty = \Delta\varepsilon\bar{p}\bar{\eta}\bar{f} + \bar{\varepsilon}\Delta p\bar{\eta}\bar{f} + \bar{\bar{\varepsilon}}\bar{p}\Delta\eta\bar{f} + \bar{\bar{\varepsilon}}\bar{\bar{p}}\bar{\eta}\Delta f$

where average values are used. The reactivity $\Delta\rho$, due to total voiding can be expressed as follows:

$$\Delta\rho = \left(\frac{\Delta\varepsilon}{\varepsilon_1+\varepsilon_2} + \frac{\Delta p}{p_1+p_2} + \frac{\Delta\eta}{\eta_1+\eta_2} + \frac{\Delta f}{f_1+f_2} + \frac{\Delta P_{n\ell}}{P_{n\ell 1}+P_{n\ell 2}}\right)\left(\frac{k_1+k_2}{k_1 k_2}\right) \qquad (5.1)$$

where the indices 1 and 2 refer to with coolant present and without coolant respectively.

It is to be expected that in case of k very close to unity, the last erm reduces to 2.0 and (5.1) would be the same as equation (1.5) derived before. The effect of changes in the non-leakage probabilities is not studied here.

From table (5.1), it can be noted that the values of f and p increase when the coolant is removed. The changes in f and p form the largest contributions to the void effect. The contribution from ε is always positive while that from η is negative.

Voiding of the coolant tends to soften the thermal neutron spectrum with the consequent loss of thermal absorptions in the thermal resonance of Pu-239 and an increase of thermal absorptions in other nuclides, as it is evident from tables (5.1) (a) (5.2) (a), (5.3)(a).

The thermal fissions decrease with loss of coolant due to the decrease in the Pu-239 thermal resonance absorption. On the other hand voiding increases absorption in the fuel for the energy band above the resonance region due to reduced macroscopic coolant cross-section. Consequently, ε increases with voiding as depicted by table (5.1).

The change in resonance escape probability can be discussed qualitatively on the basis of the familiar expression (11):

$$p = \exp - \left[\frac{N^\circ V^\circ}{\sum_i V^i \xi^i \Sigma^i_{n,pot}} \cdot I_{eff} \right] \qquad (5.2)$$

where N° : number density of absorber atoms

V° : volume of fuel region

$V^i, i=1,\ldots,n$: volume of slowing down region i

$\xi^i, i=1,\ldots,n$: Average logarithmic energy decrement for slowing down region i

$\Sigma^i_{n,pot}$: Macroscopic potential scattering cross-section for slowing down region i

I_{eff} : Effective resonance integral.

The effective resonance integral can be written as (1)

$$I_{eff}(T) = [A+B\sqrt{\frac{S^\circ(1-C)}{M^\circ}}\,]\,[1+\beta_I\,(T - T_o)] \qquad (5.3)$$

where A,B Material dependent parameters

S° Surface area of fuel pin

M° Mass of fuel pin

C Dankoff-correction factor

$\beta_I = c+d(\frac{S^\circ}{M^\circ})$ = roughly a constant (1), (12).

T Temperature in degrees Kelvin

T_o Reference temperature in K

A reduction in coolant density reduces the macroscopic cross-section of the moderator and hence increases the Dancoff-correction factor (table 2.9, ref. (12)). This decreases the resonance integral and consequently increases the resonance escape probability. This is shown in table (5.1). However, the change in the resonance escape probability is dependent on the relative magnitude of change in the resonance integral and the slowing down per absorber atom.

Setting $$\frac{N^\circ V^\circ}{\sum_i V^i \xi^i \Sigma^i_{n,pot}} = \frac{1}{X} \qquad (5.3)$$

Then, $$p = \exp - (\frac{I_{eff}}{X}) \qquad (5.4)$$

And, $$dp = \exp - (\frac{I_{eff}}{X}) \cdot \frac{1}{X^2}\,(I_{eff}\,dX - X dI_{eff}) \qquad (5.5)$$

For well moderated lattices, i.e. large X, the negative change in the effective resonance integral dominates and the resonance escape

probability increases with decreasing coolant density, whereas for highly undermoderated cells, i.e. small x, a change in coolant density makes an appreciable change to the slowing down per resonance absorber atom and the resonance escape probability decreases with coolant density.

The large increase in f noticed from table (5.1) is essentially due to the increase in absorption of the fuel with voiding as explained before.

The decrease in the value of η, as shown in table (5.1), is due to the loss of thermal absorptions in the Pu-239 thermal resonance and the consequent decrease in thermal neutron production; as in tables (5.1) (a), (5.2)(a), (5.3)(a).

For fresh fuel case, with boron control in the moderator, the total void effect amounts to 12.0274 mk. For (MOL) case, the total void effect is 11.9706 mk; while for (EOL) fuel case the corresponding value is 8.4875 mk.

The main reason for the smaller void effect for the (EOL) case as compared with the (MOL) case, is the large reactivity loss at the Pu-239 thermal resonance thorough softening of the neutron spectrum. This can be seen from tables (5.2), (5.3) and (5.4).

TABLE (5.1) (a)

FOUR FACTOR INTERPRETATION OF THE COOLANT VOID EFFECT
FOR FRESH FUEL WITH BORON CONTROL

PARAMETER	T_c=473 K	$\Delta X \cdot 10^3$	VOID EFFECT CONTRIBUTION $\cdot 10^3$	NO COOLANT
f	0.819527	+6.172	+6.817	0.825699
η	1.437059	-3.169	-2.006	1.433890
p	0.842867	+6.181	+6.639	0.849048
ε	1.100748	+2.033	+1.677	1.102781
K_∞	1.092660	+15.900	+13.127	1.10856

TABLE (5.1) (b)

FOUR FACTOR INTERPRETATION OF THE COOLANT VOID EFFECT FOR (MOL) FUEL

PARAMETER	T_c=473 K	$\Delta X \cdot 10^3$	VOID EFFECT CONTRIBUTION $\cdot 10^3$	NO COOLANT
f	0.957580	+2.403	+2.535	0.959983
η	1.131643	-2.101	-1.661	1.129542
p	0.839602	+5.129	+6.161	0.844731
ε	1.081783	+2.116	+1.977	1.083899
K_∞	0.984234	+8.693	+8.895	0.992827

TABLE (5.1) ($_c$)

FOUR FACTOR INTERPRETATION OF THE COOLANT
VOID EFFECT FOR (EOL) FUEL

PARAMETER	T_c=473 K	$\Delta X \cdot 10^3$	VOID EFFECT CONTRIBUTION $\cdot 10^3$	NO COOLANT
f	0.954359	+2.580	+2.954	0.956939
η	1.042747	-0.528	-0.554	1.042219
p	0.844938	+3.770	+4.871	0.848708
ϵ	1.082208	+2.340	+2.372	1.084557
K_∞	0.909968	+8.055	+9.642	0.918023

TABLE (5.2)(a)

THERMAL ABSORPTION IN FRESH FUEL WITH BORON CONTROL

	Tc = 473 K	$\Delta x.10^3$	without coolant
Th-232	1.550910×10^{-1}	+ 4.7404	1.598314×10^{-1}
U-233	2.026227×10^{-1}	+ 5.6435	2.082662×10^{-1}
U-235	1.8207231×10^{-2}	+ 0.5935	1.880074×10^{-2}
Pu-239	2.324618×10^{-1}	- 3.4735	2.289883×10^{-1}

TABLE (5.2)(b)

RESONANCE ABSORPTION IN FRESH FUEL WITH BORON CONTROL

	Tc = 473 K	$\Delta x.10^3$	without coolant
Th-232	4.694376×10^{-2}	- 4.8235	4.212019×10^{-2}
U-233	1.381239×10^{-2}	+ 0.5988	1.441124×10^{-2}
U-235	1.299963×10^{-3}	+ 0.0526	1.352604×10^{-3}
Pu-239	7.828417×10^{-3}	+ 0.156289	7.984706×10^{-3}

TABLE (5.3)(a)

THERMAL ABSORPTION IN (MOL) FUEL

	Tc = 473 K	$\Delta x.10^3$	without coolant
Th-232	2.569948×10^{-1}	+ 3.1530	2.601478×10^{-1}
U-233	2.895746×10^{-1}	+ 3.1076	2.926822×10^{-1}
U-235	2.822271×10^{-2}	+ 0.4190	2.864173×10^{-2}
Pu-239	3.857808×10^{-2}	- 1.1654	3.741268×10^{-2}

TABLE (5.3)(b)

RESONANCE ABSORPTION IN (MOL) FUEL

	Tc = 473 K	$\Delta x.10^3$	without coolant
Th-232	4.613100×10^{-2}	- 4.6090	4.152971×10^{-2}
U-233	9.831298×10^{-3}	+ 2.5024	1.233369×10^{-2}
U-235	1.178232×10^{-3}	+ 0.0406	1.218793×10^{-3}
Pu-239	8.135709×10^{-4}	+ 0.0284	8.419675×10^{-4}

TABLE (5.4)(a)

THERMAL ABSORPTION IN (EOL) FUEL

	Tc = 473 K	$\Delta x.10^3$	without coolant
Th-232	2.829779×10^{-1}	+ 2.2360	2.852139×10^{-1}
U-233	3.194419×10^{-1}	+ 2.0769	3.215188×10^{-1}
U-235	3.152946×10^{-2}	+ 0.3154	3.184483×10^{-2}
Pu-239	9.535197×10^{-4}	- 0.0307	9.228653×10^{-4}

TABLE (5.4)(b)

RESONANCE ABSORPTION IN (EOL) FUEL

	Tc = 473 K	$\Delta x.10^3$	without coolant
Th-232	4.535278 x 10-2	- 4.5674	4.078539×10^{-2}
U-233	1.151661×10^{-2}	+ 0.4034	1.192005×10^{-2}
U-235	1.150894×10^{-3}	+ 0.0382	1.189085×10^{-3}
Pu-239	1.803630×10^{-5}	+ 0.0007	1.876119×10^{-5}

REFERENCES

1. J.R. Lamarch, Introduction to Nuclear Reactor Theory, Reading, Mass. A-W Pub. Co. (1966).

2. J.R. Askew, F.J. Fayer and P.B. Kemshell, A general description of the lattice code WIMS, Journal of the British Nuclear Energy Society, Oct. (1966).

3. J.R. Askew and R.J. Brissenden Some improvements in the discrete ordinate method of B.G. Carlson for solving the neutron transport equation. AEE-R 161, 1963.

4. Benoist, P.A. Simple new expression of the radial diffusion coefficient for fuelled channels. AEEW Trans. 4, 1962.

5. Egelstaff, P.A., The treatment of thermal neutron scattering law data. EANDC(UK)1, 1960.

6 Nelkin, M.S., Scattering of slow neutrons by water, Phys. Rev., 1960, 119, 741.

7. Egelstaff, P.A., The physics of the thermal neutron scattering law, AERE-NP/GEN 29, 1962.

8. Honeck, H., An incoherent thermal scattering mode for heavy water. Trans. Am Nucl. Soc., 1962, 5, 47.

9. M.J. Roth, J.D. Macdougall, P.B. Kemshell, The preparation of input data for WIMS, AEEW-R 538, 1967.

10. Neutron cross-sections, BNL 325, Donald J. Hughes and Robert B. Schwartz, July (1958).

11. D. Hamel, Reactivity coefficients in a natural uranium carbide fuelled, heavy water moderated, organic liquid cooled reactor, AECL-4440, Nov. 1973.

12. Nuclear Reactor Theory, G.I. Bell and S. Glasstone, Van Nostrand Reinhold Company, 1970.

VALIDITY OF BRAGG STOPPING CROSS-SECTION ADDITIVITY RULE FOR SiC

by

Nasr M. Ghoniem

PART B: MCMASTER (ON-CAMPUS) PROJECT*

A Report Submitted to the School of Graduate Studies

in Partial Fulfilment of the Requirements

for the Degree

Master of Engineering

Department of Engineering Physics

McMaster University

Hamilton, Ontario, Canada

May 1974

*One of two Project Reports: The other part is designated PART A: INDUSTRIAL PROJECT

MASTER OF ENGINEERING (1974)
Department of Engineering Physics

MCMASTER UNIVERSITY
Hamilton, Ontario.

TITLE: VALIDITY OF BRAGG STOPPING CROSS-SECTION ADDITIVITY RULE FOR SiC

AUTHOR: Nasr M. Ghoniem

SUPERVISORS: Dr. D.A. Thompson and Dr. J.E. Robinson

NUMBER OF PAGES: ii, 70

ACKNOWLEDGEMENT

I wish to express my thanks and deep gratitude to Dr. D.A. Thompson, Department of Engineering Physics, for his continuous help and guidance during the course of this work. Also, I would like to thank Dr. J.E. Robinson, Department of Engineering Physics, for his supervision and Dr. A.B. Campbell, Department of Engineering Physics, for his experimental assistance on the Van-de-Graaff Accelerator.

ABSTRACT

This work has been done with the purpose of studying the validity of Bragg Kleeman rule which states that for combinations of elements, the atomic stopping cross-sections are additive. The validity of Bragg Kleeman rule for low energy He ions has not been conclusively tested for solids. In this work, the comparison with the experimental stopping power of SiC with the additive stopping powers of Si and C has been made experimentally.

A thick target technique in the experimental evaluation of the stopping powers is used. This method has some simplicity over the thin target techniques.

A calibration of the McMaster University Van-de Graff accelerator was done. Experiments were conducted later using the calibration curves produced.

The report contains a brief account on different sources of errors due to the Van-de-Graff accelerator calibration and due to stopping power experiments.

TABLE OF CONTENTS

CHAPTER 1

INTRODUCTION

Presented here is the experimental-theoretical technique of measurements of the stopping power of He ions in silicon, carbon and silicon carbide with initial energies ranging from 1.02 MeV to 2.22 MeV.

A modification of the technique originated by Wenzel and Whaling [1] and recently repeated by others[2] has been used. Due to the interest in the energy range of the ions from 1.0 MeV to 2.5 MeV for backscattering, channeling and radiation damage experiments, the Bethe-Bloch formalism of the stopping cross-sections with semiempirical modifications to comply with experimental data have been used. Others[3] have used the Lindhard-Winther formalism which is less relevent in the range of interest indicated, as will be shown later.

Recent measurements for other light elements[3],[4],[5] to generate fitting parameters for a semiempirical equation for the stopping cross-section dependence on energy have been used. The method followed is basically the Fletcher-Powell optimization method [6] with the aid of the "general program for discrete least pth approximation [7]. Optimality criteria indicated the good representation of chosen fitting function.

In the second chapter, a discussion of different theoretical models posed for the purpose of stopping cross-section evaluation is presented. The limits of applicability of each equation and the suitability of the Bethe-Bloch equation for the energy range of interest are discussed. Corrections

to the original Bethe-Bloch equation are discussed also and a presentation of a shell correction factor based on the idea of adjusted parameters like adjusted ionization potential is made.

In the third chapter, reference is made to the need for semiempirical type of calculations as a guide to experimental data rather than the absolute dependence on theoretical models. In this chapter, such criteria for optimization and acceptance of the semiempirical parameters are discussed.

In the fourth chapter, the energy calibration experiments are presented and a least-squares calibration curve is produced. The energy-calibration is based upon $^{4}Be(p,n)^{5}B$ reaction threshold and the $Al^{27}(p,\gamma)Si^{28}$ resonances. Sources of error are also indicated.

In the fifth and sixth chapters, a determination is done for the stopping cross-sections using the thick target technique and the semiempirical curves produced before. The merits of thick target technique are discussed. The incorporation of theory with experimentally available information gave more reliable data.

CHAPTER II

THEORETICAL STOPPING CROSS-SECTION MODELS

2.1 He Ions Energy Loss

He ions traversing matter may lose energy by the following interactions [8]:

(a) Excitation and ionization of the electrons in the atoms and molecules of the absorbing material are the dominant mode of loss by moderate and low energy He ions.

(b) Inelastic nuclear collisions become quite significant at high He ion energies and contribute heavily to the total energy loss.

(c) Elastic interactions occur, in which the He ion transfers kinetic energy to the struck atom.

(d) Photon emission due to particle deceleration in atomic fields is the least important of the He ion energy-loss process. This interaction is commonly called Bremsstrahlung.

For the high-energy region (approximately more than 1 MeV) the well known Bethe equation is applicable while for the low energy range (approximately less than 0.4 MeV) the Lindhard-Winther formalism is applicable. For the high energy range, a correction for the nonparticipating inner shell electrons can be made. The contribution of elastic nuclear collisions to the total energy loss is less than 0.1 per cent at 0.1 MeV and is even less significant at higher kinetic energies. For that reason, such elastic collisions have not been considered.

When it is compared with the ionization and excitation energy loss,

He ion Bremsstrahlung is completely negligible at the energies considered here and so has not been included. For instance, emission of virtual photons and Bremsstrahlung is only a fraction of 1 per cent at 10 BeV, drops sharply at lower energies, and is insignificant at the minimum ionization energy, which depends on target material (2.182 BeV for Al).

2.2 The Lindhard-Winther Equation

The energy loss of a fast moving heavy particle of charge $Z_1 e$, with velocity v, in a uniform electron gas of density n, is given by:

$$\frac{dE}{dx} = \frac{-4 \pi Z_1^2 e^4}{mv^2} \; n \; L(n,v) \qquad (2\text{-}1)$$

where L(n,v) is a dimensionless number and is a function of the electron density, n, and ion velocity, v. For the high velocity limit, L has the form of $\log(\frac{2 mv^2}{I})$, and $\frac{dE}{dx}$, therefore, has the form of Bethe-Bloch type energy loss. At the low velocity limit, L has a v^3 dependence and $\frac{dE}{dx}$ is proportional to the ion velocity.

For a fast ion moving in a medium of N atoms/cm^3, each stopping atom has a spherical average electron density $\rho(r)$. The stopping cross-section can be written as:

$$\varepsilon \equiv \frac{-1}{N} \frac{dE}{dx} = \frac{4 \pi Z_1^2 e^4}{mv^2} \int \rho(r) \; L(\rho,v) \; 4 \pi r^2 dr \qquad (2\text{-}2)$$

The charge distribution part of the integrand of (2-2), $\rho(r) \; 4 \pi r^2$ is related to the wave functions of a given atom Z_2 by

$$4\pi r^2 \rho(r) = \sum_{n\lambda} \omega_{n\lambda} [P_{n\lambda}(r)]^2 \qquad (2\text{-}3)$$

where $\omega_{n\lambda}$ and $P_{n\lambda}(r)$ are the occupation number and the radial wave function of the $n\lambda$ orbital and it is normalized such that

$$\int 4\pi r^2 \rho(r) dr = Z_2$$

and the Hartree-Fock-Slater radial wave functions or the simpler Thomas-Fermi distributions can be used here.

The stopping number L in equations (2-1) and (2-2) has been studied in great detail by Lindhard and Winther using quantum mechanical perturbation treatments on a free-electron gas model. In order to find the asymptotic form of the function $L(\rho, v)$, we define the Fermi velocity, v_F, which relates to the Fermi energy, E_F, by

$$E_F = \frac{1}{2} m v_F^2 = \frac{h^2}{2m} (3\pi^2 \rho)^{2/3} \qquad (2\text{-}4)$$

At the low ion velocity ($v \lesssim v_F$), $L(\rho, v)$ is proportional to v^3, i.e. stopping is proportional to v.

$$L = C_1(X) \left(\frac{v}{v_F}\right)^3 = \left(\frac{X^2}{3}\right) C_1(X)\, y^{3/2} \qquad (2\text{-}5)$$

where

$$X^2 = \frac{e^2}{\pi h v_F}, \quad y = \frac{3^{1/2}}{X} \left(\frac{v}{v_F}\right) = \frac{2 m v^2}{h \omega_\rho}$$

and the analytic form of $C_1(X)$ is given as:

$$C_1(X) = \frac{1}{2\left(1 - \frac{X^2}{3}\right)^2} \left\{ \log \left[\frac{1 + \frac{2}{3} X^2}{X^2} \right] - \frac{1 - \frac{1}{3} X^2}{1 + \frac{2}{3} X^2} \right\} \qquad (2\text{-}6)$$

One can use (2-5) and (2-3) and numerically integrate (2-2) in order to obtain ε_α.

2.3 The Bethe-Bloch Equation

The Bethe Equation for the energy loss from atomic ionization and excitation is:

$$\frac{1}{N}\frac{dE}{dx} = \frac{4\pi Z_1^2 e^2 Z_2}{mc^2 \beta^2}\left\{\log_e \frac{2mc^2\beta^2}{I_{adj}(1-\beta^2)\sqrt{1+\frac{2m}{M\sqrt{1-\beta^2}}+\left(\frac{m}{M}\right)^2}} - \beta^2 - \frac{\sum_i C_i}{Z_2} - \frac{\Delta}{2}\right\} \qquad (2\text{-}7)$$

where

Z_1 = effective charge of the ion

C = velocity of light in vacuum

e = electronic charge in e.s.u.

m = rest mass of the electron

M_1 = rest mass of the impinging ion

N = number of atoms per cubic cm of the material

Z_2 = atomic number of the stopping material

I_{adj} = the adjusted ionization potential

β = ratio of the incident particle velocity to the velocity of light $\frac{v}{c}$

$\sum_i C_i$ = the sum of the effects of shell corrections on stopping power

Δ = the polarization effect correction term

The form of this equation published by Livingston and Bethe in 1937 [9] neglects the small effects of the square root term within the logarithm. This term is quite close to unity except at very high energies. For example, omission of the term increased the energy loss at 1000 MeV by only 0.017 per cent in Al [8]. For this reason, this term in the calculations done was neglected since the energy range of interest is less than 3 MeV.

In order that the derivation which results in equation (2-7) be valid, the energy transferred to an atomic electron must in general be greater than the binding energy of that electron in its atomic shell. This condition can be partially removed by appropriate use of the shell corrections discussed later.

The incident He ion must also be represented accurately by a point charge and a point mass. This is the case for all the energies presently under consideration. Although it is not a rigorous requirement, another useful indication of the low-energy validity of equation (2-7) is the numerical value of the logarithmic term, which should be greater than zero. This requires that the kinetic energy of the He ion be:

$$E > \frac{M}{m} \frac{I_{adj}}{4}$$

In all cases,studied, this is true for He ions with energies above 0-5 MeV. Now a discussion is made for two parameters relevent to our work. namely the polarization effect and the adjusted ionization potential.

(a) <u>The Polarization Effect</u>

The perturbation of the field of the passing He ion which is caused

by the electric polarization of the surrounding atoms results in a reduction of the energy lost by the charged particle. This effect has been discussed in detail by Fermi and others [10]. The energy loss is usually reduced by less than a per cent at very high energies. It is reported by J.F. Janni [8] that the stopping power for protons at 1000 MeV in copper is reduced by 0.5 per cent and is insignificant for very low density materials, such as gases, at standard temperature and pressure.

For elements having higher atomic numbers, the medium is less strongly polarized because most of the atomic electrons are more tightly bound.

In the calculations done exclusion of this effect is made in the range of interest based on the foregoing discussion.

(b) The Adjusted Ionization Potential

Reference [8] made a general survey and selected values of the adjusted ionization potential for elements from theoretical and experimental evaluations available from the literature.

Linear interpolation was used in some cases where the adjusted ionization potential was not known.

Theoretical estimates using hydrogenic wave functions and approximation techniques would be expected to give good results for very low atomic number elements.

The inconsistency and variance of the ionization potentials, and the fact that the experiment is a guide for theoretical work, made it possible to think in a factor to lump all the inconsistencies in the adjusted

ionization potential and the shell corrections.

A method will be described later which simplifies calculations with the final aim of experimental-theoretical harmony.

Many experimental determinations of the adjusted ionization potential are inaccurate because both the multiple scattering and non-participation of the inner shell electrons in the stopping process have not been accounted for with sufficient accuracy.

However, Bloch found that for elements with sufficiently large atomic numbers, the adjusted ionization potential should be proportional to the atomic number according to the following relation [11]:

$$I = K Z , \qquad K \approx 10$$

CHAPTER 3

PROPOSED SEMIEMPIRICAL METHOD FOR THE STOPPING CROSS-SECTION

3.1 Other Methods Used Previously

W.K. Chu and D. Powers [4] in 1969 assumed an empirical relation of the form $\varepsilon_\alpha = \frac{A}{E} \ln(BE)$ to exist for the stopping cross-section. A least squares fit was done for a portion of the experimental measurements. The parameters A and B and the region of validity of the curve was given. Defficiencies in the fit, i.e. accuracy, limitation of its range of applicability and the nonconsideration of theoretical models might affect its validity.

J.F. Ziegler and W.K. Chu [3] in 1973 combined previous calculations for the Lindhard-Winther theory with existing experimental values of stopping cross-sections, to produce semiempirical values of stopping cross-section for ^{4}He ions for all elements for the energy region of 400-4000 KeV.

The semiempirical method used here is different from proposed method and could be summarised as follows:

(a) The measured experimental values of the stopping cross-sections have been used in order to interpolate for the unmeasured values.

(b) For the low and mid-Z elements, an average of the experimental/theoretical ratio is made of nearby solid target values for each energy, and the unknown values are calculated by multiplying the theoretical values by these averages.

(c) For high-Z elements, it was found that full energy range

experimental values exist only for 4 elements, namely, Dy, Ta, W, Au. Also, an additional 5 elements, namely, Gd, Hf, Ir, Pt, Pb, have 2000 KeV values. So for all elements above Z = 58, a two-step approach was used. The full energy ratios were used to obtain the shape of the values to be calculated, with the 2000 KeV value normalized to unity. The magnitude of the curve was made by averaging the 2000 KeV ratios for nearby elements. The final value was made by multiplying, for each energy, the normalised shape average, by the magnitude average, and that by the theoretical ε_α value.

Analytic least squares polynomial fit to the semiempirical values were made on the form:

$$\varepsilon_\alpha = \sum_{i=0}^{5} a_i E^i \qquad (3\text{-}1)$$

Accuracy of Mentioned Methods

No way could be established to verify the accuracy of the proposed method, however, one may easily find the following defects:

(1) The ratios of experimental/theoretical values reported is by no means a guarantee of the method because it was noticed that with the increase of atomic number, especailly in light elements, there were fluctuations of this ratio.

(2) The analytic function described is a polynomial which has a large number of coefficients, typically six.

(c) The least squares method used does not allow one to have a uniform error throughout the whole energy range and might be

inefficient if compared with other methods based on optimization criteria.

(4) The use of the Lindhard-Winther incorporating Hartree-Fock-Slater isolated-atom wave functions for the target atoms is unjustified in the high energy range ($E > 1$ MeV) [8] and resort to Bethe-Bloch formalism should be done. Lindhard-Winther theory was found not accurate to 30% for ^{4}He in matter for the energy range 1.4 - 2.00 MeV [12], [5].

3.2 Optimization and Acceptance Criteria for the Semiempirical Method

3.2.1 General

Least pth approximation is preferred because of its advantages like flexibility, efficiency; its versatility with the use of gradient optimization methods, and its practicability.

Least pth approximation with a sufficiently large value of p can result in an optimal solution very close to the optimal minimax solution.

3.2.2 The Error Functions in the Generalised Least pth Objective

Define real error functions related to the upper and lower specifications, respectively, as follows:

$$e_u(\underset{\sim}{\phi},\psi) \triangleq W_u(\psi)\,[F(\underset{\sim}{\phi},\psi) - S_u(\psi)] \qquad (3\text{-}2)$$

$$e_l(\underset{\sim}{\phi},\psi) \triangleq W_l(\psi)\,[F(\underset{\sim}{\phi},\psi) - S_l(\psi)], \qquad (3\text{-}3)$$

where

$F(\underset{\sim}{\phi},\psi)$ is the approximating function (actual)

$S_u(\psi)$ is an upper specified function (desired)

$W_u(\psi)$ is an upper positive weighting function

$S_l(\psi)$ is a lower specified function (desired)

$W_l(\psi)$ is a lower positive weighting function.

3.2.3 Discrete Approximation

The functions evaluated in (2-2), (2-3) are evaluated at discrete values of ψ, therefore it is appropriate to consider discrete approximation. In this case, the error norm is defined as:

$$||\underset{\sim}{e}||_p \triangleq \left(\sum_{i\in I} |e_i(\underset{\sim}{\phi})|^P\right)^{\frac{1}{P}} \qquad 1 \leq P < \infty \qquad (3\text{-}4)$$

where

$$e(\underset{\sim}{\phi}) \triangleq (e_1(\underset{\sim}{\phi})\ e_2(\underset{\sim}{\phi})\ \ldots\ e_n(\underset{\sim}{\phi}))^T \qquad (3\text{-}4)$$

$$I \triangleq (1,2,\ \ldots\ ,\ n)$$

the process of minimizing $||\underset{\sim}{e}||p$ is called discrete least pth approximation. In the case of fitting a curve to experimental data, discrete approximation may be the only approach possible.

One notices here that in the special case when p=2 is set, one arrives at the well known least squares approximation.

In our analysis, we followed a two-way procedure; one was to choose a certain function and then increase the value of p, while the other was to fix a high value of p and then choose suitable conceivable types of function for the energy range of interest. Our acceptance criteria, however, is to find the least possible value of $||\underset{\sim}{e}||p$ irrespective of our way of search.

3.3 Computer Programs Used

Interested readers are referred to the sophisticated program in reference [13], however suitable modifications in the main program, the sub-routine FCTAPP, and the function FUNCS(X, IINT) were made and they are listed in Appendices [A], [B] and [C] respectively.

3.4 Results and Conclusions

3.4.1 Approach

As indicated before, if one uses the accurate quantum-mechanical theory, the result for the average rate of loss is as in equation (2-7). $C_K(1/n)$ is a correction term for binding in the K-shell, and

$$\eta = \frac{m E}{M(Z - \sigma)^2 R_y} = \left(\frac{v}{(Z - \sigma) v_o}\right)^2 \qquad (3\text{-}5)$$

where R_y = Rydberg constant

σ = screening constant (approximately 0.3 for light elements) such that $(Z - \sigma)e$ gives the effective source strength of the field in which the K electrons move.

In the low-energy range, the Born approximation for heavy materials would fail, since the inner electrons move at very high velocities compared to the incident ions, and a correction for binding in the inner electron shells must be applied. This is done by subtracting the number C_K from the logarithmic term in the Bethe-Bloch formula [9], [14]. The C_K corrections have been calculated by Walske [15] and a sample of his results is as follows:

Values of C_K for Carbon

Proton Energy (Mev)	C_K
0.6	0.900
0.8	0.972
1.0	0.981
1.2	0.951
1.4	0.901
1.6	0.852
1.8	0.800
2.0	0.758
2.2	0.716
2.4	0.678
2.6	0.638
2.8	0.597
3.0	0.570

A conversion of the energy of the proton into the corresponding energy of the He ion was done and a high degree polynomial to represent the values of C_K at any needed energy was used. However, inaccuracies in the theoretical stopping power might happen because of neglecting L, M, N and even O shells effect on the stopping phenomenon [8]. The procedure here followed the idea of adjusted parameters like the adjusted ionization potential to fit experimental data. For elements with close atomic numbers, like light elements in our case, one can accept the values of C_K for a medium Z element, multiplied by a correction factor to increase or decrease the amplitude of the C_K shape. The choice of a suitable correction factor is shown to compensate for the effect of other shells with adequate practical accuracy.

Fig. (1) is shown to manifest our approach. The Lindhard-Sharff theoretical model is shown to deviate greatly from experimental evaluations of the stopping cross-section even at a ^{4}He ion energy of 0.4 MeV. The Bethe-Bloch model is in good agreement with experimental results for high energies if one considers all the inner shell contributions. We varied the correction factor f, obtained different theoretical curves for the high energy region, fitted this analytical portion with best available experimental data for light elements in the low energy region [3], [4], [5], [8], [12] and we ended up with an accepted fitting function together with a suitable adjusted shell correction factor.

Our theoretical calculations were checked with those of J.F. Janni [8] for the case of proton stopping and were then extended for the case of He^+ ions. A FORTRAN IV program for the execution of theoretical calculations as in Appendix [D].

3.4.2 Results for Carbon, Si and Other Light Elements

(i) Carbon: (z = 6)

Table (3-1) Fitting Function: $A(1)XE + A(2)XE^2 + A(3)/E + A(4)/E^2$

Case No.	p	A(I)	||e||	Shell Correction Factor	|Max. Error| (MeV/cm)	Energy for Max. Error (MeV)
A	2	1641.2928 - 423.8346 3899.3055 -1089.2446	893.91926	1.350	441.9437	1.10
B	100	1885.7554 - 509.7386 3914.7927 -1115.1262	286.9473	1.350	284.289	1.10

Table (3-2) Fitting Function: $\frac{A(1)}{E} \log_e(A(2)XE)$

Case No.	p	A(I)	||e||	Shell Correction Factor	|Max. Error| (MeV/cm)	Energy for Max. Error (MeV)
A	2	3372.2520 3.6859	1397.6553	0.05	625.7513	1.10
B	100	3476.9394 3.9683	535.5507	0.05	531.4677	1.10
C	2	3058.1025 3.8978	735.2316	1.35	343.929	0.3868
D	100	3004.8029 3.6409	266.6094	1.35	264.5976	0.6646

Table (3-2) continued

Case No.	p	A(I)	||e||	Shell Correction Factor	|Max. Error| (MeV/cm)	Energy for Max. Error(MeV)
E	2	3049.6842 3.9056	726.1607	1.5	346.1055	0.3868
F	100	3000.6194 3.9716	273.4068	1.5	275.066	0.6646

Table (3-3) Fitting Function: $\frac{A(1)}{E} \log (A(2)XE) + A(3) + A(4)/E$

Case No.	p	A(I)	||e||	Shell Correction Factor	|Max. Error| (MeV/cm)	Energy for Max. Error(MeV)
A	2	305.8103 4.0041 0.0 -82.2190	735.231	1.35	343.929	0.3868
B	100	3004.8029 4.0785 -0.0 -82.2432	266.6094	1.35	264.597	1.10

Table (3-4) Fitting Function: $\frac{A(1)}{E} \log(A(2)X\sqrt{E})$

Case No.	p	A(I)	||e||	Shell Correction Factor	|Max. Error| (MeV/cm)	Energy for Max. Error(MeV)
A	2	6116.2051 1.9743	735.2317	1.35	343.929	0.3868
B	100	6009.6059 1.9921	266.6094	1.35	264.597	1.10

(ii) Silicon: (z = 14)

Table (3-5) Fitting Function: $\frac{A(1)}{E} \log_e(A(2)X\sqrt{E})$

Case	p	A(1)	||e||	Shell Correction Factor	|Max. Error| (MeV/cm)	Energy for Max. Error(MeV)
A	2	4146.6150 2.0675	536.7375	1.35	238.0822	0.558
B	100	4040.4882 2.0805	202.4576	1.35	200.6747	0.558

Table (3-6) Fitting Function: $A(1)XE + A(2)XE^2 + \frac{A(3)}{E} + \frac{A(4)}{E^2}$

Case No.	p	A(1)	||e||	Shell Correction Factor	|Max. Error| (MeV/cm)	Energy for Max. Error(MeV)
A	2	1238.2114 -290.5439 2516.7628 -626.8983	398.7133	1.2	215.6395	0.4570
B	100	1451.4769 -352.6531 2230.4630 -532.22146	128.2667	1.2	126.9814	0.4570
C	100	1463.1446 -352.7294 2220.4856 -529.0318	127.0044	1.35	125.7379	0.558
D	10,000	1467.2504 -354.1757 2218.200 0528.441	125.1742	1.35	125.1616	0.558

Table (3-7) Fitting Function: $\frac{A(1)}{E} \log_e(A(2)XE)$

Case No.	p	A(1)	||e||	Shell Correction Factor	|Max. Error| (MeV/cm)	Energy for Max. Error(MeV)
A	2	3748.6802 2.2667	915.206	1.35	545.8587	0.558
B	100	3718.3288	408.5799	1.35	405.7422	0.558

(iii) Other Light Elements - Element: Chromium

Table (3-8) Fitting Function: $A(1)XE + A(2)XE^2 + A(3)/E + \frac{A(4)}{E^2}$

Case No.	p		||e||	Shell Correction Factor	|Max. Error| (MeV/cm)	Energy for Max. Error(MeV)
A	2	1866.4296 -358.5016 7975.3750 -2590.6506	1272.647	0.5000	640.1835	1.10
B	100	2669.7028 -592.4148 6219.1098 -1543.5867	512.1625	0.5000	351.0	1.10

Table (3-9) Fitting Function: $A(1)XE + A(2)XE^2 + \frac{A(3)}{E} + \frac{A(4)}{E^2}$

Case No.	p	A(1)	||e||	Shell Correction Factor	|Max. Error| (MeV/cm)	Energy for Max. Error(MeV)
A	2	1137.3978 -286.7014 3155.2586 -866.6937	815.279	1.10	412.453	1.10
B	10	1115.3277 -295.6817 3433.7462 -1015.167	341.807	1.10	317.1311	1.10

Table (3-10) Fitting Function: $A(1)XE + A(2)XE^2 + \frac{A(3)}{E} + \frac{A(4)}{E^2}$

Element: Aluminum (z = 13)

Case No.	p	A(1)	||e||	Shell Correction Factor	|Max. Error| (MeV/cm(	Energy for Max. Error(MeV)
A	2	1498.5903 -350.3043 2680.3357 -674.0859	430.8776	1.35	151.037	1.10
B	100	1585.6345 -377.3379 2644.3094 -676.0116	123.5215	1.35	122.3419	1.10

Table (3-11) Fitting Function: $A(1)XE + A(2)XE^2 + A(3)/E + A(4)/E^2$

Element: Vanadium (z = 23)

Case No.	p	A(1)	||e||	Shell Correction Factor	|Max. Error| (MeV/cm)	Energy for Max. Error(MeV)
A	2	1251.5204 -222.4222 7964.8571 -2440.8343	1604.9369	-1.50	745.5665	1.10
B	10	3151.6622 -790.9572 4974.3751 -991.1833	679.647	-1.50	424.0	1.10

Table (3-12) Fitting Function: $A(1)XE + A(2)XE^2 + \frac{A(3)}{E} + \frac{A(4)}{E^2}$

Element: Magnesium (z = 12)

Case No.	p	A(1)	||e||	Shell Correction Factor	|Max. Error| (MeV/cm)	Energy for Max. Error(MeV)
	2	727.2314 -157.6849 2346.1951 -630.2697	175.8997	1.35	78.45	0.9228
	100	863.5656 -200.9679 2228.9009 588.8079	68.86	1.35	68.1465	0.4893

3.4.3 Conclusions

Out of the foregoing results, one can draw the following pertinent conclusions:

(1) Extensive study for different fitting functions for a representative group of light elements results in a suitable function on the form $(A(1)XE + A(2)XE^2 + \frac{A(3)}{E} + \frac{A(4)}{E^2})$ for all cases studied except carbon data which seems more likely to fit the form $(\frac{A(1)}{E} \log_e(A(2)XE))$ used before in reference [2], however, the difference in the error norm is not significant (Tables (3-1-B) and (3-2-D)).

(2) The results shown led us to consider the function $(A(1)XE + A(2)XE^2 + \frac{A(3)}{E} + \frac{A(4)}{E^2})$ as an efficient one for light elements. This is evident from the relatively small number of optimum coefficients used, the smaller values of the error norm and maximum error especially for higher values of p.

(3) The inner shells correction factor is found to be most effective for the highest atomic number element considered (Vanadium) and a value of - 1.5 has to be introduced. For close atomic number elements in the periodic table, an optimum adjusted value of 1.35 was found to be efficient. For the same element, a change from 0.05 to 1.50 did not produce drastic effect in the error norm and maximum error, (see Table (3-2) cases B,D,F.)

(4) Increase of the value of p is observed to reduce the acceptance levels, namely the error norm and maximum error, but showed saturation in effect for very large values of p. For this particular reason, most comparisons were done between the least squares case (p = 2) and a large value

of p (usually p = 100). Very large values of p like 10^6 might produce minimax solution (equal error over entire energy range) [13], however, this error cannot be less than relevent experimental error.

(5) As indicated by Fig. (2), and the result that most maximum errors are associated with the least value of energy considered theoretically, one is led to the acceptance of the Bethe-Bloch model and not the Lindhard-Winther model for our energy range of interest.

Measured energy dependence of the stopping cross-section for He^+ ions in Si

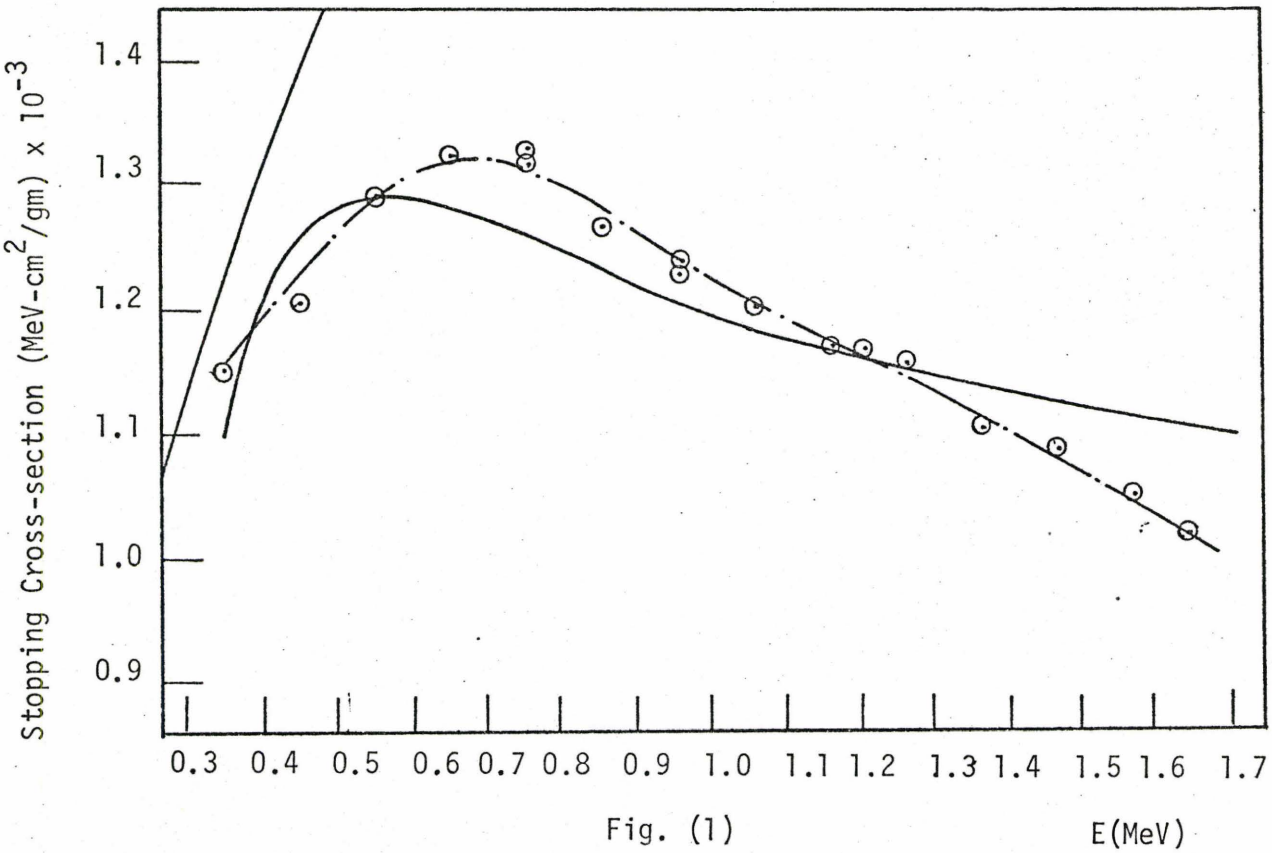

Fig. (1)

— Theoretical calculations using Lindhard Model

⊙ Experimental results, D.A. Thompson, et al. [5]

— Semiemperical calculations using Bethe-Bloch theoretical model and experimental data - f - 1.35

FIG·(2)

Sample Result, Silicon stopping power for He^4 ions

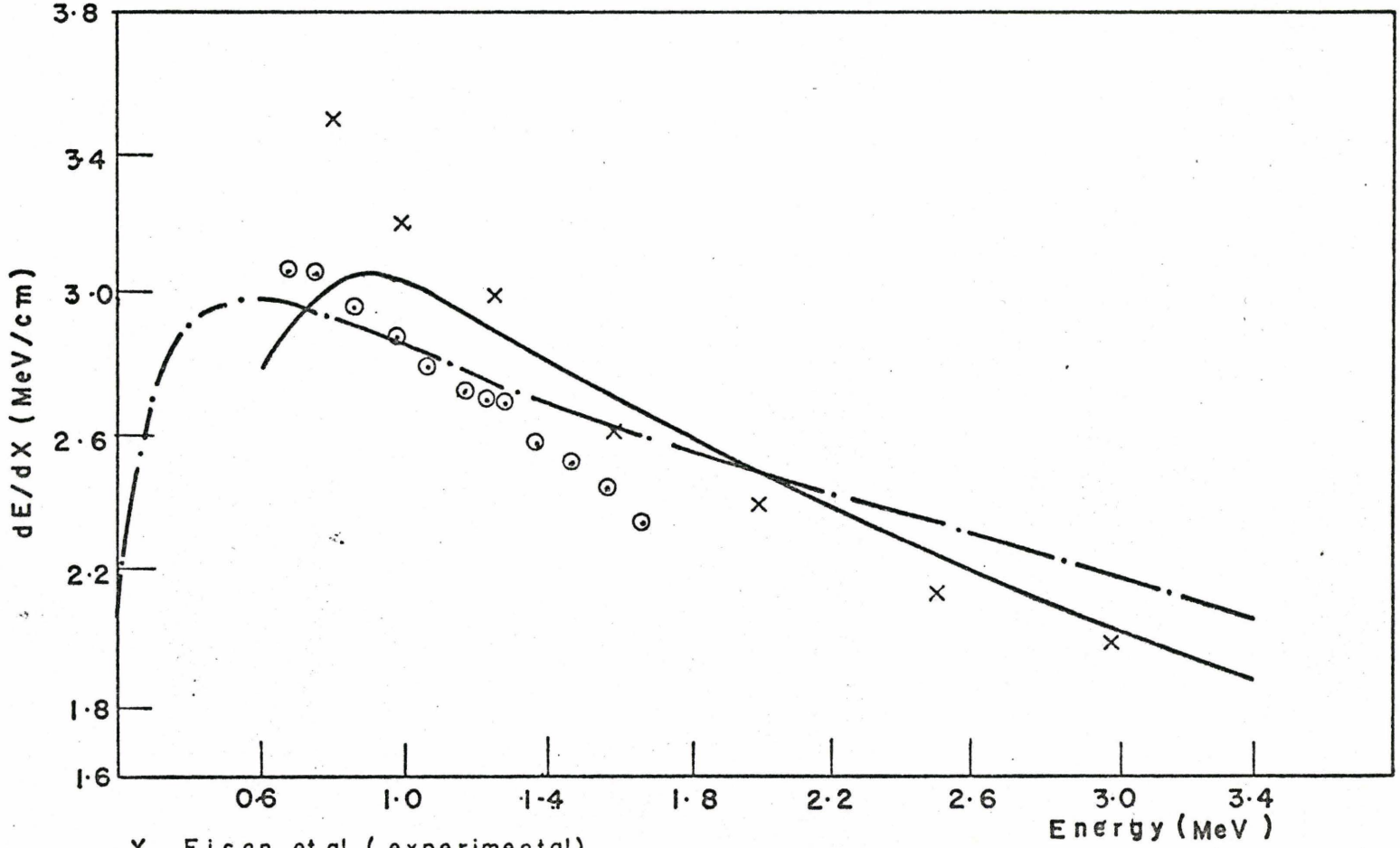

X Eisen et.al. (experimental)

⊙ Thompson et. al (experimental)

— Our theoretical Calculions, Bethe-Bloch model, shell factor = 1·35

—·— Our Semiempirical results, Shell factor = 1·35

CHAPTER 4

MCMASTER VAN-de-GRAAFF ENERGY CALIBRATION

4.1 Energy Calibration Methods [1]

The problem of energy calibration is of fundamental importance. There are several methods of the voltage measurements, however, the method used in this work involved the use of magnetic deflection of the particle beam to calibrate its energy. The Van-de-Graaff is a KN 3 MeV terminal voltage accelerator and the generating voltmeter is used to measure terminal voltage. However, for experiments sensitively dependent upon energy, the energy of the particle has to be known accurately.

The method calibrated the proton energy scale by nuclear resonances and nuclear threshold data. Certain reactions have extremely high resonances at definite proton energies, and the yields from such reactions show either sharp peaks or threshold values.

Two reactions were involved:

(a) Finding and detecting all possible resonances in the reaction $Al^{27}(p,\gamma)\ Si^{28}$.

(b) Finding the threshold value of proton energy in the reaction $_4Be^{9}(p,n)_5B^{9}$.

4.2 Experimental Arrangement

4.2.1 $Al^{27}(p,\gamma)\ Si^{28}$ Resonances

There are up to 40 known resonances in the $Al^{27}(p,\gamma)\ Si^{28}$ reaction, but with the present apparatus only 3 strong resonances could be detected.

Reference [16] indicates the presence of strong resonances at

E_p = 991.82 ± 0.1 KeV, E_p = 1381.3 ± 0.3 KeV and E_p = 1388.4 ± 0.3 KeV. There is another relatively strong resonance at E_p = 1118.4 ± 0.2 KeV.

The strength of the resonances is given by a parameter indicated as $\{(2J + 1)\,\Gamma_p\Gamma_\gamma/\Gamma^d\}$ which is proportional to the probability of proton absorption multiplied by the probability of gamma emission. This factor is important as to the selectivity of pertinent resonances, and is used as a guide as to the energy scale scanning in the calibration experiments.

Measurement of the magnetic field was carried out using a Gaussmeter, Bell Model 620. The Gaussmeter was zeroed and adjusted each measurement. Two different Gaussmeters were used for magnetic field measurement, one for the $_4Be^9(p,n)_4B^9$ threshold reaction, and a new one for $Al^{27}(p,\gamma)\,Si^{28}$ resonances detection. A correction of the readings of the old Gaussmeter is done as follows:

D.V. Reading	0.8	0.85	0.90	0.95	1.00	1.05	1.10	1.15	1.20	1.40	1.50
B_{old}(KG)	2.60	2.70	2.76	2.82	2.89	2.95	3.01	3.08	3.12	3.32	3.42
B_{new}(KG)	2.42	2.50	2.60	2.69	2.72	2.80	2.88	2.92	3.00	3.22	3.32
Difference (Gauss)	180	200	160	130	170	150	130	160	120	100	100

The average value of the difference = 147 gauss, hence we corrected the readings for the $_4Be^9(p,n)_4B^9$ threshold reaction by subtracting 147 gauss from each of them so that we use directly the new Gaussmeter.

The major difficulty in detecting the $Al^{27}(p,\gamma)\,Si^{28}$ resonances is the discrimination of the high level of background associated with the reaction.

It is known that the decay energy of the gamma quanta have a spread of values, however, energies below 1.78 MeV are not considered to correspond to the resonances of the reaction. For a complete analysis of the percentage branching from every excited state above 1.78 MeV one can look at reference [16]. With a gain of 50 of the spectroscopic amplifier, base line setting of 4.7, current of 100 NA, window setting of 0.3, we obtained the C_o^{60} standard source gamma spectrum shown in Fig. (4.1). The C_o^{60} standard source has two peaks at energies 1.173226 ± 0.04 MeV and 1.332483 ± 0.046 MeV respectively [17]. With the same settings indicated, we find from Fig. (4.1) that an energy of 1.173226 MeV occurs in channel #60 and an energy of 1.33248 MeV occurs in channel #80.

Supposing a linear relation between energy and channel number (which turned out to be a correct assumption as verified later in chapter 5), we can easily see that most of the gamma quanta coming out of this reaction will be recorded around channel #136. So the discriminator level and the width of the window were set to allow only gamma quanta of energy 1.78 MeV be recorded (see Fig. (4.3)). The discriminator level was set to correspond to channel #134.

The output gamma counts were taken after 40 μC integrated dose to allow good statistics. Fig. (4.2) shows the resulting spectrum. It was possible to detect only three strong resonances with relative strength consistent with $\{(2\,J + 1)\,\Gamma_p\Gamma_\gamma/\Gamma^d\}$ in reference [16].

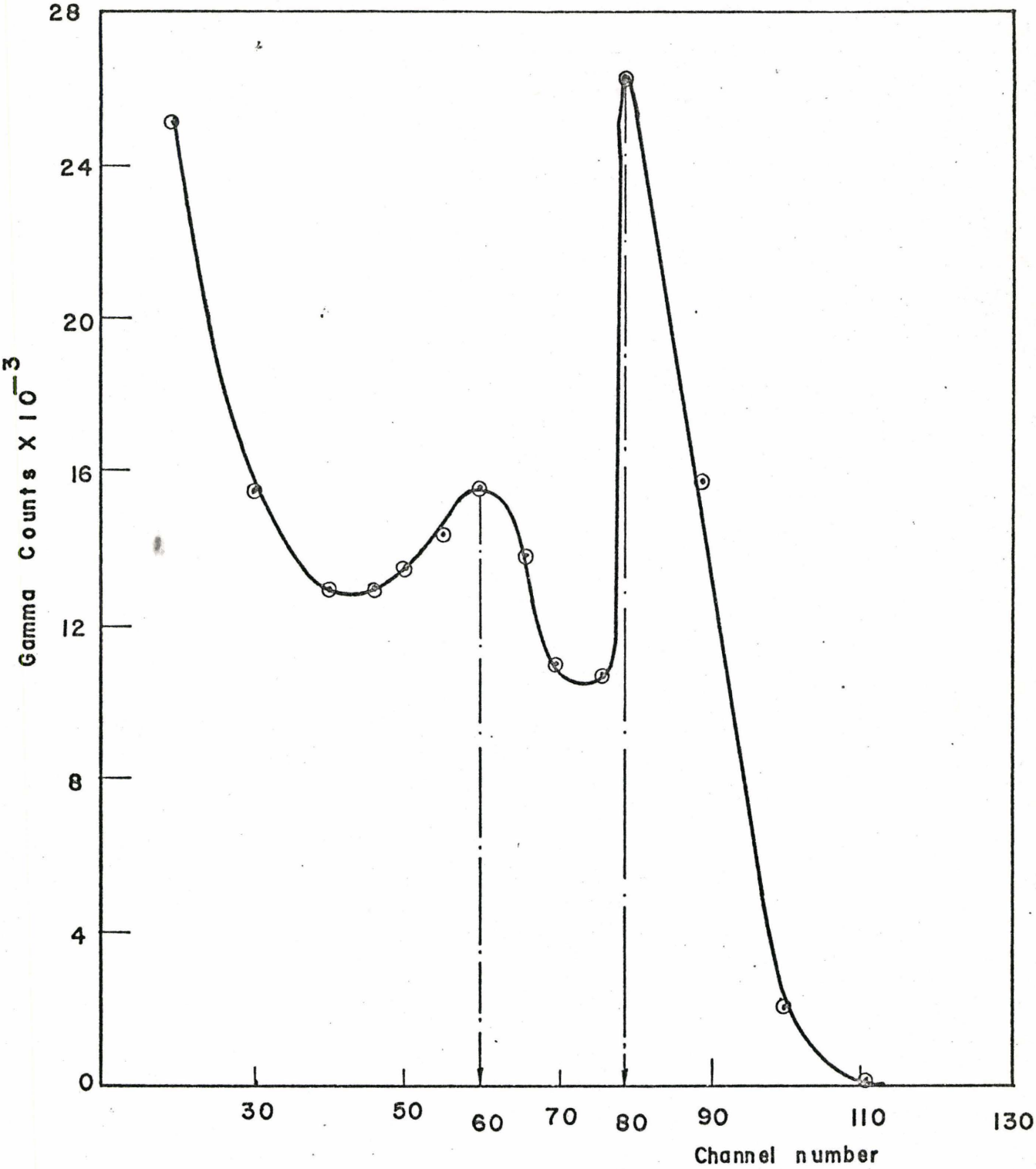

Fig.-(4-1)

^{60}Co SOURCE GAMMA SPECTRUM

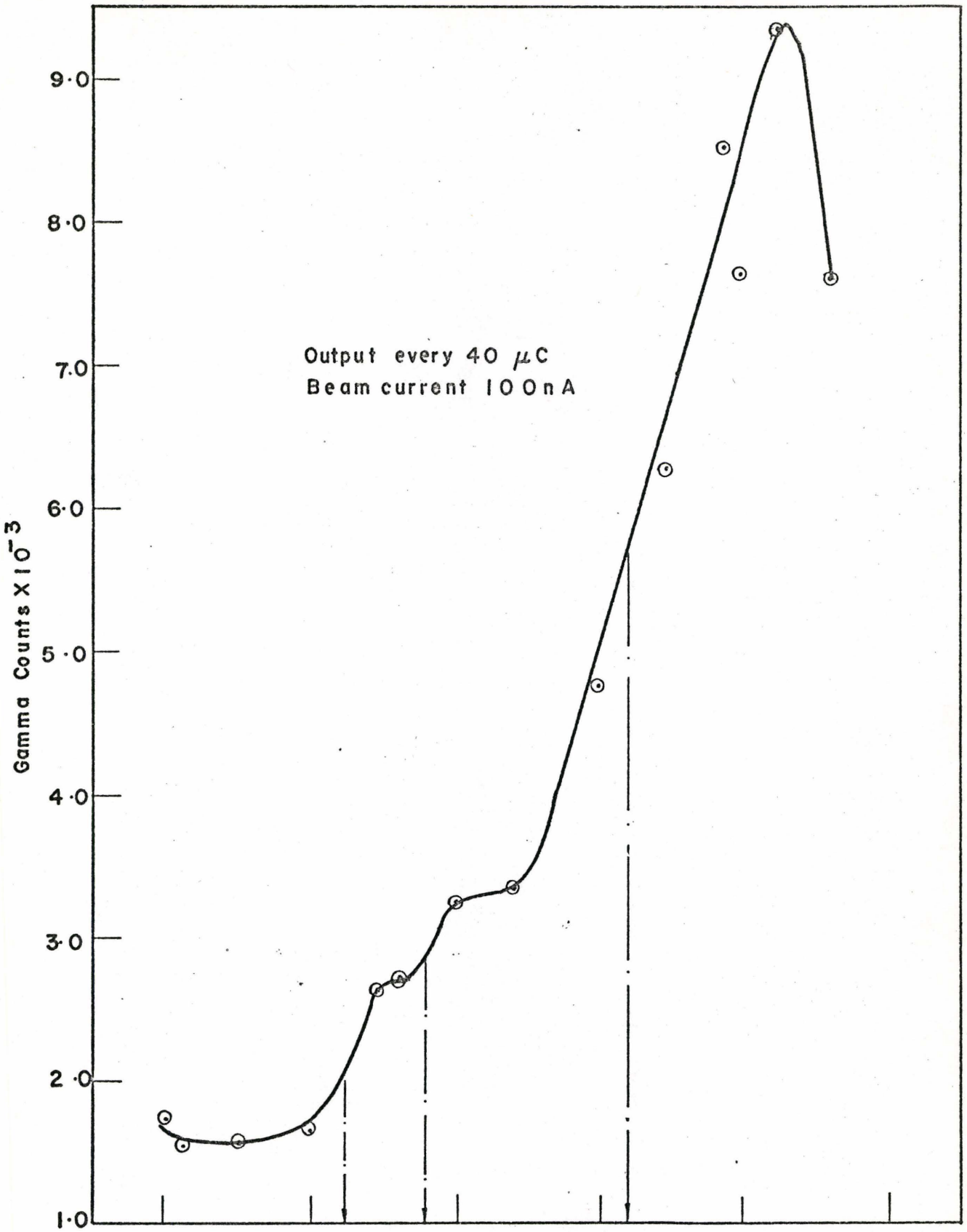

Fig. (4-2)

VAN DE GRAAFF ENERGY CALIBRATION

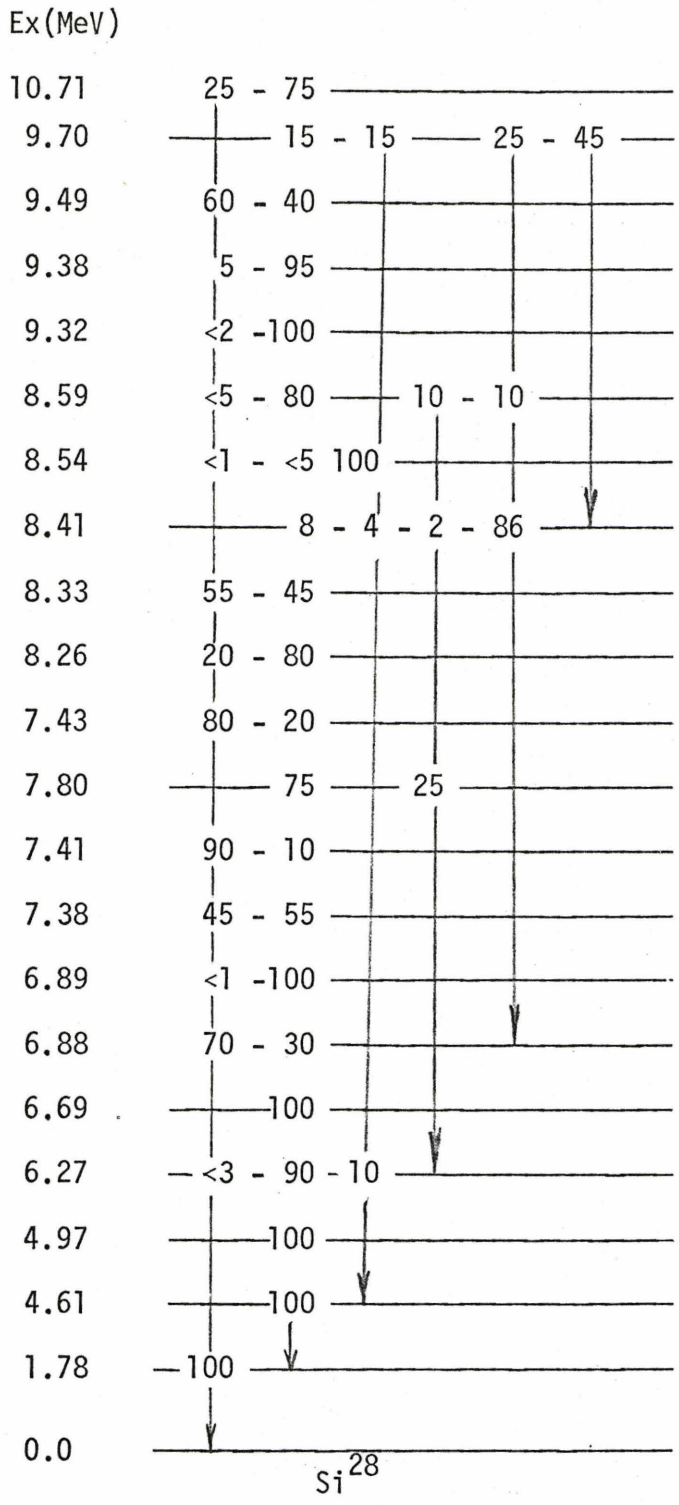

Fig. (4.3) Gamma decay of nonresonance levels of ^{28}Si numbers represent percentage branching (Reference [16]).

4.2.2 $_4Be^9(p,n)_5B^9$ Threshold Reaction

Here a $_4Be^9$ target was used, a detector angle of 90°, and a 400 nA current to give sufficient statistics. The experiment was carried out twice and the two sets of data were used to give correct threshold value. The threshold value of this reaction is known to be at 2.059 MeV [16].

Figure (4.4) shows the results of this experiment. The threshold value was found to take place at a digital voltmeter setting of 2.325 MeV. The measured magnetic field density using a Hall probe equals 3.98 KG. The magnet current was recorded to be equaling 3.2 amps. Now after necessary corrections for the magnetic field we can see that the reading of 3.98 KG corresponds to a reading of 3.833 KG on the new Gaussmeter.

We can now arrange the different results in a form of a table to draw the energy calibration curve which is the relation between the actual energy of the ion beam and the magnetic field intensity.

B	B^2	E_{actual}	E_{DVM}	$\frac{E_{act.}}{E_{DVM}}$
0.00	0.0000	0.000	0.000	1.000
2.65	7.0025	0.991	0.925	1.072
2.76	7.6176	1.118	1.025	1.089
3.04	9.2416	1.386	1.250	1.108
3.833	14.6689	2.058	2.325	0.875

These results are shown schematically in Fig. (4.5), a least squares straight line was computed. Let $y = \frac{B^2}{(\frac{m}{m_p})}$, mass = mass of the ion and m_p = mass of proton. Let X represent the energy. Then a linear relation of the form $y = C + \alpha x$ could be supposed.

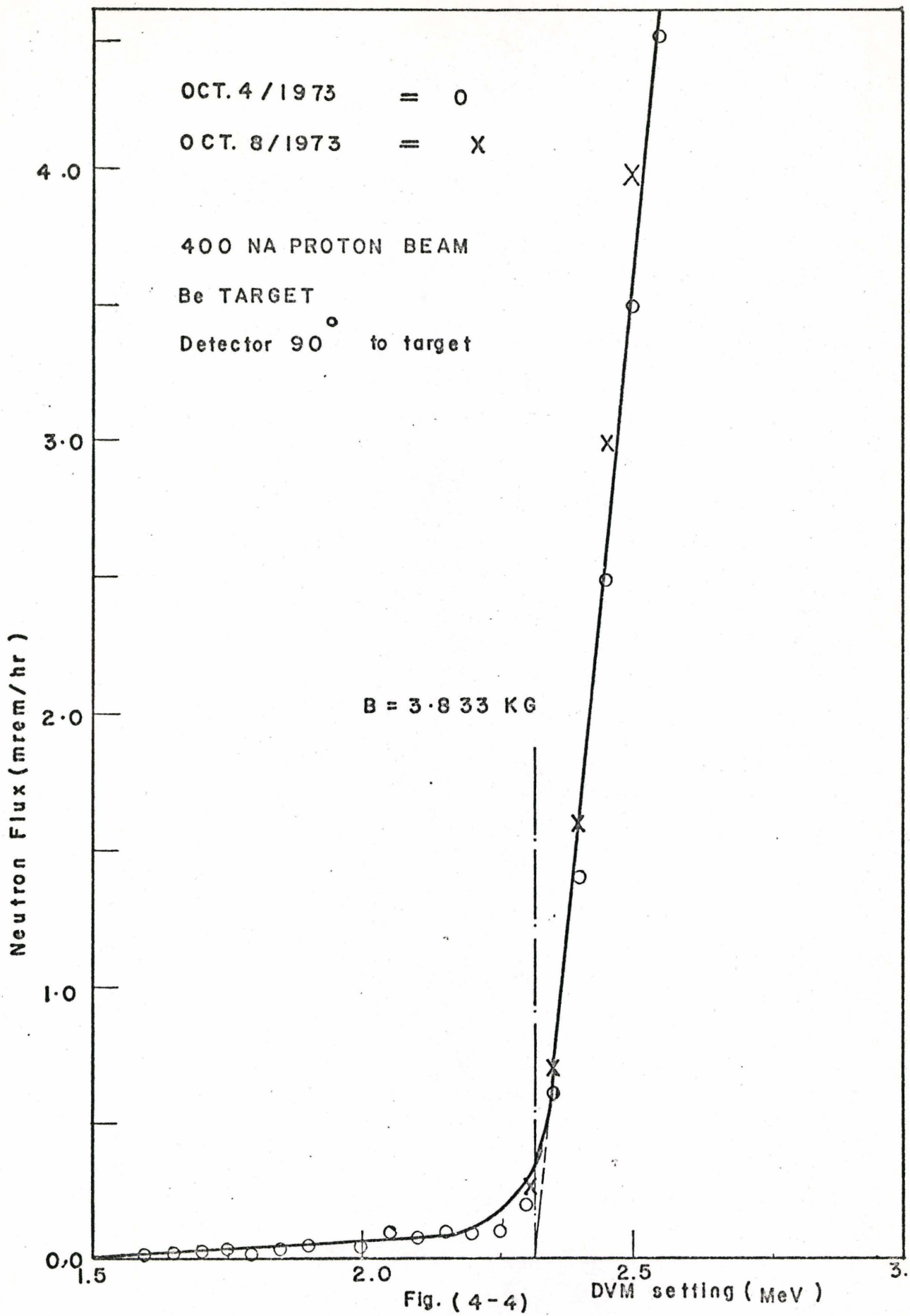
OCT. 4 / 1973 = O
OCT. 8 / 1973 = X
400 NA PROTON BEAM
Be TARGET
Detector 90° to target
B = 3·833 KG
Neutron Flux (mrem/hr)
4.0
3·0
2·0
1·0
0,0
1.5
2.0
2.5
3.0
DVM setting (MeV)

Fig. (4 - 4)

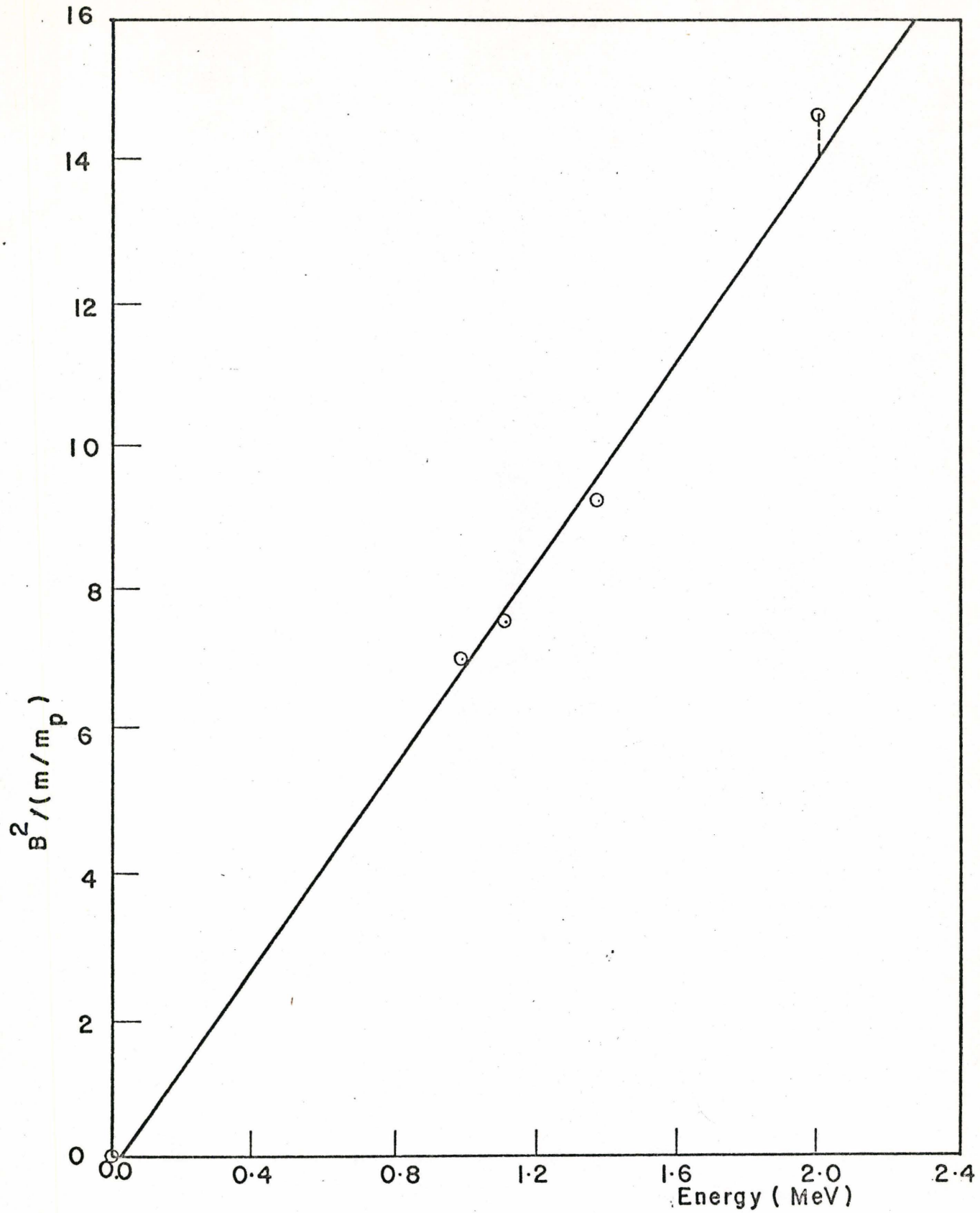

Fig. (4-5)

ENERGY CALIBRATION OF THE McMASTER VAN DE-GRAAFF ACCELERATOR

As a test of experiment, the constant C should be small and the largest error should not be too great so that one can say that linearity supposition is a good fit.

Results of computations show that C = - 0.1172 (KG^2) α = 7.046 (KG^2/MeV). The maximum error was found to be 3.92% at the energy of 2.058 MeV.

4.3 Sources of Error

1. The $Al^{27}(p,\gamma)$ Si^{28} experiment was repeated twice because we were not successful in detecting any of the gamma peaks the first time. The main reason is the sensitivity of the experiment to the discrimination level. As can be seen from Fig. (4.3), the decay scheme is complicated and one has to be careful in setting his discriminator level to a value slightly less than 1.78 MeV to reduce background.

2. Great care should be taken into consideration each time one makes measurements on the Gaussmeter because it works with a Hall probe. This probe should be placed as close as possible to the magnetic field and should be moved to all possible positions in space and the maximum attainable reading is the acceptable value of the magnetic field. Considerable errors might take place if the Gaussmeter is not zeroed at the beginning of each set of readings and the foregoing procedure is followed.

4. The "peak-to-total" ratio which represents the fraction of the total counts, in a gamma ray pulse hight spectrum, which occurs in the main peak corresponding to the full energy of the incident gamma, is though to be low in our case. Several means are available for improving the peak-to-total ratio. These include (a) use of quite a large NaI(Tl) crystal perhaps

9" in diameter x 10" high, (b) surrounding a medium-size NaI(Tl) crystal by an anticoincidence tank which responds to gammas escaping from the NaI(Tl), and (c) use of a multiple crystal compton or pair spectrometer. The use of large NaI(Tl) crystal is probably the most direct method for increasing the peak to total ratio [18].

A schematic diagram is shown in Fig. (4.6), which represents the experimental setup used for the gamma ray detection and counting.

4.4. Models of Instruments Used

(i) Van de Graaff KN 3 MeV High Voltage Engineering

(ii) Bell Model 620 Gaussmeter

(iii) ORTEC Model 462 Specroscopic Amplifier

(iv) CANBERRA Model 1436 PHA

(v) ORTEC Model 439 Current Digitizer

(vi) HARSHAW NaI(Tl) Scintillator, Scintillation Type 12S12-X

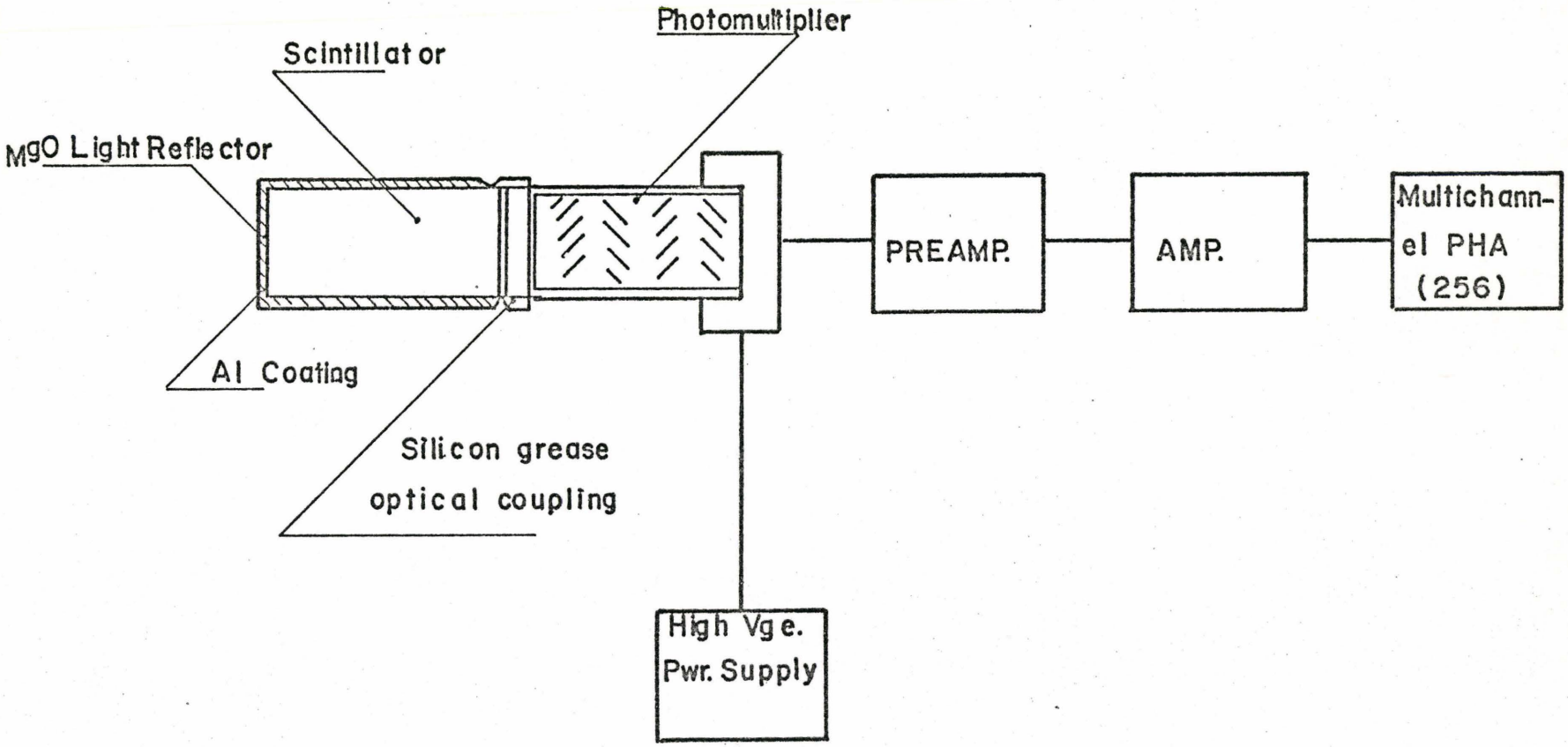

FIG. (4-6)

SCHEMATIC DIAGRAM OF DETECTION AND COUNTING SYSTEM

Chapter 5

THICK TARGET TECHNIQUE FOR MEASUREMENT OF STOPPING CROSS-SECTION

5.1 Thick Target Technique

Nuclear backscattering has become a widespread tool for solid state analysis. Use of thick targets in backscattering experiments is much simpler than thin targets because of the problems encountered in the preparation and density uncertainies in thin targets.

If E_o is the energy of the incident ion, then the energy E_1 of the ion after being elastically scattered from the target surface is given by

$$E_1 = K^2 E_o \tag{5.1}$$

where

$$K = \frac{M_1 \cos\theta_s}{M_1 + M_2} + \left[\left(\frac{M_1 \cos\theta_s}{M_1 + M_2}\right)^2 + \left(\frac{M_2 - M_1}{M_1 + M_2}\right)\right]^{\frac{1}{2}} \tag{5.2}$$

M_1 is the mass of the incident particle, M_2 is the mass of the surface-scattering atom, and θ_s (= 140°) is the laboratory scattering angle.

A schematic representation of nuclear backscattering from an elemental film is shown in Fig. (5.1) along with the resultant energy spectrum of backscattered ^{4}He particles. The incident ^{4}He beam has an energy, E_o, and the backscattered ions have an energy $E_f(1)$ if they scatter from the surface, and an energy $E_f(2)$ if they scatter from a depth ΔX from the surface. The yield spectrum shown displays how these energies are related, and defines the maximum backscattered energy difference, ΔE.

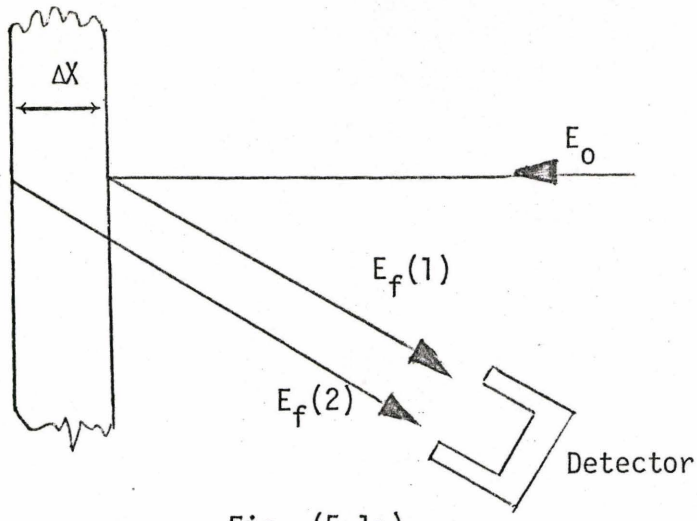

Fig. (5.1a)

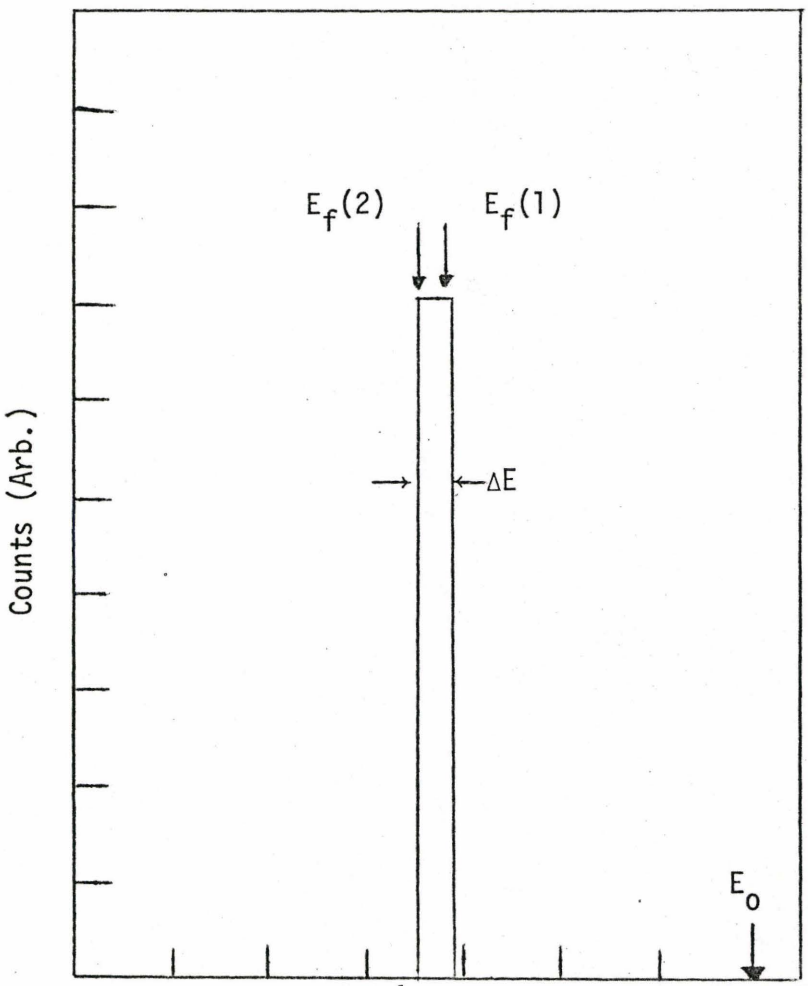

Fig. (5.1b)

From equation (5.2) and the schematic diagrams of Fig. (5.1), one can easily derive the following relationships:

$$\Delta E = E_f(1) - E_f(2)$$

$$= K^2 E_o - [K^2(E_o - NX\,\varepsilon_\alpha(in) - |\sec\theta| NX\,\varepsilon_\alpha(out)]$$

or

$$\Delta E = NX[K^2\,\varepsilon_\alpha(in) + |\sec\theta|\,\varepsilon_\alpha(out)] \qquad (5.3)$$

where N = number of atoms of target/c.c.

X = penetration distance in cm.

Let areal density

$$\equiv \rho_A = NX \text{ atoms/cm}^2$$

then

$$\rho_A = \Delta E[K^2\,\varepsilon_\alpha(in) + |\sec\theta|\,\varepsilon_\alpha(out)]^{-1}$$

$$= \Delta E\, B(\rho_A)$$

where $B(\rho_A)$ is defined as the areal density backscattering factor.

The target yield is simply proportional to the nuclear scattering cross-section, σ, the number of impinging ^{4}He ions, Q, the detector solid angle, Ω, and the areal density ρ_A. This relationship could be put in the form:

$$\text{Counts} = \sigma\, Q\, \Omega\, \delta\, E\, B(\rho_A) \qquad (5.5)$$

where $B(\rho_A)$ is defined as:

$$B(\rho_A) = E_o/[E_f\,\varepsilon_\alpha(E_o) - \sec\theta\, E_o\,\varepsilon_\alpha(E_f)] \qquad (5.6)$$

In the experiment carried out here, the scattering angle is 140° and the detector solid angle of 0.00317 s.rad.

5.2 Backscattered Spectrum

When an energetic beam of light atomic particles impinges on a solid, a fraction of the projectiles are scattered back from the solid. This phenomenon is commonly known as Rutherford backscattering.

The actual penetration of the energetic beam of particles depends on the energy of the projectile and the stopping power of the target for high-speed projectiles. The energy of the backscattered projectile can then be accurately related to the depth in the target of its scattering site and hence to the stopping power of the material.

Recent nuclear microanalysis has been carried out on many heavy metal films and compounds by means of the nuclear backscattering of He^4 ions. To obtain the composition and impurity content of thin, inter-metallic films, it is necessary to know the energy loss of the probing He^4 ions in the films.

A modification of the technique originated by Wenzel and Whaling [1], [2], [12] is used. A presentation of a detailed analysis of ^4He backscattering from a thick target of Si will be given to illustrate the analytic technique.

Thick targets of Si, SiC, C and V together with a thin film of silicon sandwiching a very thin layer of Ta were placed on a rotating disc covered with an evaporated layer of Au. The design of the rotating disc permitted same-conditions measurements for the five different targets together with backscattering measurements from the thin gold layer.

Reproducibility of the channel number corresponding to the surface backscattered energy was verified by measurements on the thick Si target and the thin Si film. An evaluation of the surface channel number was made using this technique within 0.5%.

For the spectra of the different thick targets at different He^4 ion energies, through the high energy plateau, a least squares fit of an analytic function was done of the form [19],[12]:

$$\text{Counts} = A(1) + A(2)/C + A(3)/C^2 \qquad (5.1)$$

Where A(1), A(2), A(3) are fitted constants and C is the channel number. The choice of the suitable portion of the curve for fitting is not done intuitively. The high channel number of the curve is not included in the fit to eliminate isotopic effects, surface roughness and possible alignments in the surface grains.

Each time a spectrum was collected for Si and SiC, the tilt angle was varied to check that the resulting spectrum is a random spectrum.

A typical spectrum is shown in Fig. (5.2) together with the fitted curve. An error diagram for every spectrum is made in the first run on the digital computer from which one can define the best portion of the spectrum for fitting, then a second run of the computer program (Appendix [E]) is made to produce the fitting curves of the different targets.

The fitting curve is extended out over the rounded edge. A straight line is drawn through the leading edge. Another auxiliary straight line is drawn by doubling the slope of the leading edge line. The intersection of the auxiliary straight line with the extention of the fitting curve gives two important parameters; the surface yield and the surface energy

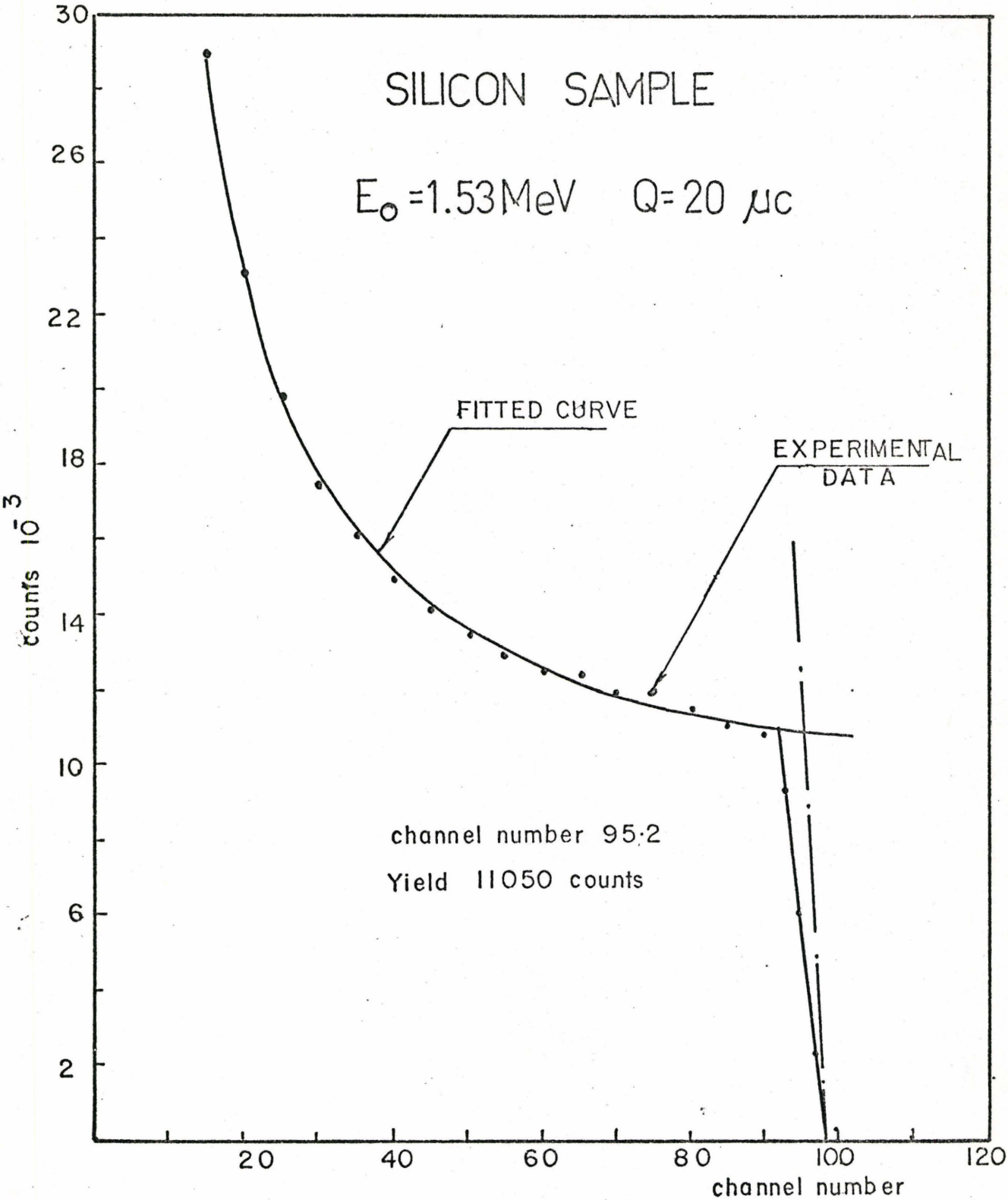
SILICON SAMPLE
E_o = 1.53 MeV Q = 20 μc
FITTED CURVE
EXPERIMENTAL DATA
channel number 95·2
Yield 11050 counts
counts 10^{-3}
channel number
30
26
22
18
14
10
6
2
20
40
60
80
100
120

Fig. (5.2)

channel number. The steps described above are shown in Fig. (5.3) through to Fig. (5.6).

For the gold layer, instead of fitting the high energy plateau with the function described, a tangent was drawn to that part of the curve. To increase the accuracy of this method, the number of back-scattered counts is increased such that the auxiliary line is nearly vertical and the inaccuracies in the intersection of the tangent and the auxiliary line is reduced. All figures drawn are for a calibrated energy of the ^{9}He ions of 2.22 MeV.

Figure (5.7) indicates the method used for the thin Au layer deposited on the Al disc.

5.3 Linearity of the Detection System

To find the channel width for the 256 multichannel pulse height analyser (δ E in KeV/channel) it is assumed that the pulse hight analyser is linear. A relationship is assumed of the form:

$$C = C_o + \alpha E$$

where

C = channel number

E = energy of the backscattered ^{4}He ion.

C_o and α = constants for the linear relationship

Actually δ E is the inverse of the slope of the assumed straight line.

For each particular value of the incident ^{4}He ion energy, a set of graphs are drawn just like those shown for the energy of 2.22 MeV.

CARBON Q = 30 μc

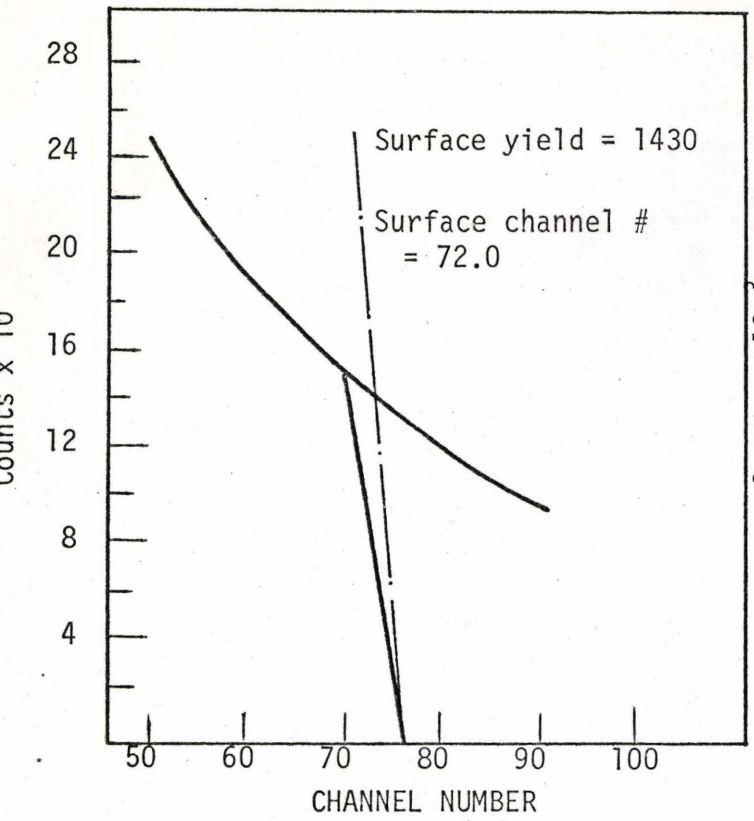

Fig. (5.3)

SILICON Q = 20 μc

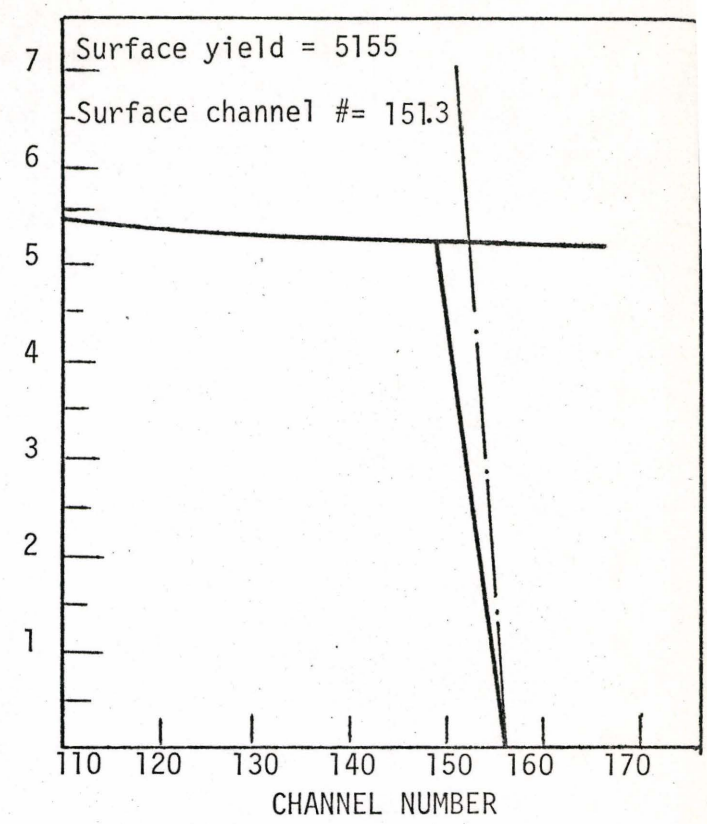

Fig. (5.4)

VANADIUM Q = 20 μc

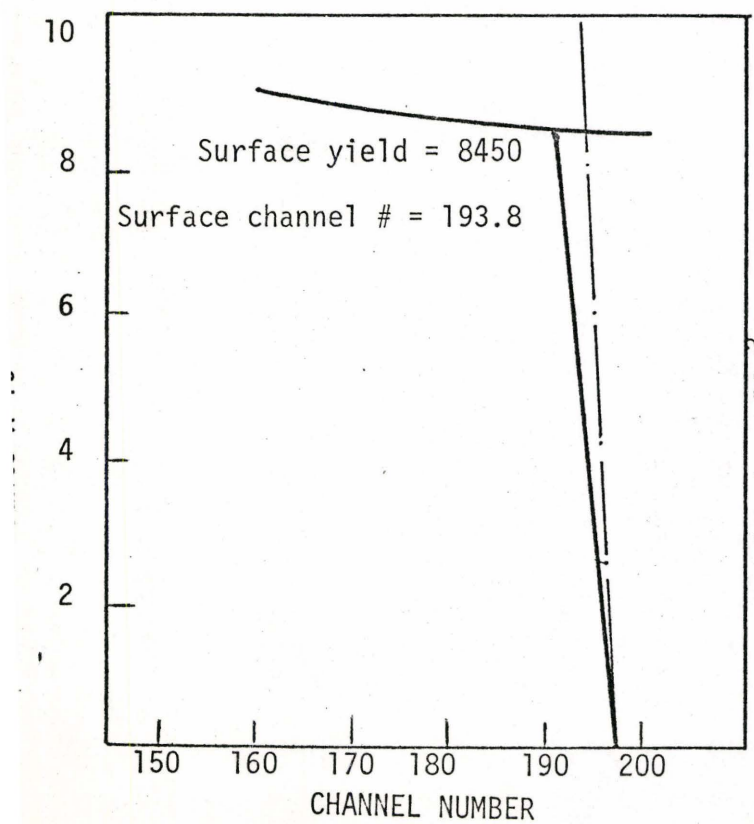

Fig. (5.5)

(SI + TA + SI) Q = 20 μc

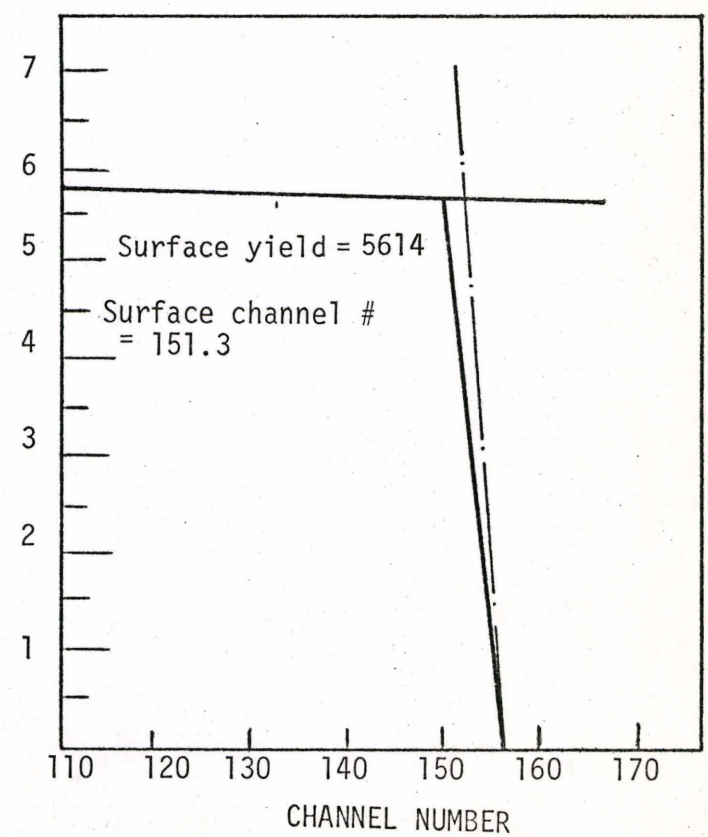

Fig. (5.6)

FIG(5-7)

Gold layer on Al backing, Q = 2·0 μC

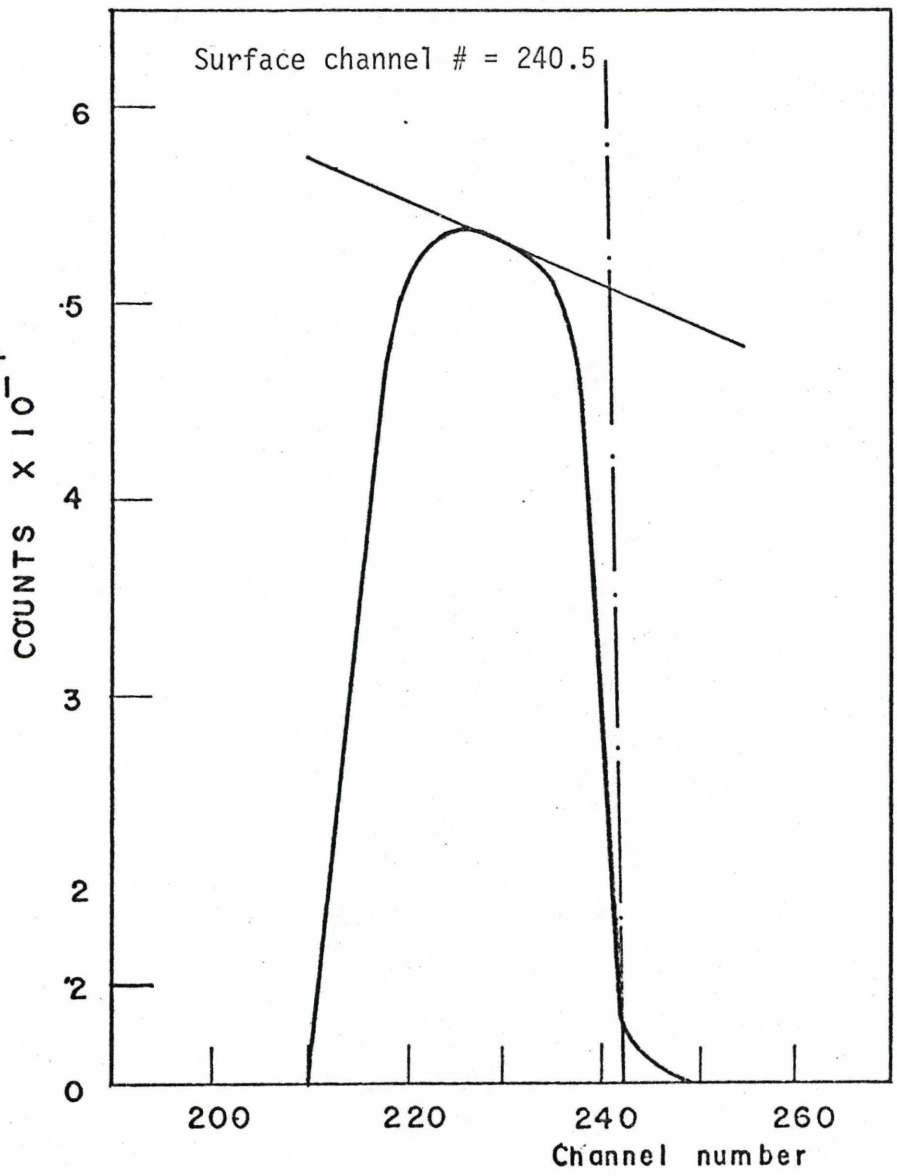

A summary of the results is as follows:

E_o = 2.22 MeV

Element	C	Si	V	Au
Surface Channel Number	72	151.3	193.8	240.5
Backscattered Energy (MeV)	0.639	1.332	1.678	2.058

E_o = 2.01 MeV

Element	C	Si	V	Au
Surface Channel Number	60.6	128.4	163.7	204.0
Backscattered Energy (MeV)	0.579	1.208	1.518	1.862

E_o = 1.65 MeV

Element	C	Si	V	Au
Surface Channel Number	50.8	107.2	136.95	170.5
Backscattered Energy (MeV)	0.476	0.990	1.248	1.53

E_o = 1.53 MeV

Element	C	Si	V	Au
Surface Channel Number	45.9	95.2	120.6	151.3
Backscattered Energy (MeV)	0.431	0.918	1.155	1.418

E_o = 1.25 MeV

Element	C	Si	V	Au
Surface Channel Number	37.46	78.23	100.2	124.5
Backscattered energy (MeV)	0.36	0.75	0.994	1.158

E_o = 1.02 MeV

Element	C	Si	V	Au
Surface Channel Number	30.75	60.2	75.9	92.6
Backscattered energy (MeV)	0.294	0.612	0.772	0.946

A least squares linear relationship is applied for each value of the impinging ^{4}He ion energy and the following results are obtained:

E_o(MeV)	C_o	α
2.22	-5.26	119.5
2.01	-4.90	111.5
1.65	-3.881	113.3
1.53	-0.6469	104.6
1.25	-2.391	109.0
1.02	+2.607	94.90

The spectroscopic simplifier gain is constant throughout the whole set of experiments at a value of 50. Typical beam currents varied from 5 nA to 50 nA. The losses in the detection system are typically from 0% to 5%.

CHAPTER 6

RESULTS AND DISCUSSIONS

6.1 Data Analysis and Results

6.1.1 Stopping Cross-sections of C, Si and V.

From the previous chapter, equations (5.5) and (5.6), one can proceed through the calculation of the stopping cross-section. The value of δE, the energy per channel, could be determined as the inverse of the linear relationship between the channel number and energy of recoil particle. The nuclear scattering cross-section per solid angle is calculated using Rutherford's law [20]:

$$\frac{d\sigma}{d\Omega} = \left(\frac{Z_1 Z_2 e^2}{4 E_1}\right)^2 (1 + \gamma) \cdot \frac{1}{\sin^4(\theta/2)} \text{ cm}^2/\text{sr} \qquad (6.1)$$

where

σ = nuclear scattering cross-section

Ω = solid angle in C.M. system

Z_1, E_1 = atomic number and energy of projectile respectively

Z_2 = atomic number of target nucleus

γ = M_1/M_2, mass ratio of projectile to target nuclei

θ = scattering angle in C.M. system

Equation (6.1) can be transposed to the lab coordinates, and the following expression for the differential cross-section in the lab coordinates is obtained,

$$d\sigma = 1.2926 \times 10^{-27} \left(\frac{Z_1 Z_2}{E_1}\right)^2 (1 + \gamma) \frac{1}{\sin^4(\psi/2)} \left[\frac{(1 + \gamma^2 + 2\gamma \cos\Psi)}{1 + \gamma \cos\psi}\right]^{\frac{3}{2}}$$

$$d\omega \ cm^2/sr \qquad (6.2)$$

where

ψ = scattering angle in lab system

E_1 = projectile energy in MeV

ω = solid angle in lab system

From equations (5.5) and (5.6), chapter 5, we have the following relationship for the calculation of the stopping cross-section using thick target technique:

$$\varepsilon_\alpha = \frac{\sigma \ Q \ \Omega \ E_o \quad \delta E/counts}{E_f - \sec\theta \ E_o [\varepsilon_{Theo}(E_f)/\varepsilon_{Theo}(E_o)]} \ ev/(10^{15} \ atoms/cm^2) \qquad (6.3)$$

Instead of using theoretical calculations to obtain the ratio $[\varepsilon_{Theo}(E_f)/\varepsilon_{Theo}/E_o)]$ in equation (6.3) [12], a semiempirical approach has been followed as described in chapter 3.

The following equations, which are consistent with discussions and conclusions of chapter 3, have been used:

(i) Carbon, p = 100, shell correction factor = 1.35

$$\frac{dE}{dx} = 1885.7554 \ E - 509.7386 \ E^2 + 3914.7927/E - 1115.1262/E^2 \qquad (6.4)$$

(ii) Silicon, p = 100, shell correction factor = 1.2

$$\frac{dE}{dx} = 1451.4769 \ E - 352.6531 \ E^2 + 2230.473-/E - 532.2215/E^2 \qquad (6.5)$$

$\frac{dE}{dx}$ is (MeV/cm)

FIG. (6 – 1)

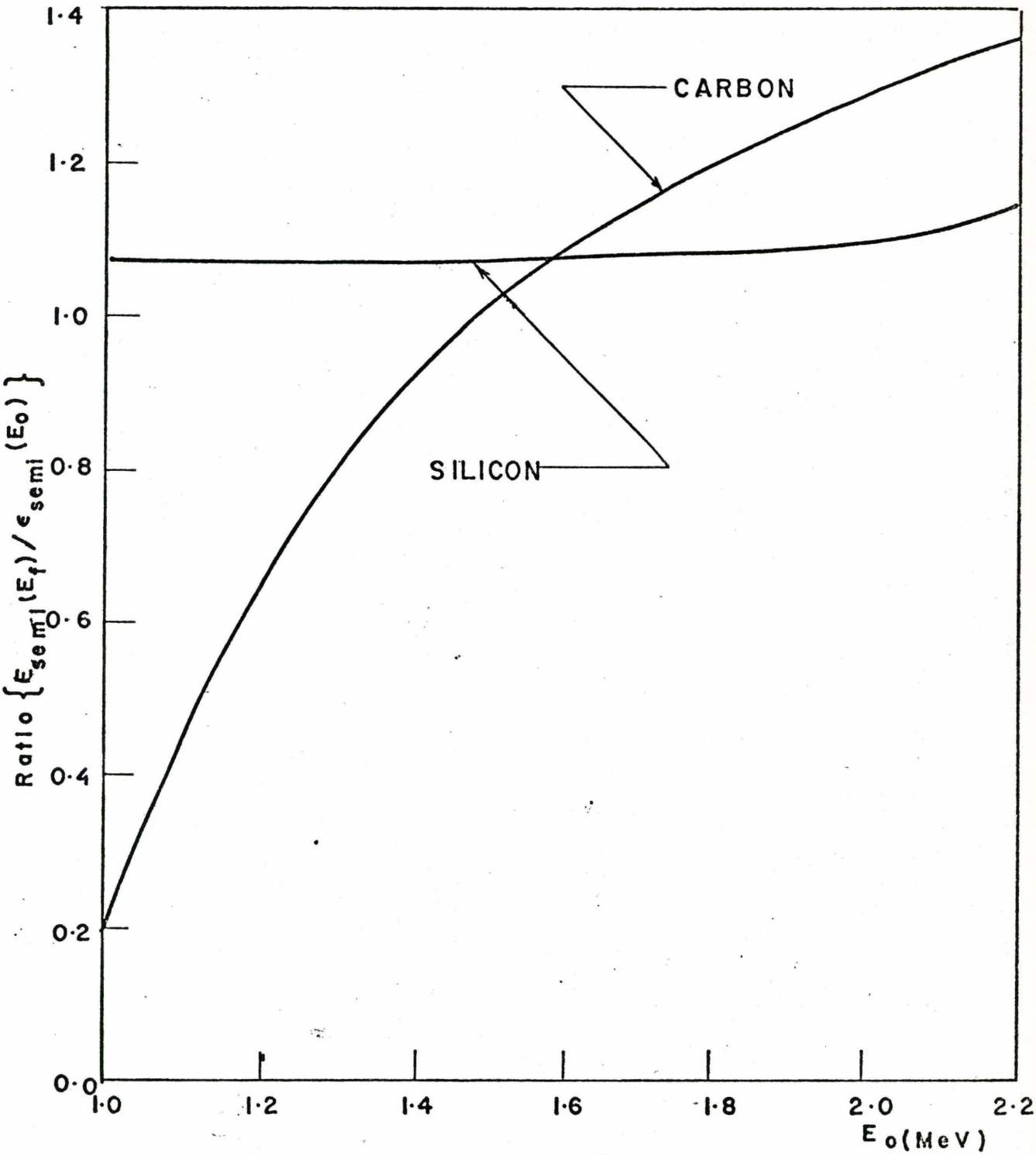
1·4
1·2
1·0
0·8
0·6
0·4
0·2
0·0
CARBON
SILICON
Ratio $\{E_{semi}(E_f)/\epsilon_{semi}(E_0)\}$
1·0
1·2
1·4
1·6
1·8
2·0
2·2
E_0(MeV)

Figure (6.1) shows $[\varepsilon_{semi}(E_f)/\varepsilon_{semi}(E_o)]$ for He^4 ions impinging on C and Si targets. From this figure, one can notice the very slight variation with impinging He^4 ion energy in case of Si targets and the large rate of increase for C targets. This might be reflected in the larger expected error of this ratio due to an error in the He^4 ion energy for low energies and the consequent poor reliability on theoretical data [12] for low z targets.

The phenomenon of secondary electron emission is of importance in the determination of the actual ion beam charge. The number of secondary electrons emitted per positive ion is denoted by γ_i.

Variation of the supression potential on the target was observed to have considerable effect on the amount of charge collected. Levelling off of the bias potential effect on collected charge occurred in the voltage range of 480 volts to 780 volts. To verify a value of $\gamma_i \simeq 0.7$ an independent experimental measurement of Vanaduim stopping cross section for He^4 ions was made with the same geometry and supression potential of 600 volts.

Recent experimental data from J.F. Ziegler and W.K.Chu [3] was used to compare results obtained for V.

A correction factor of 1.7 is used to find out the actual charge collected by dividing the collected charge by this factor. Vanaduim stopping cross sections obtained this way are in experimental agreement with recent measurements as shown in Table (6.1).

Table (6.1) Stopping Cross-sections for He in V

Energy(MeV)	Present Experimental ε_α in [ev/(10^{15} atoms/cm^2)]	Extrapolated Experimental ε_α from [3] in [ev/(10^{15} atoms/cm^2)]
1.02	84.251	88.0
1.25	80.537	84.5
1.53	76.00	79.5
1.65	72.00	78.0
2.01	78.265	71.0
2.22	77.371	68.5

Using the same factor of 1.7 to correct for the effect of secondary electrons emitted on the collected charge, calculations of the stopping cross-sections are made for Si and C and the results are shown in Tables (6.2), and (6.3).

The experiments were made with a detector solid angle, Ω, of 3.17 msr, a scattering angle, θ, of 140°.

Define the following parameters:

σ = nuclear scattering cross-section cm^2

$n = Q/q$ = number of particles collected

α = slope of linear relationship as defined in chapter 5.

$\delta E = 1/\alpha$ MeV/channel

Y = surface yield obtained by methods of chapter 5

$R = [\varepsilon_{semi}(E_f)/\varepsilon_{semi}(E_o)]$

Then Table (6.2) is obtained as follows:

Table (6.2) Stopping Cross-sections of C for He^4 Ions

E_o (MeV)	E_f (Mev)	σ	n	α	Y	R	ε_α in this report	ε_α in + ref.[3]
1.02	0.294	1.911×10^{-25}	1.25×10^{14}	94.9	8650	0.900*	41.2882	36.0
1.25	0.360	1.273×10^{-25}	2.5×10^{14}	109.0	9250	1.000*	41.2175	33.8
1.53	0.441	8.5×10^{-26}	2.5×10^{14}	104.6	6650	1.026	39.0746	30.7
1.65	0.476	7.3×10^{-26}	2.5×10^{14}	113.3	5160	1.107	37.5432	29.25
2.01	0.579	4.92×10^{-25}	1.875×10^{14}	111.5	2538	1.28	34.790	25.9
2.22	0.612	4.035×10^{-26}	1.25×10^{14}	119.5	1430	1.368	30.0	24.0

*obtained from measurements in ref. [3] to increase reliability in low energy range as in fig. (6.1) + extrapolated values to correspond to present energies.

Table (6.3) Stopping Cross-sections of Si for He^4 Ions

E_o (MeV)	E_f (MeV)	σ	n	α	Y	R	ε_α in this report	ε_α in + ref.[3]
1.02	0.612	1.15×10^{-24}	1.25×10^{14}	94.9	17550	1.068	88.55/44*	66.0
1.25	0.750	7.6615×10^{-25}	1.25×10^{14}	109.0	14400	1.078	62.2126	61.5
1.53	0.918	5.113×10^{-25}	1.25×10^{14}	104.6	11050	1.079	56.3425	56.20
1.65	0.990	4.394×10^{-25}	1.25×10^{14}	113.3	8550	1.081	50.0851	54.25
2.01	1.206	2.963×10^{-25}	1.25×10^{14}	111.5	6640	1.101	50.2843	49.00
2.22	1.332	2.429×10^{-25}	1.25×10^{14}	119.5	5155	1.127	48.7630	48.00

* anomalously high value

+ extrapolated values to correspond to present energies

6.1.2 Stopping Cross-section of SiC

Calculation of the experimental stopping cross-section of SiC for He^4 ions has been made using random spectra of a SiC sample. A least squares curve is fitted to each distinct part of the spectrum with an analytic function of the form:

$$\text{Counts} = A(1) + A(2)/C + A(3)/C^2$$

The relevant points to be fitted in each part are chosen using the error diagram produced by the computer program in Appendix [E] but generally are in the intermediate range in each part. A representative sample result is shown in fig. (6.2). The fitted spectrum is extended both directions as shown. At channels that correspond to the surface energy for C and Si, calculated from preceding chapters, a vertical line is drawn and intersections with fitted curves give surface yields of Si and C in SiC. Typical results, following this method, are:

Collected charge = 1.25×10^{14} He^4 ions

Calibrated energy of He^4 ions = 1.53 MeV

Difference in counts of the two fitted curves due to C at channel #45.9 = 11098 - 10162 = 936 counts. Si surface yield in SiC = 7690 counts

The same geometrical factors are used in obtaining SiC spectrum as those for Si and C targets at the same initial He^4 ion energy, E_o. Calculations of C and Si stopping cross-sections for He^4 ions are now straight forward using a density of 3.217 gm/c.c. for SiC [17]. SiC is known to be stoichiometric according to Lely [23] for crystals grown at 2500-2600°C; if there is a deviation of stoichiometry at all, it should be less than 10^{-5} atomic per cent [24]. In a cubic centimeter of SiC, the Si to C atoms, an atoms ratio

FIG. (6 - 2)

ANALYSIS OF SiC SAMPLE

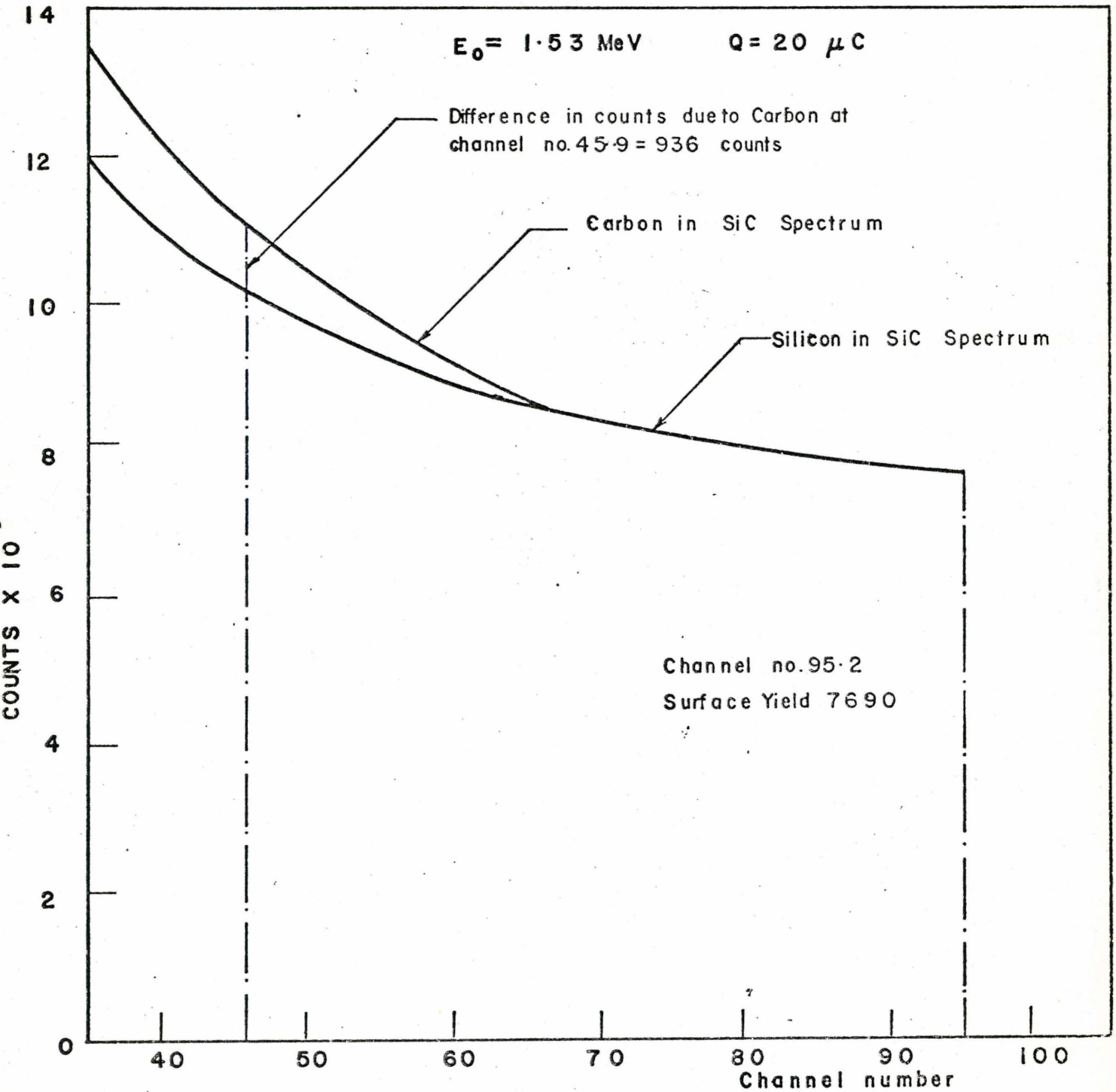

of 1:1 exists.

Then,

$$\frac{m_c \, No}{12.01115} = \frac{m_s \, No}{28.068}$$

where

No = Avogadro's number

m_c, m_s = masses of C and Si in a cubic cm of SiC respectively

Let ρ_{sic} = density of SiC, then

$$m_c = 0.300 \, \rho_{sic}$$

$$m_s = 0.700 \, \rho_{sic}$$

A calculation of the ratio of the number of C atoms in SiC to the number of C atoms in pure C per cm^3 could now be calculated and this is also equal to the ratio of areal densities of C. Let this ratio be R, then

$$R_c = \frac{0.3 \times \rho_{sic} \times No/12.0011}{\rho_c \times No/12.0011}$$

$$= 0.3 \times 3.217/2.22 = 0.434$$

while for Si, this ratio is:

$$R_s = \frac{0.7 \times \rho_{sic} \times No/28.068}{\rho_{si} \times No/28.068}$$

$$= 0.965$$

From equation (6.3), in case of constancy of all parameters used in the calculation except the number of collected particles, the counts and the number of atoms per cm^2, we can write the relationship in the form:

$$\varepsilon_\alpha = K \frac{Q \, \rho_A}{counts} \quad [ev/(10^{15} \text{ atoms/cm}^2)] \qquad (6.6)$$

where K is a constant for the same energy of the particles and the same geometry.

Now if we let subscript 1 represent the case of pure silicon or carbon and subscript 2 represent the case of silicon or carbon in SiC, then:

$$\varepsilon_{\alpha_2} = \varepsilon_{\alpha_1} \left(\frac{Q_2}{Q_1}\right) \left(\frac{\text{counts}_1}{\text{counts}_2}\right) \left(\frac{\rho A_2}{\rho A_1}\right) \quad [\text{ev}/(10^{15} \text{ atoms/cm}^2)]$$

From this simple equation we can proceed to the calculation of the stopping cross-sections of Si and C in their compounded state.

Using the numbers given before, then, for Si:

$$\varepsilon_{\alpha_2}(1.53 \text{ MeV}) = 78.1 \ [\text{ev}/(10^{15} \text{ atoms/cm}^2)]$$

and for C

$$\varepsilon_{\alpha_1}(1.53 \text{ MeV}) = 60.03 \ [\text{ev}/(10^{15} \text{ atoms/cm}^2)]$$

Values of the stopping cross-section of SiC calculated this way are put in Table (6.4). The stopping cross-section of carbon in SiC is not calculated using this method for low energies (1.02 MeV) and for high energies (1.01 and 2.22 MeV) because of the rapid rate of decrease of the spectrum in the first case and of small difference in counts in the high energy range in the second case.

Table (6.4) Comparison of SiC Stopping Cross-sections

[ev/(10^{15} atoms/cm^2)]

E_o	ρ_{sic} using Bragg's Rule	ρ_{sic} Calculated Directly	% Error
1.25	103.4341	147.5	29.2
1.53	95.4371	138.13	30.8
1.65	87.6283	137.0	36.1

6.1.3 Validity of Bragg-Kleeman Additivity Rule

From the figures presented in Table (6.4), one could see the deviation of the stopping cross-section of SiC calculated directly from that calculated using Bragg-Kleeman additivity rule. Above 1.00 MeV, the calculated stopping cross-section lies below the measured values by more than can be expected from experimental error. Consequently when reliable values for stopping cross-sections are required, it is preferable to measure them directly in the material of interest and in the appropriate physical state, rather than to compute them from data available for the constituent atoms.

6.2 Discussions and Sources of Error

As indicated from fig. (6.1) the rapid increase in the ratio of $[\varepsilon_\alpha(E_f)/\varepsilon_\alpha(E_o)]$ for low energies and low z elements might introduce errors in the stopping cross section calculations. For this reason, the first two ratios in Table (6.2) were obtained from previous experimental measurements [3]. Slight variations might exist in the value of γ_i for different targets and independent experimental arrangement may verify its constancy for different

targets as stated by D.J. Rose and M. Clark [21].

Stopping cross-section calculations in this report of C for He^4 ions are higher than those given by J.F. Ziegler and W.K. Chu [3], however, other experimental sources, e.g. Ward Whaling [22], give even higher values for C. Impurity content, surface roughness, structural faults and other carbon crystal structure effects might account for the differences in stopping cross-sections of C for He^4 ions from reference to the other.

In the low energy range (< 1.25 MeV), the energy per channel should not be too large and this could be controlled by the gain of the spectroscopic amplifier, while in the high energy range (> 2.01 MeV) the number of collected ions should be increased to allow better statistics.

6.3 Conclusions:

As an extension of the work the technique followed to develop semi-empirical relations for light elements could be extended to the heavier elements by using other shapes factors of the inner shell corrections.

As a conclusion, the differences between the values of the stopping cross-sections of SiC calculated using Bragg-Kleeman additivity rule can not be attributed to experimental errors and hence one has to measure stopping cross-sections directly if critical values are needed.

APPENDIX [A]

```
      PROGRAM TST (INPUT,OUTPUT,TAPE5=INPUT,TAPE6=OUTPUT)
C          MAIN PROGRAM
      DIMENSION A(5),ASTRT(5),G(5),Y(5),PY(5),DUM1(5),DUM2(5),GRAD(5),
     1EPS(5),H(30),XX(3,100),NUMB(150),INUMB(150),X(150),X1(150),
     2ERROR(150),EHELP(150),AP(150),IPA(100),CK(20),ESM(100)
      COMMON/XXX/E,Z,RO,AV,A1,XME,ZZ,XMP,C,CK,XI,DEN,ENI,COR,NF,M,N
      READ (5,1)E,Z,RO,AV,A1,XME,ZZ,XMP,C,(CK(I),I=1,15),XI,DEN,ENI,COR
      WRITE(6,1)E,Z,RO,AV,A1,XME,ZZ,XMP,C,(CK(I),I=1,15),XI,DEN,ENI,COR
      READ(5,2)NF,M,N
      WRITE(6,2)NF,M,N
      WRITE(6,5)
      READ (5,109)(ESM(I),I=1,70)
      WRITE(6,110)(ESM(I),I=1,70)
      CALL FMLPO(A,ASTRT,G,Y,PY,DUM1,DUM2,EPS,H,GRAD,NUMB,XX,X,X1,ERROR,
     3EHELP,AP,INUMB,IPA)
      CALL EXIT
    1 FORMAT(8E10.4)
    2 FORMAT(16I5)
    5 FORMAT(1H1)
  109 FORMAT(10A8)
  110 FORMAT(7((30X,10A8)/))
      END
```

APPENDIX [B]

```
      SUBROUTINE FCTAPP(X,K,A,APP,GRAD,IINT,INDIC)
SUBROUTINE WHICH CALCULATES APPROXIMATING FUNCTION AND ITS GRADIENTS
 WITH RESPECT TO VARIABLE PARAMETERS
      DIMENSION A(1),GRAD(1)
      GO TO (100,200),INDIC
00    APP=A(1)*X+A(2)*X*X+A(3)/X+A(4)/(X*X)
      RETURN
00    GRAD(1)=X
      GRAD(2)=X*X
      GRAD(3)=1./X
      GRAD(4)=1./(X*X)
      RETURN
      END
```

APPENDIX [C]

```
      FUNCTION FUNCS(X,IINT)
 FUNCTION SUBPROGRAM WHICH DEFINES UPPER AND LOWER SPECIFIED FUNCTION
      DIMENSION CK(20),A(25),B(10),EN(25)
      COMMON/XXX/E,Z,RO,AV,A1,XME,ZZ,XMP,C,CK,XI,DEN,ENI,COR,NF,M,N
      GO TO (1001,1001,1002,1002,1003,1003,1004,1004,1005,1005,1006,
     A11006,1007,1007,1008,1008,1009,1009,1010,1010,1020,1020,1030,1030,
     B1040,1040,1050,1050,1060,1060,1070,1070,1080,1080,1090,1090,
     C1100,1100),IINT
1001  PI=3.1 159265
      YN=RO*AV/A1
      DO 15 I=1,NF
      IF(I-1)300,444,300
 444  EN(1)=ENI
      GO TO 15
 300  J=I-1
      EN(I)=EN(J)+DEN
  15  CONTINUE
      CALL  LESQ(A,B,EN,CK,M,N)
      RETA=X
      ALEX=B(1)+B(2)*RETA+B(3)*RETA*RETA+B(4)*RETA**3+B(5)*RETA**4
     1+B(6)*RETA**5
      V=SQRT((3.2E-6)*X/XMP)
      BETA=V/C
      FAX=ALEX*COR
      FAC1=ZZ*ALOG(2.*XME*V*V/(XI*(1.-BETA*BETA))-BETA*BETA)-FAX
      FAC2=YN*4.*PI*(E**4)*Z*Z/(XME*V*V)
      FUNCS=FAC1*FAC2/(1.6E-6)
      RETURN
1002  FUNCS=1.82*1840.
      RETURN
1003  FUNCS=1.82*1790.
      RETURN
1004  FUNCS=1.82*1740.
      RETURN
1005  FUNCS=1.82*1710.
      RETURN
 006  FUNCS=1.82*1660.
      RETURN
 007  FUNCS=1.82*1560.
      RETURN
 008  FUNCS=1.82*1470.
      RETURN
 009  FUNCS=1440.*1.82
      RETURN
 010  FUNCS=4000.
      RETURN
 020  FUNCS=4040.
      RETURN
 030  FUNCS=.0350E+05
      RETURN
 040  FUNCS=.0370E+05
      RETURN
 050  FUNCS=.0380E+05
      RETURN
  60  FUNCS=.0385E+05
      RETURN
```

...continued

```
70 FUNCS=.0360E+05
   RETURN
80 FUNCS=.0340E+05
   RETURN
90 FUNCS=.03000E+04
   RETURN
00 FUNCS=.0
   RETURN
   END
```

```
      PROGRAM TST (INPUT,OUTPUT,TAPE5=INPUT,TAPE6=OUTPUT)
      DIMENSION CK(20),A(25),B(10),EN(25),EN2(200),ALEX(200),EGYPT(200)
     1,FAX(200),ESM(100)
  106 READ (5,1)E,Z,RO,AV,A1,XME,ZZ,XMP,C,(CK(I),I=1,13),XI,DEN,ENI,ENI2
     1,DEN2,COR,DCOR
      WRITE(6,1)E,Z,RO,AV,A1,XME,ZZ,XMP,C,(CK(I),I=1,13),XI,DEN,ENI,ENI2
     1,DEN2,COR,DCOR
      READ(5,2)NF,M,N,NF2,IFF
      WRITE(6,2)NF,M,N,NF2,IFF
      WRITE(6,5)
      READ (5,109)(ESM(I),I=1,70)
      WRITE(6,110)(ESM(I),I=1,70)
      WRITE(6,3)
      PI=3.14159265
      YN=RO*AV/A1
      DO 111 II=1,IFF
      COR = COR+DCOR
      DO 15 I=1,NF
      IF(I-1)300,444,300
  444 EN(1)=ENI
      GO TO 17
  300 J=I-1
      EN(I)=EN(J)+DEN
   17 V=SQRT(2.*(1.6E-6)*EN(I)/XMP)
      BETA=V/C
      FAC1=ZZ*ALOG(2.*XME*V*V/(XI*(1.-BETA*BETA))-BETA*BETA)-CK(I)
      FAC2=YN*4.*PI*(E**4)*Z*Z/(XME*V*V)
      ELOSS=FAC1*FAC2/(1.6E-6)
      WRITE(6,4)EN(I),ELOSS
   15 CONTINUE
      WRITE(6,5)
      CALL  LESQ(A,B,EN,CK,M,N)
      DO 16 J=1,NF2
      IF(J-1)333,500,333
  500 EN2(1)=ENI2
      GO TO 18
  333 I=J-1
      EN2(J)=EN2(I)+DEN2
   18 V=SQRT((3.2E-6)*EN2(J)/XMP)
      BETA=V/C
      ALEX(J)=B(1)+B(2)*EN2(J)+B(3)*EN2(J)*EN2(J)+B(4)*EN2(J)**3
     1+B(5)*EN2(J)**4+B(6)*EN2(J)**5
      FAX(J)=ALEX(J)*COR
      FAC1=ZZ*ALOG(2.*XME*V*V/(XI*(1.-BETA*BETA))-BETA*BETA)-FAX(J)
      FAC2=YN*4.*PI*(E**4)*Z*Z/(XME*V*V)
      EGYPT(J)=FAC1*FAC2/(1.6E-6)
      WRITE(6,4)EN2(J),EGYPT(J)
      CALL PLOTPT(EN2(J),EGYPT(J),4)
   16 CONTINUE
      CALL OUTPLT
      DO 112 JJJ=1,NF
      EN2(JJJ)=EN2(JJJ)
      ALEX(JJJ)=ALEX(JJJ)
      FAX(JJJ)=FAX(JJJ)
      CALL PLOTPT(EN2(JJJ),FAX(JJJ),35)
      CALL PLOTPT(EN2(JJJ),ALEX(JJJ),46)
  112 CONTINUE
```

.....continued

```
      CALL OUTPLT
      WRITE(6,107)COR
  111 CONTINUE
      GO TO 106
    1 FORMAT(8E10.4)
    2 FORMAT(16I5)
    3 FORMAT(50X,6HENERGY,15X,7H(DE/DX),//,50X,5H(MEV),17X,6HMEV/CM,//)
    4 FORMAT(48X,E10.4,11X,E10.4,//)
    5 FORMAT(1H1)
  107 FORMAT(1H1,///,50X,18(2H**),/,50X,1H*,*L-SHELL CORRECTION FACTOR*
     1,3X,F6.3,1H*,/,50X,18(2H**),//)
  109 FORMAT(10A8)
  110 FORMAT(7((30X,10A8)/))
      END
```

APPENDIX [E]

```
NNNNNNNNNNNNNNNNNNNNNNNNNNNNNNNNNNNNNNNNNNNNNNNNNNNNNNNNNNNNNNNNNNNNNNNNN
```

Ap

```
      PROGRAM TST (INPUT,OUTPUT,TAPE5=INPUT,TAPE6=OUTPUT)
      DIMENSION A(15),B(10),Y(500),E(500),EE(500),X(500),IY(500),C(500)
     1,ESM(200)
  506 READ (5,501)II,N,M,IFF,NN
      READ (5,503)DXN,XNI,XINT,OXIT
      READ (5,508)(ESM(I),I=1,80)
      WRITE (6,602)II
      WRITE(6,508)(ESM(I),I=1,80)
      READ (5,502)(IY(I),I=1,N)
      X(1)=XINT
      DO 888 I=1,N
      IF(I-1)30,30,40
   40 X(I)=X(I-1)+DXIT
   30 Y(I)=IY(I)
      CALL PLOTPT(X(I),Y(I),35)
  888 CONTINUE
      CALL OUTPLT
      DO 333 I=1,N
  333 E(I)=1./X(I)
      CALL LESQ(A,B,E,Y,M,N)
      MP=M+1
      WRITE (6,1001)(B(I),I=1,MP)
      SUM=.0
      DO 777 I=1,N
      EE(I)=(B(1)+B(2)/X(I)+B(3)/(X(I)*X(I))-Y(I))**2
      CALL PLOTPT(X(I),EE(I),35)
  777 SUM =SUM+EE(I)
      WRITE (6,1002)SUM
      CALL OUTPLT
      DO 999 I=1,N
      C(I)=B(1)+B(2)/X(I)+B(3)/(X(I)*X(I))
      CALL PLOTPT (X(I),C(I),35)
  999 CONTINUE
      CALL OUTPLT
      XN =XNI
      WRITE (6,504)
      DO 10 I=1,NN
      XN =XN+DYN
      YY=B(1)+B(2)/XN+B(3)/(XN*XN)
   10 WRITE(6,505)XN,YY
      IF(II-IFF)506,507,507
  501 FORMAT (8I5)
  502 FORMAT (10I8)
  503 FORMAT(8E10.4)
  504 FORMAT(1H1,30X,*CHANNEL NUMBER                          COUNTS*,//)
  505 FORMAT(32X,E10.4,20X,E10.4//)
  508 FORMAT(10A8)
  602 FORMAT(1H1,*CASE STUDY * ,I4,*CURVE FITTING BY THE LEAST SQUARES
     1METHOD IN THE FORM OF ((A+B/E+C/(E.E)))*///)
 1001 FORMAT(1H1,5X,2HA=,F15.8,15X,2HB=,F15.8,15X,2HC=,F15.8///)
 1002 FORMAT(10X,*THE LEAST SUM OF SQUARES IS *,F15.8//)
  507 STOP
      END
```

REFERENCES

[1] W.A. Wenzel and W. Whaling, Phys. Rev., 87, 499 (1952).

[2] C. Foster, W.H. Kook, W.F. Van der Weg and R.E. Rovsendaal, Rad. Effects., 16, 139 (1972).

[3] J.F. Ziegler and W.K. Chu, IBM Thomas J. Watson Research Center, Yorktown Heights, N.Y. (to be published, March 1973).

[4] W.K. Chu and D. Powers, Phys. Rev., 187, No. 2, (1969).

[5] D.A. Thompson, Journal of Applied Phys., Vol. 42, No. 10, Sept. (1971).

[6] R. Fletcher and M.J.D. Powell, "A Rapidly Convergent Descent Method for Minimization", Computer J., Vol. 6, 163-168, June (1963).

[7] M.S. Livingston and J.P. Blewett, "Particle Accelerators", Chapter (13).

[8] J.F. Janni, "Calculations of the Energy Loss, Range, Path Length, Straggling, Multiple Scattering, and the Probability of Inelastic Nuclear Collisions for 0.1 to 1000 MeV Protons", Air Force Systems Command, Kirtland Air Force Base, New Mexico, Sept. (1966).

[9] M. Livingston and H.A. Bethe, "Nuclear Dynamics, Experimental", Rev. of Modern Physics, 9, 245, (1937).

[10] E. Fermi, "The Ionization Loss of Energy in Gases and Condensed Materials", The Physical Review, 57, 485, (1940).

[11] F. Bloch, "Bremsvermögen von atomen mit Mehreren Elektronen", Zeitschrift Für Physik, 81, 353, (133).

[12] W.K. Chu, et al., App. Phys. Letters, 22, 437, (1973).

[13] J.R.Popović and J.W. Bandler, "Internal Reports in Simulation, Optimization and Control: A General Program for Discrete Least pth Approximation", October (1973).

[14] S.K. Allison, "Passage of Heavy Particles Through Matter", Reviews of Modern Phys., Vol. 25, No. 4, Oct. (1953).

[15] W.C. Walske, Phys. Rev., 88, 1283 (1952).

[16] Nuclear Physics, Vol. A214, Editor L. Rosenfeld, North-Holand Amsterdam, (1973).

[17] Handbook of Chemistry and Physics, 52nd Edition, Editor Robert C. Weast, published by the Chemical Rubber Company, (1971-1972).

[18] A.H. Snell, "Nuclear Instruments and Their Uses", Vol. 1, Editor

[19] J.F. Ziegler, B.L. Crowder, Appl. Phys. Letters, 20, 178, (1972).

[20] Evans, "The Atomic Nucleus", Appendix B, p. 828, McGraw-Hill (1955).

[21] D.J. Rose and M. Clark, Plasmas and Controlled Fusion", M.I.T. Press.

[22] W. Whaling, Handbuch der Physik, Bd. XXXIV, p. 193.

[23] J.A. Lely, Ber. Dent. Keram. Ges., 32, 229 (1955).

[24] Proceedings of the Conference on SiC sponsored by the Electronics Research Directorate U.S. Air Force Cambridge Research Center, Pergamon Press (1960).

[25] R.D. Moorhead, Journal of Applied Physics, 36, 391, (1965).